Organic Photovoltaics using Novel Pentacene Derivatives

A dissertation presented

By

Anup Kumar Singh

to

The Department of Electrical and Computer Engineering

in partial fulfillment of the requirements
for the degree of

Doctor of Philosophy

in the field of

Electrical Engineering

Northeastern University
Boston, Massachusetts

December, 2013

Abstract

Organic photovoltaic (OPV) technology has attracted scientific and economic interest over the last decade due to the possibility of low-cost manufacturing and the rapid increase in OPV power conversion efficiency. The future potential of these devices and the increasing demand for green energy have motivated government and private organizations and researchers.

In OPV cells, excitons are generated in the organic semiconductor materials after absorption of photons. These excitons diffuse towards the electrode-semiconductor interface or donor-acceptor (p-type and n-type) interface, dissociate, and move by drift and diffusion processes toward the respective electrodes to generate electricity. The selection and processing of the organic materials are crucial to the performance of the cells.

Organic semiconductors suffer from low mobilities relative to most inorganic semiconductors. It is therefore critical to investigate what mobility is necessary for efficient operation or whether there is an optimal value for which cells can perform the best. We, in this thesis, use an existing model for a bilayer solar cell and modify the model to calculate a more accurate value of the electric field at the donor-acceptor interface. We use this new model to determine the optimum value of mobility for which the power conversion efficiency (PCE) is maximum. It is observed that PCE does not improve above the mobility (optimum) about 10^{-4} cm^2/V-s. Donor and acceptor thicknesses are also optimized using the simulation program to get the best efficiency. It was found that mobility increase has adverse impact on PCE for higher mobility cases ($\geq 10^{-4}$ cm^2/V-s). But for lower mobilities ($<10^{-5}$ cm^2/V-s), smaller increase (up to 100) in mobilities in fact enhances the PCE and the larger mobility ratio ($\geq 10^4$) causes a reduction in PCE when it is compared with the PCE in balanced mobility case. Exciton diffusion length in the donor can be increased at least up to 50nm where the simulation results showed a saturation effect on PCE.

The most studied OPV cell uses a donor-acceptor polymer blend of poly(3-hexylthiophene) (P3HT) and [6,6]-phenyl-C_{61}-butyric acid methyl ester (PCBM). These cells have a maximum efficiency of about 5%. It is imperative to look for alternative new organic materials that could provide superior performance in terms of efficiency or life-time or both.

One of the most promising organic semiconductors is pentacene which acts mainly as a donor molecule. We explore the efficacy of various new, very stable, pentacene derivatives synthesized

by Prof. Glen Miller's group at University of New Hampshire, Durham. These pentacenes are water soluble pentacene (WSP); 5,6,7-trithiapentacene-13-one (TTPO), and Bis-C_{60} adduct of 6,13-(decylthio)pentacene ($BC_{60}DTP$). We in this thesis present the OPV cell designs, fabrication steps, electrical results and discuss them to correlate the experimental findings with simulation data.

The Miller group synthesized the very first water soluble pentacene, WSP. It has a great half life time (~96 hours) in solution form, and is therefore an excellent material for solution processing. At Northeastern, a fabrication method was developed to overcome the crystallization issue with WSP during spin coating, and smooth thin films were achieved. This is important in bilayer OPV fabrication. We fabricated a working photovoltaic cell using WSP and characterized it to find an open circuit voltage of 0.525V and an overall efficiency of 0.145%. We also fabricated a bilayer OPV cell using the stable and thermally robust TTPO pentacene which is easily evaporated in a Thermal Evaporator to make a solid thin film. The short circuit currents of these cells are observed to be increased when the device temperature is increased. Because of low mobility of TTPO ($\sim 10^{-9} cm^2/V/s$), the overall efficiency is found to be only $1.5\times10^{-3}\%$. The new pentacene $BC_{60}DTP$ is soluble in many organic solvents and it has large half life time (750min) in solution form, potentially making it a good choice for fabricating a bulk heterojunction solar cell with P3HT as the donor material. The P3HT/$BC_{60}DTP$ cell showed a power conversion efficiency of 0.116% and open circuit voltage of 0.4V.

Acknowledgements

My first debt of gratitude must go to my thesis advisor, Prof. Nicol McGruer. I appreciate all his contributions of perennial guidance, valuable times, ideas and funding to complete my Ph.D. study. He motivated me to be confident in taking up difficult challenges and I came up with success. Eventually, I realized we often set a boundary of our limitations which are smaller than our actual capabilities are. I sincerely thank him for many insightful discussions of semiconductors, photovoltaic theories and microfabrication which helped me a lot during my PhD pursuit.

Special thanks to my committee thesis readers, Prof. Glen Miller and Prof. Matteo Rinaldi for their valuable suggestions during my thesis and proposal defense. My sincere thanks go to Prof. Glen Miller for providing me with various newly synthesized organic semiconducting materials to carry on my photovoltaic research. We had several useful meetings and insightful discussions with Prof. Glen and his research group members Chandrani, John, Jeremy and Yushu.

I am grateful to Prof. Ahmed Busnaina, the director of the Center for High-rate Nanomanufacturing (CHN), funded me through CHN as a Research Assistant. While working at the cleanroom microfabrication facility of the Kostas Nanoscale Research Center, the lab manager Scott McNamara has helped me with training on various equipment and my experiments; and he deserves my sincere thanks.

I sincerely thank Dr. Siva Subramanian from whom I learnt many things in device physics and microfabrication. He had been a great colleague, mentor and supportive. My friends and colleagues in the lab, Erfan, Huiyan, Saba, Suchit, Mithun, Peter, Malima, Hunchul with whom I had technical as well informal discussions were sources of laughter, joy and support.

I would be thankless if I don’t mention the indirect contribution of my villagers in India who have huge expectations from me since my childhood. This encouraged me to work hard and meet their expectations.

The love and support given by my parents, my brother and sisters, and my wife was incessant and truly inspiring, for which my mere expression of gratitude does not suffice. Our newly born angel Arohi filled the fuel of joy and energy in me towards the end of my PhD pursuit. Thank you.

Anup Kumar Singh
Northeastern University
December, 2013

I dedicate this thesis to
my parents, my brother and sisters,
my wife, and our little angel.

Table of Contents

Table of Figures:

1. Motivation and Outline

1.1 The Background

1.1.1 Limited Fossil Fuels and Environmental Impact

At present time we are heavily dependent on fossil fuels such as coal, oil, natural gas and wood for our daily need of energy requirements. In 2011, fossil fuels contributed approximately 82% of world's primary energy use (Source: Energy Information Agency). These sources of energy have a limited supply including Uranium and are non-renewable.

Based on the world's population growth trend, a total population of nine billion in the next 50 years and 10 billion by year 2100 has been projected. The world's energy demand will increase at least proportionately. A continuing rise in oil prices is expected due to increasing demand. According to the US department of energy, fossil fuels will be mostly consumed within 100-120 years. A few other estimates say it will be depleted even before the end of this century. In any case, these estimated times are not too far ahead before we may face a great crisis of energy supply. Therefore, we need to look for long lasting or renewable sources of energy.

Humans are adding more than 30 billion metric tons (30×10^{12}Kg) of CO_2 to the atmosphere each year, mainly by burning fossil fuel. Uncontrolled deforestation makes this situation worse due to the inability of plants to handle the rapid influx of CO_2, resulting global warming. The global mean surface temperature has already increased by 0.3-0.6°C since the late 19th century and the global sea level has increased by 10-25cm [1]. With the present CO_2 emission scenario a temperature increase of 0.6-7°C by 2010 is extrapolated. Certainly this will have a devastating effect on human life in coming decades.

In such conditions, development of alternative sources of green energy such as hydro-power, wind power, tidal power and solar power become inevitable.

1.1.2 Renewable Sources of Energy

We have abundant free energy sources like wind, tidal waves, sunlight, water reservoir potential etc. One of our targets in harvesting energy from these sources should be less harmful to humans and the environment. Secondly, the life-time energy output value should be considerably more than its input costs in installation, fabrication, labor, research and development, maintenance etc. In other words, the higher the energy payback values the better.

1.1.2.1 Wind Power

Wind energy has been used for generations and is in abundant supply. This energy is converted into other useful form of energy, e.g. wind turbines for generating electricity, windmills for mechanical power to machines, windpumps for pumping water, sails to propel ships etc. Sailboats and sailing ships have been widely used for thousands of years. The first practical windmill was used somewhere between 7th and 9th century in Iran [2]. In recent technology, wind energy is mostly used to drive turbines to generate electricity which is either stored using batteries or directly fed to the power grid. Growing demand for wind power generation in the market is due to its clean, abundant supply and one of the cheapest renewable energy in terms of energy payback value. US Department of Energy has estimated that wind power could contribute up to 20% of the nation's total electricity supply by 2030. Total wind energy production today is, however, less than 4% of worldwide electricity usage but the annual growth in recent years is more than 25%, according to World Wind Energy Association WWEA 2011 report [3]. American Wind Energy Association 2011 report says that wind energy cost has gone down to 5-6 cents/kWh which is 2 cents cheaper than coal-based electricity generation.

1.1.2.2 Hydro Power

Hydro power also has been used from ancient times for driving watermills, textile mills etc. The power is derived from the kinetic energy of the water current or falling water from a dam or reservoir. The concept is similar to wind power generation but since water is much denser than air, it can generate considerable power with even a slow water stream flow. Electric generators introduced in the early 20th century could be coupled with hydro turbines to generate electricity. Since then there has been a tremendous rise in hydroelectric power plant set up all over the world.

It is the most widely used form of renewable energy, meeting 16% of worldwide energy need in 2010[4].

The cost of hydroelectricity for plants larger than 10MW is around 3 to 5 US cents/kWh making it the cheapest renewable energy and comparable to energy produced from fossil fuels [4]. It is also considered to have the least environmental impact in terms of pollution and disposal of the waste products.

Tidal waves and currents are also used to generate electricity by using potential energy of the water head created by low and high ocean tides. The kinetic energy of the tidal streams is also used to drive the water turbines. Tidal power is also a form of hydro power and is renewable energy source. These are highly predictable compared to wind energy and sunlight.

1.1.2.3 Solar Energy

Our planet receives ~1.2×10^{17} watts power from the sun whereas the current worldwide electric energy consumption is ~10,000 times smaller, i.e. ~1.3×10^{13} watts [5]. Meaning, the earth receives more energy in an hour than the worldwide energy need for the whole year. Solar cells or photovoltaic cells directly convert solar energy in the form of energetic photons into electricity. Photovoltaic industries are still struggling with the fact that the energy payback value for solar energy system is much higher compared to that of fossil fuels. We need to focus more on research and development for increasing photovoltaic efficiency and life-time and for decreasing production costs by exploring alternative cheaper semiconducting active materials etc.

1.1.3 Photovoltaic Technology and Development

Global interest in photovoltaic (PV) technology has increased sharply over the last decade due to speculation on the possibility of a future energy crisis, pollution, developments in fabrication technology etc. Spectacular gains in both the PV market and in research activity are seen. A solar cell or photovoltaic cell directly converts the sunlight into electricity. The first solar cell was constructed by Charles Fritts in 1880s where he used Selenium semiconductor and a thin layer of gold. The semiconductor served as photon absorber and the electron-hole pair is separated by the electric field in the Au-Se Schottky junction. The first silicon solar cell where electron-hole pairs were separated at the p-n junction was developed by Russel Ohl in 1941. The cell was remarkably improved by Gerald Pearson, Calvin Fuller and Daryl Chapin in 1954 at Bell Laboratory and was capable of 6% conversion efficiency from direct sunlight [6].

Between 1970 and 1983 photovoltaic installations grew rapidly, but falling oil prices in the early 1980s thwarted the growth in PV research from 1984 to 1996. Since 1997, PV development has accelerated due to supply issues with oil and natural gas, global warming concerns, and the improving economic position of PV relative to other energy technologies [7]. Photovoltaic production growth has averaged 40% per year since 2000. According to the European Photovoltaic Industry Association the world's total installed capacity reached 40 GW in 2010 from 23 GW in 2009.

Currently, most of the solar cells are made of silicon where costs are high, many alternative types of solar cells are fabricated and new cheaper materials have been investigated to replace silicon. The use of amorphous silicon is one of its solutions as it is less expensive and higher light absorbing capability compared to monocrystalline or polycrystalline silicon. Recently, organic solar cells (OSCs) having much cheaper photo active layer organic semiconductors have drawn attentions of PV research groups worldwide due to its easy and inexpensive fabrication cost.

Various types of solar cell's power conversion efficiency from 1976 through 2012 have been reported by National Renewable Energy Laboratory (NREL) in Figure 1.

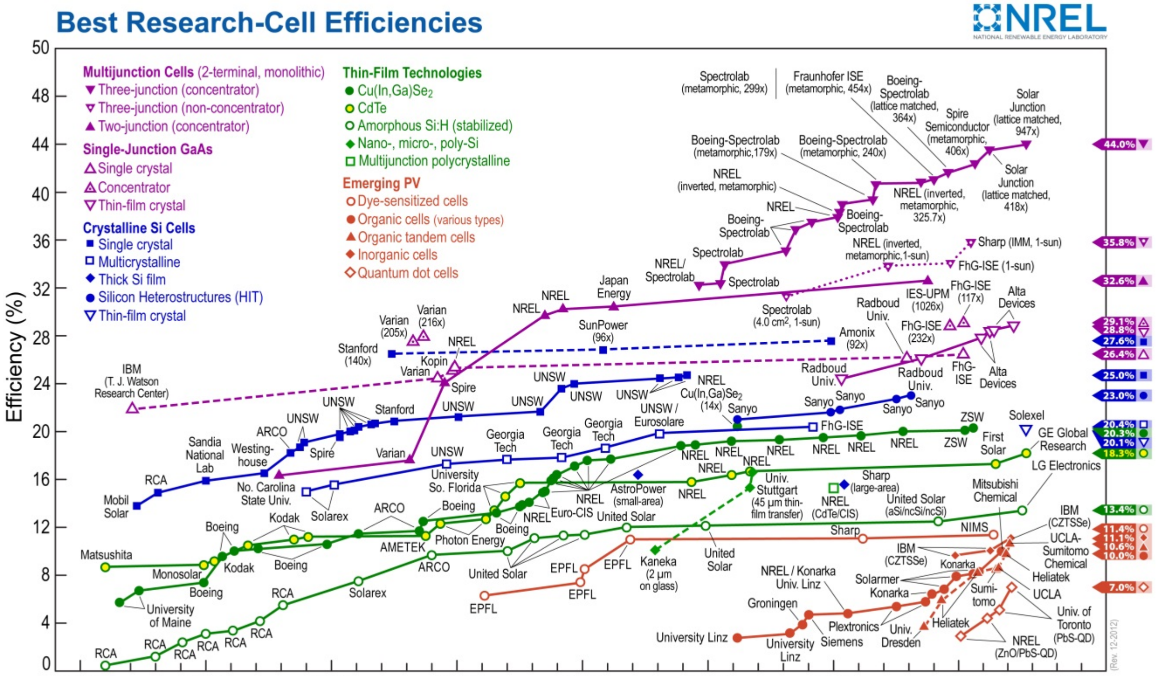

Figure 1: Power Conversion Efficiency for various photovoltaic technologies up to year 2012 (Source: NREL)

1.1.4 Photovoltaic Manufacturing: Present and Future

In the USA, average cost of grid-supplied electricity in 2009 was 9.5¢/kWh and will continue to rise due to increase in demand. Three different rates in cost increment are shown in Figure 2 [8]. Photovoltaic production has grown at a rate of greater than 40%/year over the past decade. However, the current price of electricity produced by PV is 2 to 3 times the cost of grid-supplied electricity but it continues to decrease and projected to converge, called grid parity, sometime in this decade (before 2020) [8], shown in Figure 2.

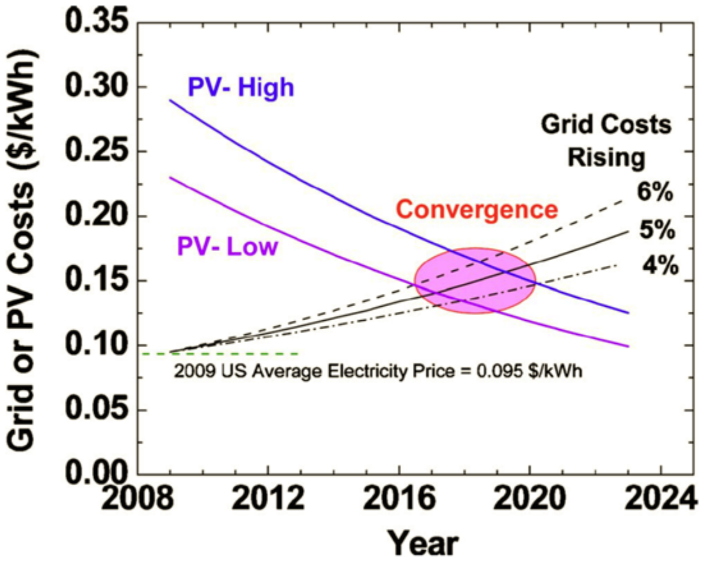

Figure 2: Projected convergence of the cost of electricity produced by PV and the grid prices [8]

1.1.5 Solar Cell Types

Various types of solar cells based on types of materials used are classified briefly in this section. Inorganic bulk semiconductors such as mono- and polycrystalline silicon, amorphous silicon and thin films of semiconductors such as cadmium telluride (CdTe), Copper indium gallium selenide (CIGS) are used as photovoltaic material. Another category of materials include organic dyes and organic polymers make solar cells of thin film type. The third category uses nanocrystals and used as quantum dots.

1.1.5.1 Solar Cells of Crystalline Silicon

Photovoltaic cells made of silicon are the p-n junction type where electron-hole pairs generated after absorbing photons are driven in opposite directions by the barrier potential generating a current in the closed circuit. Solar cell modules manufactured today mostly use monocrystalline (c-Si) and polycrystalline silicon (poly-Si) which shared 87% of the PV market in 2011 [9]. Both are discussed below.

- **Monocrystalline Silicon (c-Si):**

Monocrystalline silicon is produced by the Czochralski (CZ) method where a single crystal silicon seed is dipped into a high purity melt of polycrystalline and pulled slowly to form an ingot of single crystal silicon. Single crystal silicon has high lattice uniformity throughout the material resulting in higher mobility of charge carriers. Although, they show a higher power conversion efficiency (up to 25% [10]) compared to poly-Si PV modules, c-Si manufacturing costs are higher. Due to higher thickness requirements and a significant amount of c-Si loss during wafer process, cost of the PV modules becomes even more.

- **Polycrystalline Silicon (poly-Si):**

Polycrystalline silicon has many crystalline grains connected in different orientations. Polycrystalline silicon is made by cooling large molten blocks of silicon. Poly-Si is stronger and can be cut to one-third the thickness of c-Si material making it cost effective. The ribbon growth method directly grows thin sheets of poly-Si that does not require sawing, reducing the cost of the PV module. Irregular grain boundaries in poly-Si hinder the charge mobility causing a decrease in power conversion efficiency. However, its longevity comparable to monocrystalline cousin, lower manufacturing cost and decent conversion efficiency up to 20% [10], such cells are the most popular choice in residential installations

1.1.5.2 Thin Film Solar Cells

- **Amorphous Silicon (a-Si):**

Amorphous silicon is the most developed of the thin film technologies and its basic electronic structure is p-i-n type. It has a higher bandgap (1.4 - 1.7 eV) and stronger absorption in the visible light due to high absorptivity, even a micron thick amorphous silicon is able to absorb most of the usable sunlight, hence reduces the material cost. Amorphous silicon can be deposited on low cost substrates such as glass and transparent plastic, and it requires low temperature (≈ 75℃) processes, reducing the production cost drastically. However, disordered a-Si based solar cells suffer from a poor conversion efficiency of about 10% and from significant degradation within few months of sunlight exposure. Amorphous silicon solar cells are about 3% of the world PV market [9].

- **Gallium Arsenide (GaAs)**

It's a compound semiconductor made of gallium (Ga) and arsenide (As) and has a crystal structure same as that of silicon. Due to a high photon absorption coefficient, GaAs requires only a few microns of material to absorb the same amount of light as a 200-300 micron thick crystalline silicon cell. It has high power conversion efficiency too, about 25-30%. A triple junction GaAs cell held the high efficiency record on 15 Oct 2012 [11].

- **Cadmium Telluride (CdTe)**

It is polycrystalline direct bandgap material made of cadmium (Cd) and Tellurium (Te), which has a band gap of 1.5 eV, a perfect matching material for absorbing sunlight coming to the Earth in terms of optimal conversion to electricity. Since it is difficult to produce thin film of n-type CdTe, a heterojunction of p-CdTe and wide band gap n-type semiconductors are commonly used. The most common heterojunction partner for p-CdTe is wide band gap (2.4eV) n-type CdS thin film. High absorptivity of CdTe film enables sunlight to be fully absorbed by nearly 2μm thick material [8], which reduces the material cost. In addition, relatively easy and cheap fabrication processes such as high-rate evaporation, spray or screen printing are added advantages. An efficiency of more than 17% has been achieved so far [10]. The power conversion efficiency of CdTe based solar modules has disadvantages of its instability and extreme toxicity of cadmium metal during recycling. It represented 6% of the 2011 world market [9].

1.1.5.3 Dye Sensitized Solar Cell (DSSC)

The dye sensitized solar cell also known as a Gratzel cell is an electrochemical device. The Gratzel cell was invented by Gratzel at EPFL, Switzerland [12, 13]. A porous bed of titanium dioxide (TiO_2) nanoparticles soaked in a dye solution acts as photoactive layer. Ruthenium-polypyridine is generally used for dye molecules, also called sensitizers. Sensitizers are in contact with a thin layer of iodide electrolyte coated on cathode. When excited by a light photon, the dye molecule injects an electron into the TiO_2 and diffuses towards the external circuit. This loss of the electron is compensated by the iodide electrolyte which regains an electron from the cathode to complete the circuit. DSSC has a very high response in visible light spectrum, so can efficiently work even in diffused light, indoor light or cloudy weather. The liquid electrolyte could be leaky and freeze at low temperatures. A record high efficiency of 12.3% has been achieved [14].

1.1.5.4 Quantum Dot Solar Cell (QDSC)

The electron energies in quantum dots (QDs), which are nanometer sized semiconductor particles, are limited as per quantum mechanics considerations. These energy levels are the bandgaps which can be tuned by changing the size of the QDs without changing the material. The tuning requires simple processes such as varying growth time or temperature. This facilitates QDs to use in multi-junction solar cells to absorb a wider spectrum of photons. Colloidal quantum dots can be synthesized using inexpensive wet chemistry processes. The QD solar cell has a record efficiency of 7% [15].

1.1.5.5 Organic Solar Cell (OSC)

In organic photovoltaic cell (OSCs) [16-23], the active materials are donor (p-type semiconductor) and acceptor (n-type semiconductor) layers. Excitons (excited electron-hole bound pairs) are generated upon absorption of photons and are dissociated at the donor-acceptor (D-A) interface. These separated charge carrier's transport towards the respective electrodes is governed by diffusion and the internal electric field. In a single layer OPV device, excitons are dissociated at the metal-semiconductor Schottky barrier whereas in bilayer devices they are dissociated at the donor-acceptor planar junction. A method of improving dissociation of excitons was later developed by making the active layer of intimately mixed active D-A materials together that forms a much larger interface area. Phase segregation is also important for bi-continuous path for charge carriers to reach to electrodes. Organic semiconductors or polymers are inexpensive as they can easily be synthesized in any chemical laboratory. These materials have very high absorption coefficients. Only a few hundred nanometers of material is required to absorb the sunlight efficiently and therefore less material is needed which lowers the fabrication cost further and also enables fabrication of flexible devices. Low efficiency is the one of the major drawback of such cells, yet inexpensive fabrication makes OPV research attractive. A recent rapid growth in overall efficiency has been observed. Heliatek has recently achieved the highest efficiency of 12% by improving its previous record of 10.7% efficiency [24].

1.2 Motivation of This Thesis

In previous Section, we have seen that photovoltaic technology is one of the most promising technologies among renewable energy resources. Photovoltaic technology apart from being abundant in nature, much cleaner compared to conventional fuel resources such as coal and natural gas, its portable use facilitates a quick installation of solar cells at any small and remote place are the.

Silicon is a prime candidate for photovoltaic cells as it quite abundant in the nature and has broad absorption spectrum of the sunlight reaching to the Earth. In photovoltaic industries, the production of the silicon based photocells is well established. The underlying problem with this is the cost of production due to high purity and high temperature process. A widespread industrial production is impeded due to the marginal energy payback value of this technology. A large number of hazardous chemicals and water are needed to make monocrystalline silicon solar cells. The energy production from the photovoltaic cells, however, is clean but the production of the cell itself is not. Harmful gases such as sulphur dioxide and carbon dioxide are released during the production of electronic grade silicon. In terms of the environmental impact, the quantitative values of Composite Environmental Impact Index (CEII) of energy resources presented in the Table below indicates the silicon based solar cells are better than energy produced by coal and natural gas but not better than wind and hydroelectric power [25].

Total Environmental Impact of 1 kWh of Electricity Production From -				
Coal	Natural gas	Solar panel	Wind	Hydro
885.5	133	52.4	8.5	0.5

Therefore, we need to develop a technology which can reduce this environmental cost if we want a mass production of photovoltaic cells. Organic photovoltaic technology using organic semiconductors as active layers can be among promising technologies which can cause less environmental pollution and comparatively less expensive disposal of the waste.

Unlike silicon, organic semiconductors have a very high light absorption coefficient and hence a very thin layer of the material coating less than couple of hundred nanometers can absorb the necessary amount of light to produce the electricity. This is another reason the material cost in organic solar cell is much less compared to silicon photocells. Organic semiconductors offer a less sophisticated low temperature synthesis than silicon production resulting lowering the cost.

Flexible cells are possible to fabricate due to very thin layer of the materials used in it. In this case, of course, brittle ITO has to be replaced by a flexible, conductive and transparent substrate such as polyethylene terephthalate (PET) coated with a conductive thin polymer.

Polymers can be coated using low cost techniques such as ink-jet printing, screen printing, doctor blading etc. [26]. Roll-to-roll deposition of the active layers on flexible substrates would be very cost effective technological effort to establish organic photovoltaic technology in the market.

P3HT and PCBM are the most common active materials used as donor and acceptor, respectively and OPV cells made out of these materials show efficiencies of 3-6% [27-30]. Other common donor materials are pentacene derivatives that coupled with C_{60} as acceptor show efficiency range of 1% - 2.8% [31-34]. Organic materials also suffer from low lifetime or stability. For commercial production of organic photovoltaic cells the laboratory efficiency needs to be improved to at least 15%. Material stability is also important aspect to address. Therefore, we need to explore new organic donor and acceptor materials that can provide better efficiency and stability. We, in this thesis, are discussing the design, fabrication and investigating the performance of OPV cells using novel pentacene molecules synthesized by Prof. Glen Miller's group at University of New Hampshire, Durham.

One of the key factors of poor OPV cell efficiency is the very low mobility of carriers in the active materials. It becomes inevitable to investigate whether the improvement in the mobility is always essential or there is an optimal value for which cells can perform the best. Other parameters such as donor and acceptor thicknesses affect the cell efficiency drastically and optimal thicknesses need to be chosen. This thesis addresses the task of device modeling, simulation and analysis which is a perfect choice for giving a better insight to the cell parameters variation versus the performance.

1.3 Outline

Chapter 2 will begin with details about the physical theory involved in organic photovoltaic device operation. This will include light absorption, exciton generation, charge separation and collection at electrodes. This will also describe the device parameters which are extracted after the device electrical characterization. Different types of organic photovoltaic structures are also described which are used in our various cell designs.

In **Chapter 3**, we present a simple existing device model for the bilayer organic solar cell with a modification in the model to calculate electric field at the interface more accurately. With simulation, the model explores the effect of critical parameters such as charge carrier mobilities, photoactive layer thicknesses, absorptivity, metal work functions, and LUMO and HOMO values of donor and acceptors etc. We calculate to find a feasible solution by optimizing mobilities and thickness to achieve maximum power conversion efficiency quantitatively.

In C**hapter 4**, we discuss about design, fabrication and testing of the organic solar cell using a newly synthesized pentacene derivative which is soluble in water (water soluble pentacene or WSP), ethanol, methanol etc. The coatings of this solution processable pentacene in various solvents are studied and a method is developed for coating a film of WSP.

Chapter 5 describes about an OPV cell using another new pentacene 5,6,7-trithiapentacene-13-one (TTPO) which is thermally stable up to 400℃. A bilayer cell is fabricated; and characterized at two different raised temperatures as its mobility increases with increase in temperature.

In **Chapter 6**, $BC_{60}DTP$ based bulk heterojunction solar cell design, fabrication and characterization are discussed.

Chapter 7 will conclude this whole thesis briefly and will present with possible extensions of my current research work.

Chapter 8 is **Appendix** which includes the measurement set up and an alternative to expensive solar simulators. It also includes a run sheet of the OPV device fabrication steps and MATLAB device simulation code.

2. Organic Solar Cell – General

2.1 Introduction

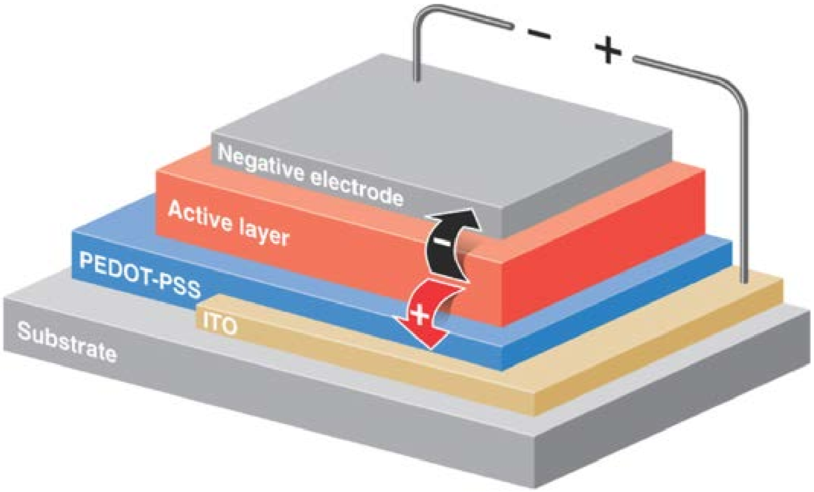

Figure 3: Schematic of an organic photovoltaic cell (source: http://spie.org/x14269.xml)

Figure 3 is a schematic of a typical organic solar cell consisting of a transparent and conductive electrode (usually an ITO anode) with a transparent substrate, an electron blocking layer (such as PEDOT: PSS), an active organic polymer layer (monolayer, bilayer or bulk heterojunction) and a cathode (typically Al or Ca/Al). Light enters through the transparent substrate and charge carriers are generated in the active layer after light absorption and flow towards the respective electrodes. Details of operation are presented in the following sections.

This chapter will describe device operation from light absorption to transport of charge carriers. Various photovoltaic structural designs such as monolayer (or homojunction), bilayer (or planar heterojunction) and bulk heterojuntion will be described. A band energy model under forward and reverse bias, open-circuit and short-circuit conditions will also be explained. The origin of conjugation and semiconductivity in organic materials will be discussed. Atomic and molecular phenomenon such as excitons and polarons within organic materials will be described. A circuit model with the necessary electrical parameters representing the cell will also be presented.

2.2 Principle of Operation

Schematically, Figure 4 indicates loss mechanisms and device operational mechanisms of organic solar cells at various stages from light absorption to charge collection. In the following, we will discuss the five operational steps of organic photovoltaic device, shown in Figure 5.

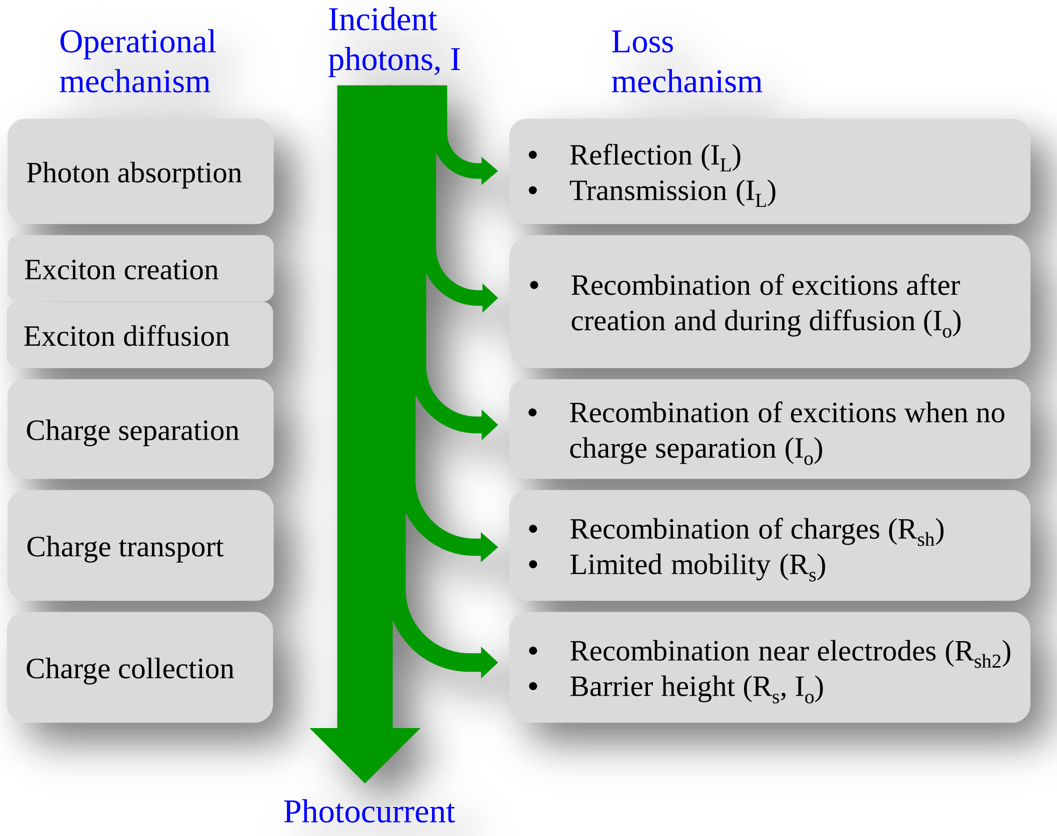

Figure 4: Operational steps and loss mechanism in organic solar cell

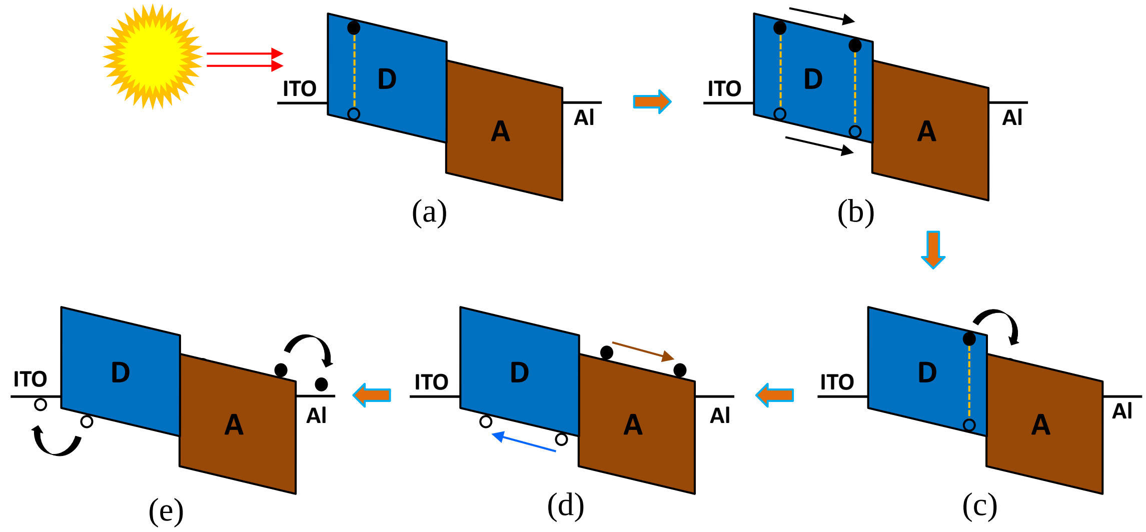

Figure 5: Operational steps of bilayer and bulk-heterojunction OPV cell: (a) Photon absorption and exciton generation (b) Exciton diffusion (c) Exciton dissociation, polaron formation & dissociation (d) Charge transfer (e) Charge collection. Blocking layers are not shown for simplicity.

(a) Photon absorption

The first step for power conversion from the light is absorption of photons in active layer of the organic solar cell. Incoming photons undergo reflection, absorption and transmission.

(b) Exciton generation and diffusion

Photon having energy more than or equal to optical band gap of the organic polymer when absorbed, an electron is excited leaving a hole behind but are still attracted strongly by a Coulombic force. This quasineutral particle in a bound state is called an exciton.

The properties of excitons are discussed in Section 2.5. Excitons start diffusing towards a systematically designed interface with another organic polymer or electrode. The excitons diffuse to the donor-accept interface in case of a bulk heterojunction or bilayer device or a Schottky barrier in the case of a single active layer. The diffusion length must be at least equal to the polymer thickness for excitons to be efficiently dissociated before they are quenched.

(c) Exciton dissociation:

Once excitons reach the interface, they get dissociated due to the local electric field created by difference of electron affinities (EAs) and ionization potentials (IPs) between donor and acceptor material. At the interface, the polymer semiconductor material with higher electron affinity (lower ionization potential) can take electron (hole) from the material having lower EA (higher IP). In other words, after dissociation of an exciton at D/A interface, the electron (hole) from the LUMO (HOMO) of donor (acceptor) transfers to the LUMO (HOMO) of acceptor (donor). Excitons do not contribute to photocurrent if the difference in ionization energies or electron affinities is not sufficient to dissociate them.

(d) Charge transport:

The dissociated charge carriers start moving towards the respective electrodes by diffusion and drift processes. The mobility plays an important role, and is discussed later in this Chapter. At the interface of the organic semiconductor and metal electrodes, the separated charge carriers are collected resulting in a photocurrent.

(e) Charge collection:

The efficiency of charge collection is mostly dependent on the energy band alignment of the donor-HOMO with the anode and the acceptor-LUMO with the cathode. The nature of the semiconductor/electrode interface is complex as interfacial charge density due to dipole formation or chemical reaction at the interface, widely affect the alignment which may or may not favor the charge collection. Efficient charge collection is achieved by using intermediate layers such as electron and/or hole transport layers that favor unidirectional flow of carriers; and passivation layers to inhibit chemical reaction.

2.3 Device Physics

Below are the diagrams, Figure 6(a) and Figure 6(b) for a general schematic of bilayer and bulk heterojunction OPV devices showing electrodes and various layers used. In bilayer structure, it is always guaranteed that donor and acceptor phase are in contacts with hole and electron transport layer, respectively whereas in bulk heterojunction case, it happens only if bi-continuous or percolated paths exist which is necessary for the cell to work. The bilayer and bulk heterojunction both can be represented by a single energy band diagram, Figure 6(c) as they both differ only in spatial orientation of layers and not energetically. The step by step process of operation is shown via energy band diagram (Figure 6(c)). This section mainly explains about functions of various layers used in the cell. The basic comparison of three different types of OPV structures are explained in next section.

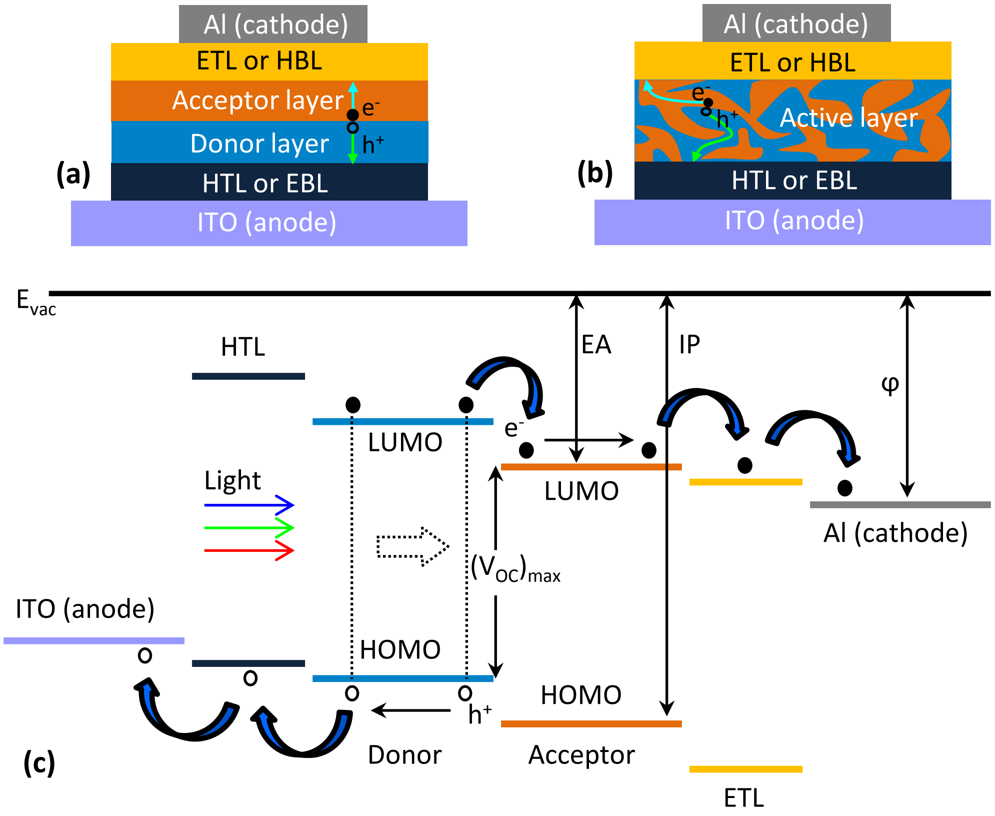

Figure 6: A general schematic of (a) a bilayer OPV cell (b) a bulk heterojunction OPV cell and (c) Energy band diagram of the device

2.3.1 Active Layers for Light Absorption

Active layers are the main constituents of OPV cell which are small molecules or polymer semiconductors. These are also called photo-active layers (or donors and acceptors, explained next) as they can absorb photons with energy greater or equal to optical band gap of the material and generate excitons that are eventually converted to charge carriers. The light absorption can be explained by Beer-Lambert's law which relates the absorption of light through a material having absorption coefficient $\alpha\ (\lambda)$. If the material is a solid thin film of thickness (d), then $\alpha(\lambda)d > 1$, transmitted light intensity $I(d)$ can be represented by

$$\boldsymbol{I(d) = I_o e^{-\alpha(\lambda)d}}$$

Where, I_o is incoming light intensity, $\alpha(\lambda)$ is the wavelength dependent light absorption coefficient and d is the film thickness.

For most efficient absorption of sunlight at earth, the ideal band gap is around 1.4 eV. Most organic semiconducting polymers have band gaps higher than 2 eV (600 nm) which limits the possible absorption to about 30% of the solar spectrum. Organic polymers display orders of magnitude lower mobility compared to inorganic semiconductor crystals and therefore the material has to be very thin in order for excitons to reach the interface without being quenched. Fortunately, a high absorption coefficient (usually > 10^5 cm^{-1}) of the material partially balances the negative impact of lower mobility in photovoltaic device. Some light trapping methods are also employed to enhance the light absorption [35].

2.3.2 Donor/Acceptor Interface:

At heterojunction, the material with higher electron affinity can take electrons to its LUMO is called acceptor (A). Similarly, the material with lower ionization potential can easily donate an electron from its HOMO, or in other words can take a hole is called donor (D). Meaning, the material with lower (higher) LUMO and HOMO values is donor (acceptor). An electron in donor is excited to LUMO leaving a hole in its HOMO or a hole in acceptor is excited to HOMO leaving an electron in LUMO thus forming an exciton after absorbing a photon. Unlike conventional solar cells, absorption of photons is not enough to generate free charge carriers and an interface of donor/acceptor (D/A) material with proper energy level matching is required for exciton to dissociate into free charge carriers. The differences in energy levels LUMOs and HOMOs should be larger than exciton binding energy (~ 0.4 eV) for dissociation to occur. Exciton generated in donor (acceptor) material is dissociated at the interface of the organic semiconductors heterojunction by donating an electron (hole) from its LUMO (HOMO) to the LUMO (HOMO) of the acceptor (donor) material and retaining the hole (electron). Exciton dissociation has been described as two-step process: (a) charge transfer to form polaron, i.e. exciton separated into hole and electron in D and A, respectively, but still bound together; (b) polaron dissociation into separated charge carriers (however, polarons may recombine also). The separated charge carriers are then transported to respective electrodes. Therefore, the donors are hole transporting materials or p-type and the acceptors are electron transporting materials or n-type.

If both LUMO and HOMO level of one of the heterojunction organic semiconductor materials is bigger than the other, exciton split is not possible but rather energy transfer will occur in the form of radiation. This situation is desired for designing light emitting diodes (LEDs).

Poly(3-hexylthiophene-2,5-diyl) or P3HT, poly[2-methoxy-5-(2-ethylhexyloxy)-1,4-phenylenevinylene] or MEH-PPV, copper phthalocyanine (CuPc) are commonly used donors or p-type material in organic electronics. Fullerene (C60), [6,6]-phenyl C_{61} butyric acid methyl ester (PCBM) are common n-type organic semiconductors or acceptors.

2.3.3 Semiconductor/Electrode Interface:

A seminal work of Mott and Schottky has established the theory of metal-semiconductor contact for charge injection from the doped semiconductor to the metal [36, 37]. However, it is not well known to what extent it applies in organic semiconductors, but it is often used to predict the behavior of such contacts for carrier collection or injection. The barrier can be formed at the interface of ITO (anode) and the donor material or Al (cathode) and the acceptor material. A Schottky barrier is formed when metal work function is smaller (larger) than the work function which is the difference between vacuum level to Fermi level of p-type (n-type) semiconductor, i.e. $\phi_M < \phi_S$ ($\phi_M > \phi_S$), otherwise the contact is ohmic. Such barriers act as an obstruction to charge carriers which should kept minimum for better charge collection. Charge carriers can overcome the barrier ϕ_B by thermionic emission and/or field emission (quantum mechanical tunneling). The current through the barrier is often described by

$$\boldsymbol{J = J_0 e^{(qV-\phi_B)/nkT}}$$

where, J_o is a constant for low doping and $n \approx 1$ at high temperatures [38], V is the applied voltage and T is the temperature. When the thermal energy $k_B T$ is sufficient to produce charge carriers with potential greater than the barrier height ϕ_B ($=|\phi_M - \phi_S|$), thermionic emission occurs.

The Schottky barrier is ohmic also when the barrier ϕ_B is very thin or very low. Ohmic contacts are preferred for efficient charge collection for which electrode work functions should be properly matched at donor-HOMO and acceptor-LUMO levels. A large difference between the anode work function and the D-HOMO or the cathode work function and the A-LUMO will cause the loss of open circuit voltage and working potential.

2.3.4 Interfacial Layers:

By inserting a very thin interfacial layer between the electrode and active layer the overall device performance can be significantly improved, Figure 6. Several interfacial buffer layers have been reviewed by Chen et al. [39]. The main functions are described below:

2.3.4.1 Functions of interfacial materials

(a) Injection barrier reduction by interfacial dipole: The injection barrier ϕ_h (ϕ_e) is the difference between the metal work function and HOMO (LUMO) of the semiconductor material. Upon introduction of an interface dipole with the positive (negative) pole towards metal the hole (electron) injection barrier can be reduced, shown in Figure 7. Barrier height reduction increases the injection efficiency of carriers in case of OLEDs and can enhance the open circuit voltage in OPVs. Similarly, the reverse dipole can increase the injection barrier causing an open circuit voltage loss [40, 41].

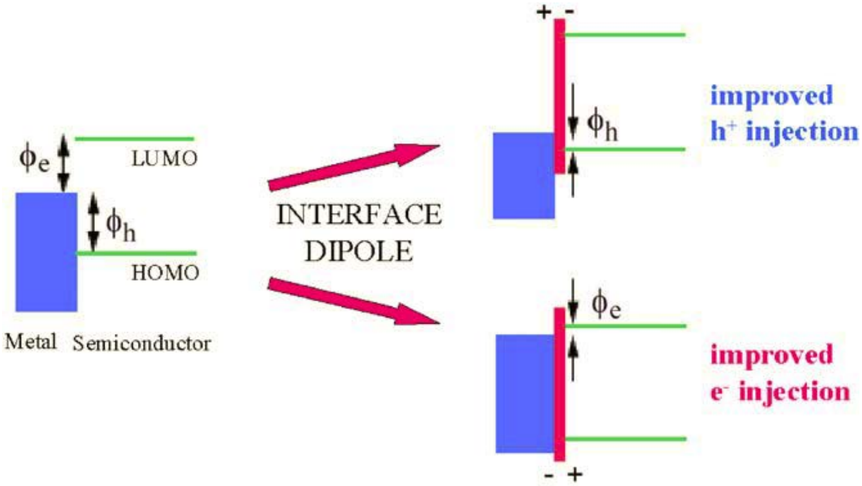

Figure 7: Modification of the hole (electron) injection barrier ϕ_h (ϕ_e) upon introducing interface dipole (source: [42]).

(b) Blocking layers: Blocking layers are introduced between the electrode and the active layer of OPV cells to avoid recombination of charge carriers at semiconductor-electrode interface and allow passing certain type of charge carrier, either holes or electrons. An electron blocking layer (EBL), also called a hole transport layer (HTL) is when inserted between the anode and donor layer, only holes could be allowed to reach the anode from the active layer and hence impedes the recombination with electrons at the anode-donor interface. Similarly, insertion of hole blocking layer (HBL) or electron transport layer (ETL) between the active layer and the cathode (Al) can improve the device performance by allowing electron transport only and also hindering exciton quenching at cathode.

(c) Active layer passivation and suppression of diffusion:

Metal ion diffusion into the organic layer has a detrimental effect. The metal/organic interface undergoes chemical reactions that change the contact properties and forms interfacial dipole barriers which can cause kink (S-shape) effects in J-V curves [43]. Therefore a buffer or passivation interlayer is inserted to prevent diffusion and interface reaction.

(d) Modulation of optical field by an optical spacer:

The incident light forms a standing wave inside the active layer of the cell. The transparent optical spacer between polymer and electrode is introduced such that the optical field strength is maximum in active layer zone to enhance the photocurrent [44].

2.3.4.2 Anode interlayers

The most commonly used EBL at anode is poly(3,4-ethylenedioxythiophene): poly(styrenesulfonate) or PEDOT: PSS, a conjugated polymer that is doped by H^+ from PSS has work function of 4.75eV – 5.15eV depending on the doping concentration [45]. PEDOT is conductive (~1000S/cm) and not soluble in water, however, when doped with PSS, it becomes hydrophilic and soluble in water. PEDOT: PSS has a lower conductivity of conductivity ~ 1-10 S/cm. It absorbs little light in the visible region and is widely used as transparent and conductive polymer with ductility. PEDOT: PSS is widely used for coating ITO glasses to smooth their spikiness to avoid shorts in OSCs. The top layer of PEDOT: PSS is PSS^- rich phase which is a wide band gap polymer is responsible for blocking the electrons [46] and increased photovoltage

[47]. This layer also hinders exciton recombination at the anode resulting in improved photo carrier generation. PCE with optimized thickness of PEDOT: PSS can be 6 times more than the PCE without it [48]. However, its acidic nature etches the ITO and causes lifetime instability [49, 50]. Its conductivity can be significantly improved by a post-treatment (also called secondary doping) with various compounds, such as dimethyl sulfoxide (DMSO), ethylene glycol (EG), acids etc. [51, 52]. Molybdenum trioxide (MoO_3) is also used as an EBL due to its low LUMO value (LUMO – HOMO: 2.4eV – 5.3eV) and high transparency and improvement in device performance has been achieved [53-55]. V_2O_3 and MoO_3 as anodic interlayers is are reported as replacements for PEDOT: PSS [56].

2.3.4.3 Cathode interlayers

Aluminum is the most commonly used cathode electrode. Instability of Al was studied by Logdlund et al and Antoniadis et al who found that Al-C bond formation disrupts the π-conjugated system [57, 58]. Formation of a dipole at the interface of Al and PCBM in (P3HT: PCBM) device increases the extraction barrier and reduces the V_{OC} [40, 41]. A low work function metal, calcium (Ca), makes an ohmic contact when inserted between Al and the polymer, resulting in a higher fill factor [59]. Alkali metal compounds such as lithium fluoride (LiF) and cesium carbonate (Cs_2CO_3) provide low work function contacts [60-62]. A thin layer (~1nm) of LiF acts as dipole modifying the vacuum level to reduce the workfunction of Al which helps in better electron extraction [63] and also serves as a buffer layer to reduce the Al diffusion into the polymer. A more versatile electron injection layer Cs_2CO_3 which can be thermally evaporated or spin coated before cathode layer, be it Al or Ag, shows similar performance [60, 64, 65].

Other commonly used HBLs or ETLs between the polymer and the cathode are bathocuproine (BCP), titanium dioxide (TiO_2), zinc oxide (ZnO). Such materials are able to block holes due to the large HOMO values of BCP (LUMO-HOMO: 3.5 eV – 7 eV), TiO_2 (LUMO – HOMO: 4.4 eV – 8.1eV) or ZnO (LUMO – HOMO: 4.2 eV – 7.5 eV) and inhibit recombination of excitons at the cathode. BCP as an interfacial HBL is also known to be an excellent exciton blocking layer, and can more than double in the PCE [66, 67]. With titanium dioxide (TiO_2) the PCE is enhanced more than twice and also the stability is greatly improved [68, 69]. With ZnO as the HBL an improvement in device performance and stability is reported [53, 70, 71].

2.3.5 Electrode Materials:

The selection of electrode material is crucial and as discussed before, depending on the LUMO/HOMO levels of the Donor and Acceptor materials, the contact could be ohmic or blocking. The difference between anode and D-HOMO or cathode and A-LUMO should be minimized to lower the voltage loss of the cell. Elements in the periodic table with their workfunctions are given in Table 1 [72]. The common cathode electrodes used in organic solar cells are Al, Ca and Mg. Effects of few common cathodes on performance of BHJ solar cell were investigated in [73].

Transparent electrodes are generally hole-collecting anodes and have high work-functions. Indium tin oxide (ITO) is the most widely used transparent conducting anode, which is a degenerate semiconductor comprising a mixture of indium oxide (In_2O_3 – 90%) and tin dioxide (SnO_2 – 10%). It is formed by reactive sputtering of an In-Sn target in an oxygen atmosphere. ITO has a Fermi-level of 4.5 – 4.9 eV and a bandgap of 3.7eV. There is no absorption of light of wavelength longer than 350 nm due to its large bandgap and hence it is quite suitable as a conducting material that is transparent to much of the solar spectrum.

Table 1: Workfunction (eV) of elements in polycrystalline form.

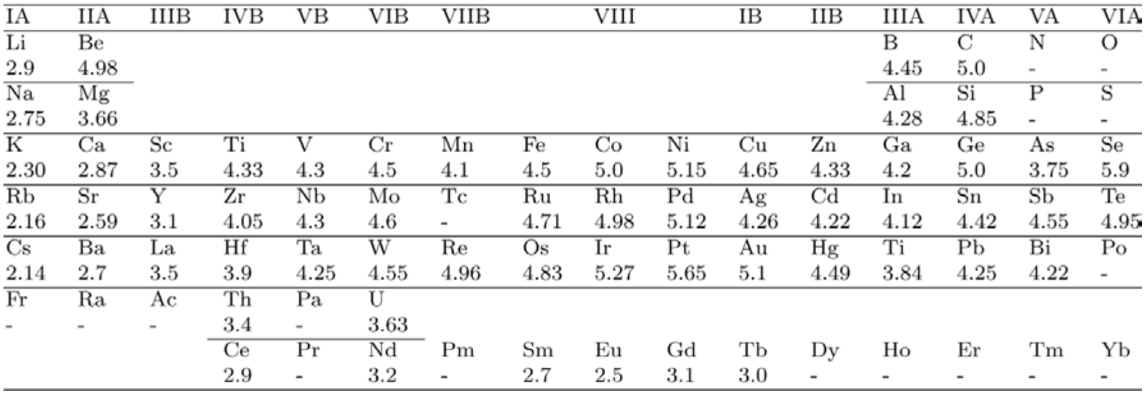

IA	IIA	IIIB	IVB	VB	VIB	VIIB		VIII		IB	IIB	IIIA	IVA	VA	VIA
Li	Be											B	C	N	O
2.9	4.98											4.45	5.0	-	-
Na	Mg											Al	Si	P	S
2.75	3.66											4.28	4.85	-	-
K	Ca	Sc	Ti	V	Cr	Mn	Fe	Co	Ni	Cu	Zn	Ga	Ge	As	Se
2.30	2.87	3.5	4.33	4.3	4.5	4.1	4.5	5.0	5.15	4.65	4.33	4.2	5.0	3.75	5.9
Rb	Sr	Y	Zr	Nb	Mo	Tc	Ru	Rh	Pd	Ag	Cd	In	Sn	Sb	Te
2.16	2.59	3.1	4.05	4.3	4.6	-	4.71	4.98	5.12	4.26	4.22	4.12	4.42	4.55	4.95
Cs	Ba	La	Hf	Ta	W	Re	Os	Ir	Pt	Au	Hg	Ti	Pb	Bi	Po
2.14	2.7	3.5	3.9	4.25	4.55	4.96	4.83	5.27	5.65	5.1	4.49	3.84	4.25	4.22	-
Fr	Ra	Ac	Th	Pa	U										
-	-	-	3.4	-	3.63										
			Ce	Pr	Nd	Pm	Sm	Eu	Gd	Tb	Dy	Ho	Er	Tm	Yb
			2.9	-	3.2	-	2.7	2.5	3.1	3.0	-	-	-	-	-

2.3.6 Operating Steps of OPV Cells

The electrodes are represented by their work functions, and the organic semiconductors by their LUMO-HOMO levels. Four simple device operational steps under different voltage regimes and I-V curve are shown in Figure 8 and Figure 9, respectively.

(a) Short circuit condition: is when metals shorted together align to same energy level resulting tilting the LUMO-HOMO bands of organic semiconductor layer/layers between electrodes. There is no dark current as no voltage is applied across. The output current is represented by short-circuit current I_{SC}, Figure 9(a). The difference of work functions of the metals creates an internal electric field distributed throughout the device. After excitons dissociation at interface, the holes and electrons are pulled toward higher and lower work function electrode, respectively due to internal field and thus cell generates electricity.

(b) Open circuit condition: is when dark current or diffusion current counter balances the photocurrent or drift current and output light current is zero. LUMO-HOMO energy bands of the semiconductor are almost flat. The applied voltage in this case is a little below the metal work function difference which opposes the built-in electric field.

(c) Reverse bias condition: of the OPV device extracts more charge carriers under stronger electric field and diode works as a photodetector, i.e. extracted charge carriers or photocurrent is proportional to the light intensity.

(d) Forward bias condition: The dark current is almost zero until the open circuit voltage and heavy injection of charge carriers takes place near and after V_{OC}, Figure 9. In this case, there is large recombination and if it is radiative, the device operates as a LED.

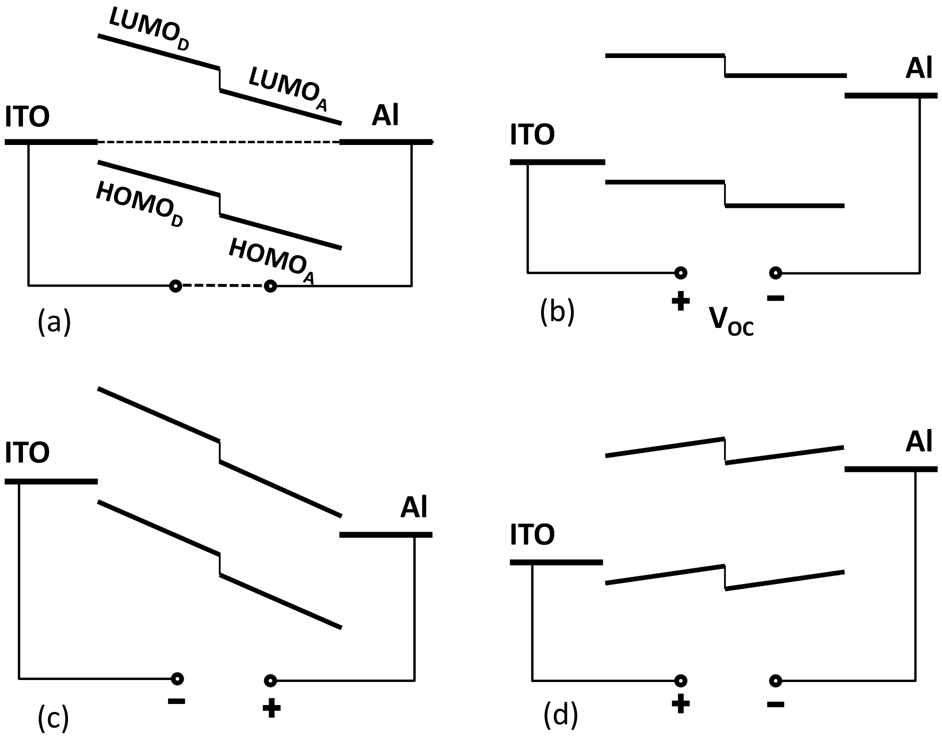

Figure 8: Energy band diagram of a typical OPV cell under (a) short circuit (b) open circuit (c) reverse bias and (d) forward bias.

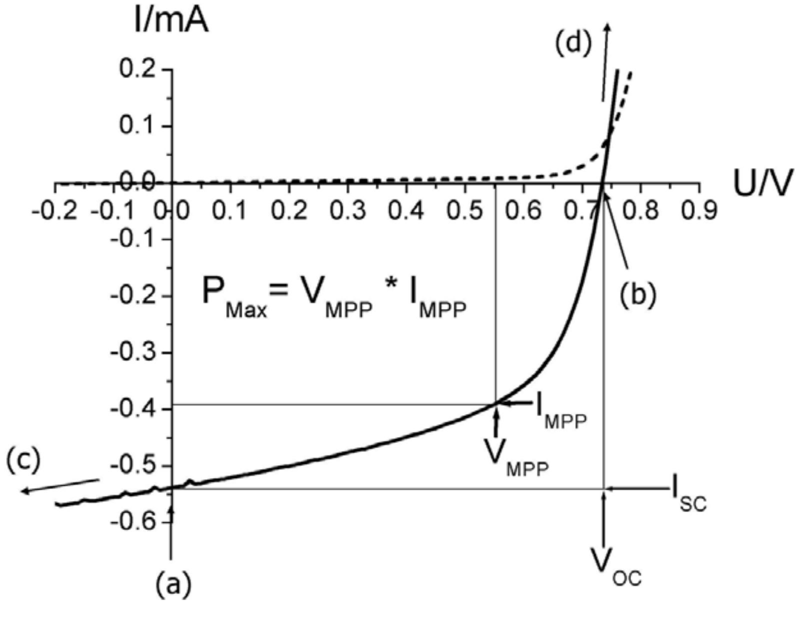

Figure 9: Current-voltage curve of a typical OPV cell (dotted: dark current; solid: illuminated current). (a) short circuit (b) open circuit (c) reverse bias (d) forward bias.

2.4 OPV Architectures:

We will discuss three main types of organic photovoltaic cell structures shown in Figure 10.

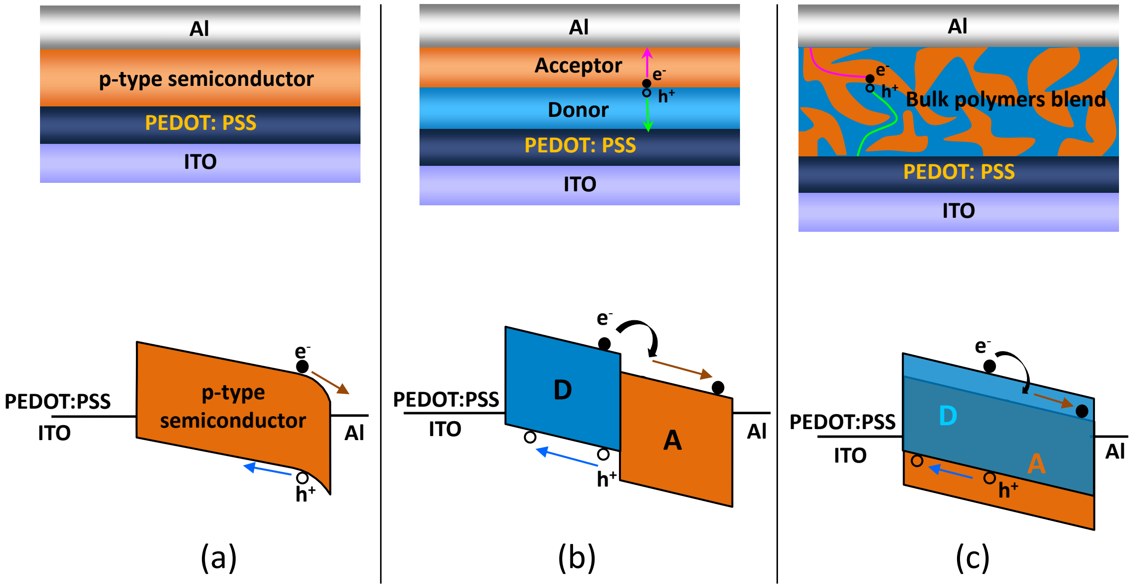

Figure 10: (a) Single layer device (b) Bilayer or planar heterojunction and (c) Bulk heterojunction

2.4.1 Single Layer Device:

The first organic solar cells were based on an organic layer sandwiched between two metal electrodes of different work functions. Such type of cells can be explained by the MIM model or by Schottky barrier formation between a metal of low work function and a p-type semiconducting layer. Band bending of organic semiconductor at the semiconductor-metal interface has been confirmed with Kelvin probe study by H. Ishii et al [74]. Figure 10(a) shows a band bending at the interface between the electrode (Al) and the p-type organic semiconductor where electric field is created due to the bend. Excitons which diffuse towards the Schottky barrier can be dissociated into electrons and holes under this field. Schottky-based organic solar cells using phthalocyanine produced very small photocurrents on the order of $20\mu A/cm^2$, under AM1.5 [17, 75, 76]. Single layer type OPV cells suffer from severe exciton recombination due to insufficient electric field to dissociate excitons; and charge carriers recombination as holes and electrons are generated in the bulk which has higher probability to recombine. Organic layer has to be thin enough as excitons generated near the depletion region or in the near range of exciton diffusion length can contribute to photocurrent.

2.4.2 Planar or Bilayer Structure:

In bilayer device, the active layer consists of two organic semiconductors namely the donor and the acceptor stacked together with a planar interface. Such stacking is done by either sequential spin coating of the solution or thermal evaporation of the donor (D) and the acceptor (A). Unlike in the depleted region of p-n junction solar cells, it does not have an in-built electric field at D-A interface due to absence of doping. Excitons in this case are dissociated more efficiently at the donor-acceptor (D-A) interface due to sufficient LUMOs and HOMOs level differences of these two layers, Figure 10(b). Upon photon absorption, excitons are excited from HOMO to LUMO and diffuse towards the D-A junction where an exciton can be separated by donating an electron from the donor to acceptor or a hole from the acceptor to the donor. The dissociation may take place under the condition when the difference of electron affinity (EA) of the acceptor and ionization potential (IP) of excited state of the donor is greater than exciton binding energy (U_B) or,

$(EA)_A - (IP)_{D*} > U_B$. Similarly, excitons generated in the acceptor can be dissociated at the interface when $(IP)_D - (EA)_{A*} > U_B$. An asterisk mark (*) indicates the excited state condition.

Bilayer devices show majority-carrier transport phenomena as after dissociation, the electron is transferred to the acceptor or n-type layer and the hole is retained in the donor or p-type material. Hence, bulk recombination is not possible in this case. A bilayer solar cell made of copper phthalocyanine (CuPc) and fullerene (C_{60}) as a donor-acceptor pair has showed a power conversion efficiency about 3.6% under AM1.5 [77, 78]. Pentacene based bilayer cells showed efficiencies about 1% - 2.7% [31-34].

Due to concentration gradient, excitons once generated diffuse towards the D-A interfaces. The exciton diffusion length is $L_D = \sqrt{(D\tau)}$, where D is diffusion coefficient and τ is the exciton life-time. Very low exciton diffusion length (few tens of nanometers) [79] limits the thickness of the active layers to about hundred nanometer in order to inhibit exciton quenching before reaching the interface of active layers in the bilayer structure.

2.4.3 Bulk-heterojunction Device:

The donor and the acceptor materials are intimately mixed in a bulk heterojunction (BHJ) type to reduce the distance of interface sites from the point of exciton generation so that the exciton has to travel less than its diffusion length to prevent its recombination. The device should have enough percolated pathways for dissociated charge carriers to reach to their respective electrodes for a useful photocurrent. An extreme intermixing of the blend could be deterrent to such bi-continuous interpenetrating network and hence phase segregation of the components is necessary for efficient charge transport [28, 80-83], Figure 10(c). In BHJ device, donor-acceptor interface is three-dimensional unlike two-dimensional D-A interface in case of bilayer structure. Therefore, in BHJ, the interface area is increased by several folds and exciton dissociation is much more efficient. The active layer thickness could be chosen considerably larger than the exciton diffusion length and this will allow absorbing the light more efficiently. Most common BHJ type OPV cells are made by blend of P3HT: PCBM [27-30] or PPV: PCBM [84-86].

2.5 Properties of Organic Semiconductors

2.5.1 Properties of Conjugated Materials

(a) Hybridization

The backbone of the molecules of organic materials consists of covalent bonded carbon atoms. The wavefunction of the valence electrons is distorted by the surrounding atoms or molecules and atomic orbitals form new hybrid orbitals. Hybridized orbitals are useful in explaining the shape of molecular orbitals. In methane (CH_4), four electrons (2s and 2p) in the outer shell of the carbon atom forms four equivalent sp^3 hybrid orbitals and makes four covalent σ-bonds with neighboring hydrogen atoms. The sp^3-orbitals form a tetrahedral structure with an angle approximately 109° between the orbitals. In ethylene ($H_2C=CH_2$), three electrons (1s and 2p) of the C atom form three coplanar and 120° spaced sp^2 hybrid orbitals (Figure 11) to make σ-bonds with four hydrogen atoms. Another two hybrid orbitals form a σ(C-C)-bond when remaining two *p*-orbitals form a π(C-C)-bond, shown in Figure 12(a) and (b).

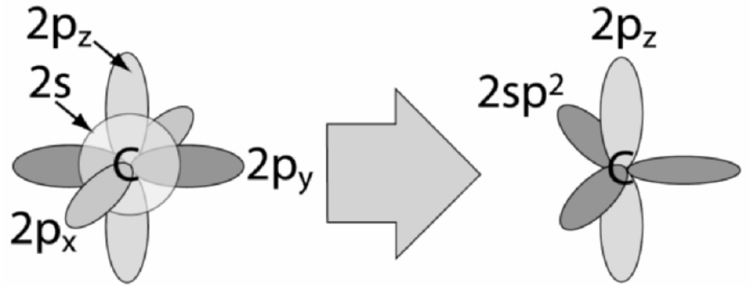

Figure 11: A schematic of sp^2 hybridization of a carbon atom with unhybridized p_z [87].

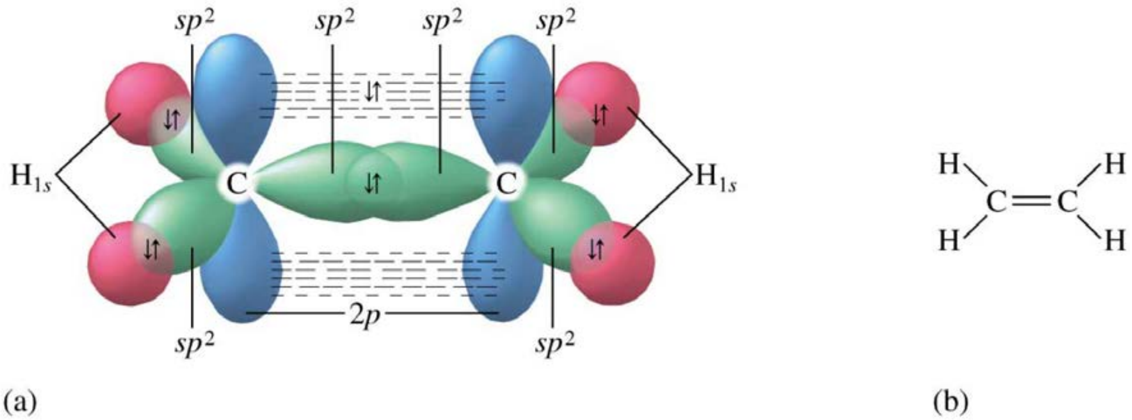

Figure 12: (a) σ and π bonding in ethylene (b) chemical structure

(source: lecture notes - http://depts.washington.edu/chemcrs/bulkdisk/chem162C_spr09/notes_lecture_01_Ch_14.pdf)

(b)LUMO and HOMO energy levels

When two atoms interact with each other to form a molecule, depending on constructive or destructive interference of the atomic orbitals, new wave functions describing the valence electrons are called molecular orbitals, shown in Figure 13. In case of constructive interference, a finite probability of finding an electron between two nuclei acts as a glue to bind them together. These orbitals are called bonding orbitals. If the atomic orbitals undergo destructive interference, there is no probability to find the electrons between the two atoms, thus positive nuclei repel each other. These orbitals are called anti-bonding orbitals. Energy levels when molecular orbitals are formed, split into two - bonding orbitals which are stabilized and have lower energy levels than original atomic level, and - anti-bonding orbitals which are destabilized that are pushed to higher energy levels. Figure 14 shows few dimerization steps of hydrogen molecules in carbon based compounds where at each step, orbitals are split into bonding and anti-bonding orbitals. For a large chain, orbital energy levels are grouped into two compact orbital bands, called valence band with occupied orbitals and conduction band with unoccupied orbitals. The lowest level of the conduction band is called the Lowest Unoccupied Molecular Orbital (LUMO) and the highest level of the valence band is called the Highest Occupied Molecular Orbital (HOMO). LUMO-HOMO energy level and their difference (band gap) mainly determine the optical and electronic properties of an organic semiconductor.

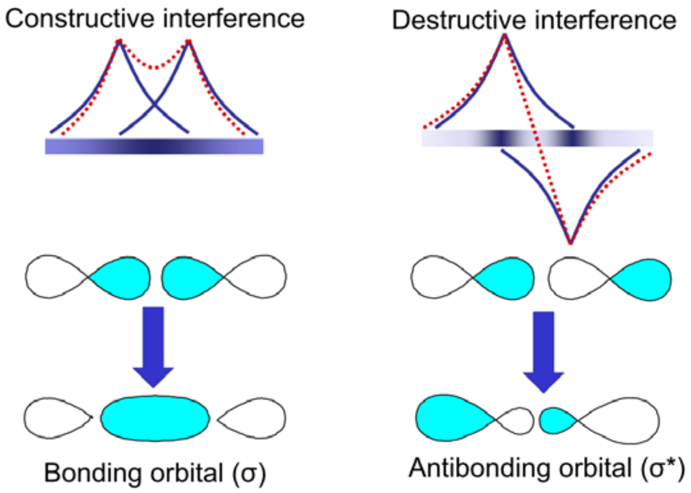

Figure 13: Bonding and anti-bonding orbitals

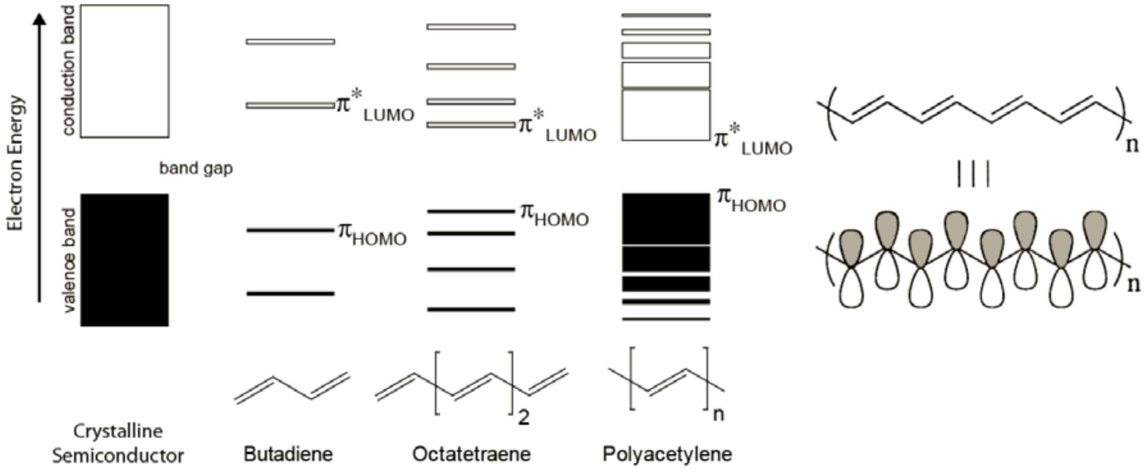

Figure 14: Bonding and anti-bonding energy levels coming together into HOMO and LUMO bands as dimerization length increases. LUMO-HOMO levels are somewhat equivalent to conduction and valence bands in conventional semiconductor (Source: handouts-Excitonic solar cells by Kevin Sivula).

(c) Conjugation

Conjugated molecules have single and double (or multiple) bonds in alternation along their skeleton. Such molecules have connected *p*-orbitals which allow delocalization of *π*-electrons to lower the overall energy of the molecule and increase stability. The basic structure of a conducting or semiconducting organic material is shown in Figure 15 [87]. The compound may be cyclic, acyclic, or mixed. Butadiene ($H_2C{=}CH{-}CH{=}CH_2$) is one of the smallest conjugated molecules and benzene is (C_6H_6) one of the conjugated cyclic compounds with carbon based skeleton. Conjugated systems can easily donate or except delocalized *π*-electrons and these polymers are widely used in donor-acceptor based photovoltaic devices. The large conjugated systems include conductive and semiconducting polymers, carbon nanotube, fullerene etc. The larger is the conjugated *π*-system, smaller is the bandgap, in general.

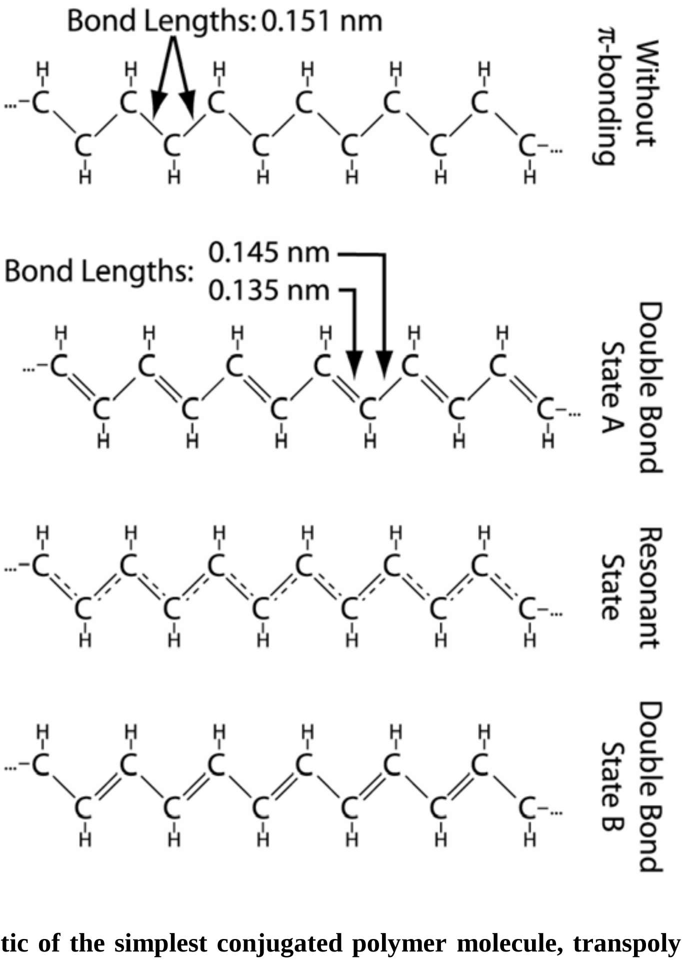

Figure 15: A schematic of the simplest conjugated polymer molecule, transpolyacetylene [87]. The polymer molecules are more stable by interchanging the position of single and double bonds.

2.5.2 Excitons:

Unlike conventional semiconductors where free electron-hole pairs are generated upon light absorption, organic semiconductors create excitons which are essentially quasi-neutral electrostatically bound electron-hole pairs and are not free carriers. The exciton binding energy is about 0.3-0.5eV in organics compared to 0.01eV in conventional semiconductors. To understand more about excitons it is important to examine the difference between conventional semiconductors (CSC) and excitonic semiconductors (XSC).

A charge carrier becomes free when its thermal energy k_BT is equal to or greater than the electrostatic potential energy. For a critical distance r_c between charge carriers:

$$\boldsymbol{E = (q^2/4\pi\varepsilon\varepsilon_0)(1/r_c) = k_B T}$$

where, q is the electronic charge, ε and ε_o are relative and absolute permittivities, respectively. "In a semiconductor with hydrogen-like wavefunctions, the Bohr radius of the lowest electronic state is" [88]:

$$\boldsymbol{r_B = r_0 \varepsilon (m_e/m_{eff})}$$

where, r_o (= 0.53 Å) is the Bohr radius of a hydrogen atom in its ground state, m_e and m_{eff} are the free electron mass in vacuum and effective mass in the semiconductor, respectively. For XSC, effective mass m_{eff} is more than m_e but is opposite in case of CSC. Rearranging the above two equations and we define a ratio γ [88]:

$$\boldsymbol{\gamma = r_c/r_B = [q^2/(4\pi\varepsilon_0 r_0 m_e k_B)][m_{eff}/(\varepsilon^2 T)]}$$

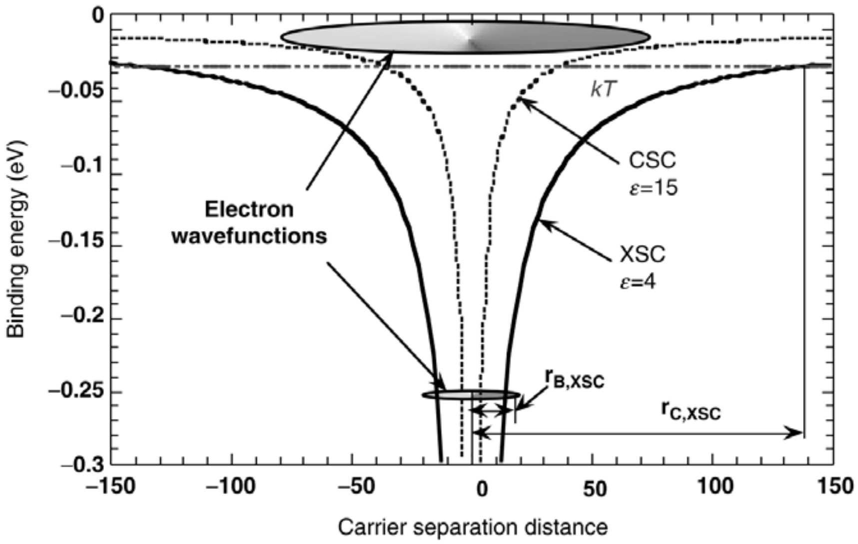

Figure 16: A schematic representing CSCs and XSCs. Wavefunction (r_B) and critical distance (r_c) depend on effective mass, permittivity and the temperature [88]

When $\gamma > 1$, $r_c > r_B$ indicates carriers are not free which is the case for excitonic semiconductor (XSC), and for $\gamma < 1$, $r_c < r_B$ indicates carriers are free suggesting the case in conventional semiconductor (CSC). Although the ratio of r_c/r_B in above equation is only a rough approximation as parameters r_c, r_B, ε, and m_{eff} do not actually have spherical symmetry for XSC, but it's a useful interpretation showing parameters mainly indicate the conditions when excitonic or conventional semiconductors behavior is observed.

According to equations in previous expressions of r_c and r_B, lower relative permittivity ε of XSCs accounts for larger critical distance r_c at a fixed temperature, and the wavefunction r_B is lower for XSC due to its lower value of ε and higher effective mass m_{eff}, indicates $r_c \gg r_B$. Similarly, inverse temperature dependence suggests that at very low temperature T, even CSCs turn into XSCs as $r_c \gg r_B$.

2.5.3 Polarons and Polaron Excitons:

The polarization in a lattice occurs due to electrons repelling its neighboring electrons or negative ions while being attracted towards the nuclei or positive ions in the vicinity. When electron moves through the lattice, it carries the induced polarization as a unit called a polaron, Figure 17. This acts as a potential well which hinders the charge movements and hence decreases the mobility. “In a conjugated molecule, a charge is self-trapped by deformation it induces in the chain. This mechanism of self-trapping is often described through the creation of localized states in the gap between the valence (HOMO) and the conduction (LUMO) bands, as shown in Figure 18 in the case of polythiophene” [89]. A bound pair consisting of an electron polaron and a hole polaron is called a polaron exciton or polaron pair and usually referred to an intermediate state between exciton and dissociated charge carriers.

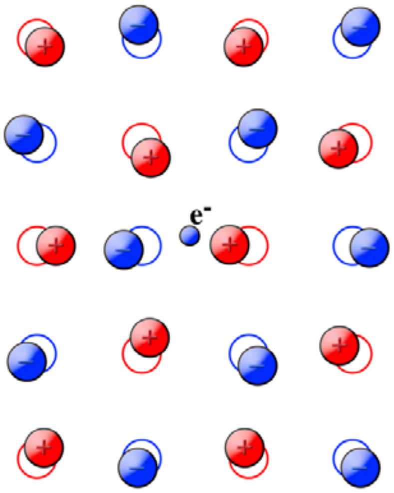

Figure 17: Artist view of a polaron (source: wikipedia)

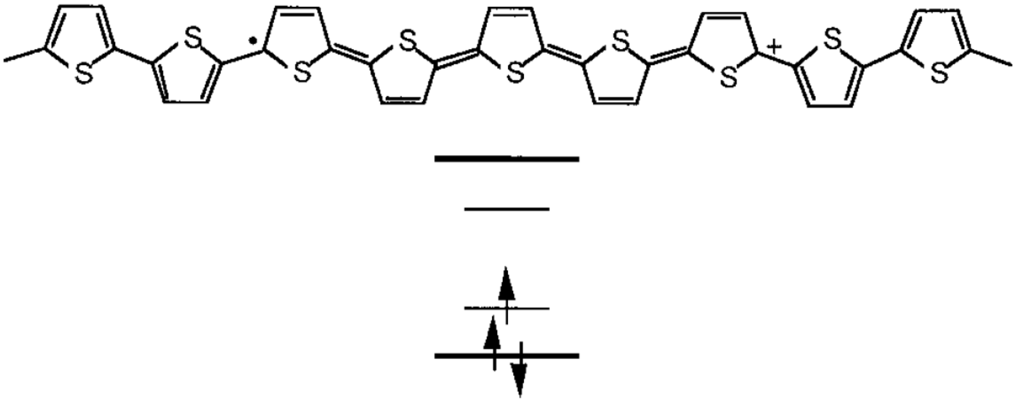

Figure 18: A polaron in polythiophene. *Top*: Change in chemical structure. *Bottom*: Corresponding energy diagram where localized states are created due to polaron formation [89].

2.5.4 Space Charge Limited Photocurrent:

Goodman and Rose, in 1971, presented a simple model and approximate theory for double extraction of uniformly generated electron-hole pairs from a photoconductor [90]. They predicted the electrostatic photocurrent limit in semiconductors at high light intensities. Photocurrent is injected in an external circuit when charge carriers are produced by photons and separated by built-in electric field or external bias. The magnitude of photocurrent depends upon generation, recombination and transport process. Inside the photoconductor (insulator) the mean drift lengths are $w_e = \mu_e\tau_e E$ for electrons, and $w_h = \mu_h\tau_h E$ for holes, where μ's are carrier mobilities, τ's are lifetimes before deep trapping and E is the electric field in the photoconductor. "If both w_e and w_h are much larger than length L of the photoconductor, all of the photogenerated carriers are extracted and no net charge is stored in the photoconductor. If, however, either w_e or w_h or both are smaller than L, trapped charge will accumulate in the layer altering the electric field. The electric field will continue to change until a steady condition is reached in which there is no further net trapping of charge and, consequently, equal currents of electrons and holes are extracted at the contacts" [90]. The same effect has been well studied on PPV based polymer and PCBM blend, and explained by Mihailetchi et al [91]. In the case when all the photogenerated carriers are extracted (w_e and $w_h > L$), photocurrent is saturated and is given by $J_{\mathrm{ph}} = qGL$, with q an electronic charge and G the generation rate of the electron-hole pairs. In case of $w_h \ll w_e$ and $w_h < L$, the holes will accumulate to a greater extent in the device than the electrons, forming space charge resulting in increase in the electric field in the region (L_1) enhancing extraction of holes, Figure 19. Similarly, the electric field decreases near the cathode which reduces the extraction of electrons. In steady state, the modified electric field in the region (L_1) is such that the external hole current equals the external electron current and total voltage V appears across the hole accumulated region ($V_1 \approx V$) and photogenerated current in this region is almost the total current. Therefore, hole drift length $L_1 = \mu_h\tau_h V_1/L_1$ or $L_1 = (\mu_h\tau_h V_1)^{1/2}$ follows that [90, 91]

$$\boldsymbol{J_{\mathrm{ph}} = qGL_1 = qG(\mu_h\tau_h)^{1/2}V^{1/2}}$$

which is termed as ***μτ*-limited** current. Goodman and Rose indicated that a fundamental limit can be expected for the buildup of space charge in a semiconductor at high intensities. At the electrostatic limit, the photogenerated current $J_{ph} = qGL_1$ is equal to ***space-charge limited* (SCL) current**:

$$J_{\mathrm{SCL}} = \frac{9}{8}\epsilon_0\epsilon_r\mu_h\frac{V_1^2}{L_1^3} = qGL_1$$

where, $\epsilon_o\epsilon_r$ is the permittivity of the medium. Solving for L_1 assuming $V_1 \approx V$, the maximum photocurrent that can be extracted electrostatically from the device is [90, 91]:

$$J_{\mathrm{ph}} = q^{3/4}\left[\frac{9}{8}\epsilon_0\epsilon_r\mu_h\right]^{1/4} G^{3/4}V^{1/2}$$

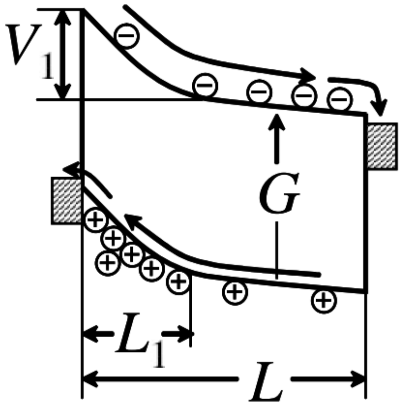

Figure 19: Schematic of energy bands for the photovoltaic device under illumination [91].

In both above equations (*μτ-limited* current) and (*space-charge limited* current) the photocurrent varies as square root of the applied voltage and is governed by slowest charge carrier mobility, however, they differ their dependence on *G* or light intensity. Following are the requirements to observe the space-charge limited current in a semiconductor [91]:

- The material should have high *G* and a long carrier lifetime *τ* after *e*-*h* pair dissociation.
- Charge transport should be strongly unbalanced leading to space-charge formation, i.e. $w_h/w_e \ll 1$ or $\gg 1$.
- Slowest charge carrier should have low mobility to reach the SCL inside the space-charge region.

A blend of conjugated polymers and fullerene molecules can fulfill the above criteria to observe the SCL current. After light absorption, excitons are generated and subsequently dissociated at the interface inside the blend. The photogeneration is ultrafast (< 100 fs) [92] and electron-hole pairs are spatially separated leading to long carrier life times (microsecond to millisecond) [93].

2.5.5 Charge Transport in Organic Materials:

Organic semiconductors have a backbone arising from sp^2 hybridized atomic orbitals of adjacent carbon atoms that overlap to form bonding σ and antibonding σ^* molecular orbitals. The remaining atomic p_z orbitals overlap to a lesser degree form π and π^* molecular orbitals [94]. "The electrical band-gap arises because of the alternation between single and double carbon-carbon bonds, a signature of the Peierls distortion in a 1D system. When a perfect 1D chain of the equidistant carbon atoms is considered, the electronic structure resulting from the electronic coupling between the atomic p_z-orbitals is that of a half-filled π band, implying a metallic character. The introduction of an alternating bond length, however, leads to the formation of a filled π-band and an empty π^*-band, with a gap separating them, thus predicting semiconducting properties" [94].

Charge transport in organic semiconductor is usually described by a hopping model. The mobility edge model is another alternative to hopping model. In the mobility edge model, electronic states are divided into two non-overlapping state distributions – localized or trapped states and delocalized or band states – which are separated by an energy level called the mobility edge [95].

2.5.5.1 Band Transport

If the interaction energy is larger than any energy associated with disorder in the neighbor, charge transport takes place through a band. Band transport can only occur if the bands are wider than the energetic uncertainty of the charge carrier [94].

2.5.5.2 Disordered Based Transport

In crystalline inorganic semiconductors, the atoms are aligned in lattice which allow good orbital overlap between neighboring atoms and delocalization is present throughout the material [96]. Mobility is very high in such materials is limited mainly by phonon scattering. Defects, impurities or dislocations in the lattice induce localization and result in the mobility decrease. In the extreme case, such as in amorphous semiconductors the electronic states become localized over a small volume and charge transfer occurs via hopping mechanism. The mobility in such case is mainly phonon assisted unlike mobility that is limited by phonon scattering in delocalized or band states. In other words, the mobility decreases with temperature in conventional semiconductor whereas it is opposite the case in most of the organic semiconductors.

In disordered organic semiconductors, π-orbitals are weakly overlapped and charge transport depends on the ability of charge carriers to pass from one molecule to another, which is referred to as hopping transport. This is affected by temperature and the electric field across the material. The conductivity is proportional to $T^{-1/4}$ and $\exp(-E_a/k_BT)$ in a low and high electric fields, respectively [97]. A simpler Miller-Abrahams hopping rate is given by [98]:

$$\boldsymbol{\nu_{MA} = \nu_0 \exp\left(-2\gamma R_{ij}\right) \exp\left\{-(\varepsilon_j - \varepsilon_i)/k_\mathrm{B}T\right\},\ \ \varepsilon_j > \varepsilon_i}$$
$$\boldsymbol{\nu_{MA} = \nu_0 \exp\left(-2\gamma R_{ij}\right),\ \ \varepsilon_j < \varepsilon_i}$$

where, the carrier hops from site *i* with energy ε_i to site *j* with energy ε_j, and the distance between these sites is R_{ij}. γ is the inverse localization radius tells that how well charge carriers can tunnel from site *i* to site *j*, k_B is Boltzman's constant. The energy difference plays a role in hopping rate only when the second hopping site has the higher energy than the first one, otherwise the second exponent part is 1. The first exponent part is tunneling contribution and the second exponent shows the thermally activated upward hopping.

In disordered systems, the barriers created by energetic disorder can be overcome at higher temperatures and the hopping transport is improved. An Arrhenius-like model is used to model the temperature dependence of mobility for disordered systems and is given by,

$$\boldsymbol{\mu = \mu_\infty \exp\left(-\frac{\Delta}{k_B T}\right)}$$

where, Δ is the activation energy which typically increases with the amount of disorder [99].

In mobility edge model (contrast to the hopping model), charge carriers in the localized or trap states are completely immobile. These carriers contribute to transport only if they are thermally activated into the band states, i.e. thermal energy $k_\mathrm{B}T$ > trap energy. In organic semiconductors, traps are created by structural defects and impurities causing a different set of HOMO-LUMO values that falls within the HOMO-LUMO levels of the intrinsic semiconductor. In homogeneous traps, the mobility is expressed as

$$\boldsymbol{\mu = \mu_0 \alpha \exp\left(-\frac{\Delta E}{k_B T}\right)}$$

where, ΔE is the trap energy, μ_o is mobility in delocalized states, and α a constant [99].

2.6 Parameters affecting OPV performance

We have to consider many factors while designing an organic solar cell. The most important ones including mobility, HOMO-LUMO matching of donor-acceptor materials, electrode work-functions, and layer thicknesses are presented below.

2.6.1 Mobility:

Disordered organic polymers have mobility values orders of magnitude lower than inorganic crystals. One question we would like to answer is whether low mobility always limits the performance of the organic solar cell and if polymers with higher mobility will perform better. Higher mobility, on one hand, leads to efficient charge extraction, but on the other hand, it can cause an increased rate of charge carrier recombination at the donor-acceptor interface. As reported in [100], increases in mobility beyond what is required for efficient charge extraction lead to lower efficiency because of increased recombination . In bilayer structure modeling which is exclusively studied in the next Chapter, the Langevin recombination rate which is proportional to the product of summation of mobilities and charge carrier concentration at D-A interface has been used. It has been shown that at higher mobilities, the efficient charge extraction strongly reduces the charge carrier concentration at D-A interface reducing the open-circuit voltage [101, 102]. Authors found theoretically that the optimal power efficiency of a bulk heterojunction organic solar is achieved for a mobility of about 10^{-2} cm^2/V.s [100-103].

A simulation program solving the Poisson differential equation, and the continuity equation using a drift-diffusion model describes the performance vs mobility of a bulk heterojunction ($\mu_e = \mu_h$) in [102]. The results are shown in Figure 20. The short-circuit current density (J_{SC}) saturates above a carrier mobility of 10^{-2} cm^2/V.s and there is a sharp decrease in open-circuit voltage (V_{OC}) for mobilities greater than 10^{-4} cm^2/V-s. Combined, these effects cause the power conversion efficiency to reach a maximum near these values. The model considers the reduced Langevin-type polaron recombination rate R [102, 104]:

$$\boldsymbol{R = \zeta\gamma(np - n_i p_i)}$$

where, ζ is a prefactor considering the reduction in bimolecular Langevin recombination. Since only a fraction of the total phase segregated volume of active materials take part in recombination at D-A interface and there is imperfect bi-continuous interpenetrating network in the blend, γ is modified by the prefactor ζ. The Langevin recombination parameter is given by [100, 104, 105]:

$$\boldsymbol{\gamma = \frac{q}{\varepsilon}(\mu_e + \mu_h)}$$

where, q is electronic charge and ε is the permittivity of the medium, n (p) is the free electron (hole) densities and n_i (p_i) is intrinsic electron (hole) density.

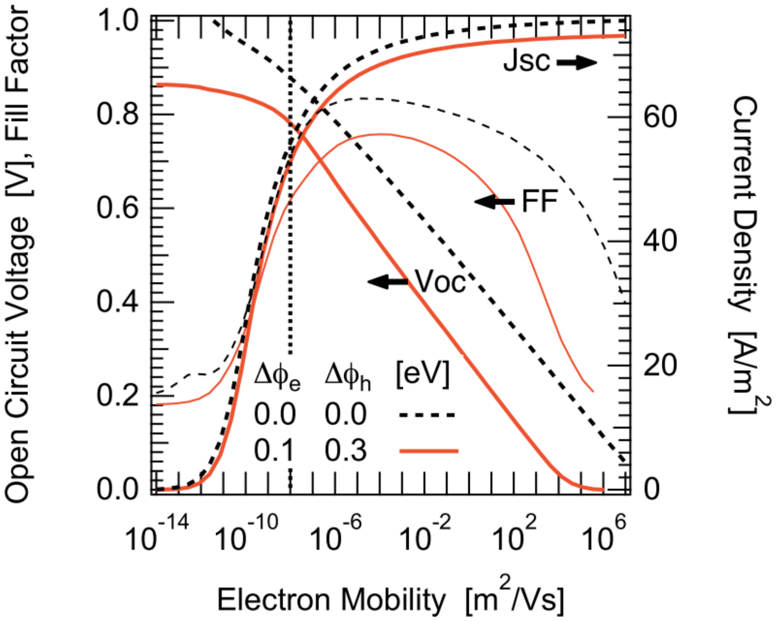

Figure 20: Open-circuit voltage, short-circuit current density and fill-factor dependence on the carrier mobility, for two sets of injection barriers [102]. Note that SI units are used.

Figure 21(a) depicts that at lower mobility, the inefficient charge extraction leads to space-charge build up that forms high carrier concentrations. The performance is poor mainly due to low mobility (μ_e ~ 7×10^{-11} m^2/V.s, PCE = 0.5%). Efficient charge extraction at high mobility leads to depletion of charge carriers (μ_e ~ 2×10^{-2} m^2/V.s, PCE = 0.5%), Figure 21(c). Therefore, such high carrier concentration reduces quasi-Fermi level splitting resulting in lowering the open circuit voltage and hence overall PCE after a certain mobility. The maximum achievable efficiency (at μ_e ~ 10^{-6} m^2/V.s, PCE = 3.0%) would be a trade-off between high mobility (causing high carrier extraction and low open-circuit voltage) and low mobility, leading to low short circuit current, shown in Figure 21(b).

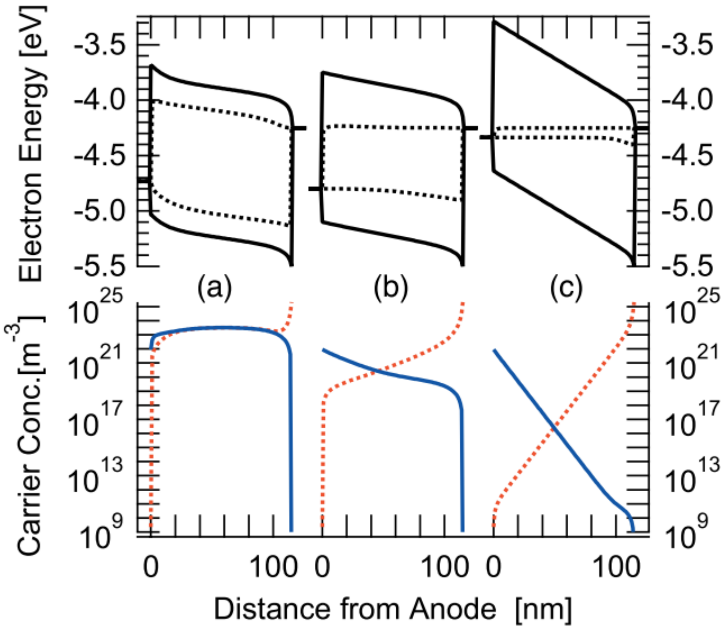

Figure 21: (Top) Band diagrams (solid), electron and hole quasi-Fermi levels (dotted). (Bottom) electron (dotted) and hole (solid) concentrations at maximum power point for (a) $\mu_e \sim 7\times10^{-11}$ m^2/V.s, PCE = 0.5%, (b) $\mu_e \sim 10^{-6}$ m^2/V.s, PCE = 3% (max) and (c) $\mu_e \sim 2\times10^{-2}$ m^2/V.s, PCE = 0.5% [102].

2.6.2 Phase Morphology:

In bulk heterojunction (BHJ) solar cells, morphology plays an important role. Very fine grained ultimate phase mixing of D-A pair would be ideal for effective exciton dissociation but may not be great for charge transport due to poor bi-continuous path formation. On the other hand, extreme phase segregation will not be effective in terms of exciton dissociation due to reduced heterojunction area. Hence a trade-off between efficient dissociation and transport is required.

Different D-A ratios or thermal annealing experiments have been done in order to influence the device performance by changing the nanomorphology of PPV:PCBM [80], P3HT:PCBM [28, 81, 82]. Thermal annealing could improve the photocurrent by up to one order of magnitude [83]. Annealing was found to increase the size of PCBM aggregates and also P3HT crystallinity [106]. The polymer fiber growth in P3HT: PCBM by annealing is confirmed by transmission electron microscopy [107].

A vertical phase segregation also showed the improvement in device performance by graded higher concentration of donor at anode and acceptor at cathode [108, 109]. This helps collecting holes at anode and electrons at cathode more effectively.

Phase morphology in case of bilayer cell is helpful up to some extent as mobility is improved due crystallinity of the material by annealing and interpenetration of D-A at the interface making a pseudo bulk heterojunction type structure [110].

2.6.3 HOMO-LUMO levels and electrode work functions:

For efficient charge separation at the D-A interface, the difference of LUMOs and HOMOs should be more than exciton binding energy (0.3-0.5 eV). Lower value will make inefficient charge separation whereas quite large value will account for the loss of energy. Similarly, the work function of anode (cathode) should be smaller (larger) but as close to the donor-HOMO (acceptor-LUMO) as possible in order to minimize the voltage loss. The theoretical open circuit voltage is the difference of donor-HOMO and acceptor-LUMO should be chosen larger as possible. Again, quite larger value may not absorb the sunlight efficiently and hence reduce the short circuit current and so the overall efficiency. The optimal band gap for plastic photovoltaics has been theoretically predicted to about 2.0 eV [111].

2.6.4 Layer Thickness:

In case of a bilayer structure, a thicker active layer will absorb more photons and generate more excitons but the excitons may recombine before they reach the interface due to the very short diffusion length (< few tens of nm) that limits the material thickness to ~100nm for efficient exciton dissociation. In the bulk heterojunction structure, thicker layers will absorb more light but still can downplay the performance due to lower probably of bi-continuous path formation and increased chance of recombination for larger thickness. Therefore, the thicknesses of photoactive layers need to be optimized.

2.6.5 $\mu\tau$-Product Balance:

Mean drift length ratio defined by (b = $\mu_e\tau_e/\mu_h\tau_h$) the ratio of mobility-lifetime products of electrons and holes directly affects the illuminated *J-V* response in case of ohmic contacts (non-injecting in reverse bias) [90]. Severe $\mu\tau$-imbalance (b≪1 or ≫1) creates a space charge build up and a transition of ohmic conductivity to SCL current takes place. In such case, *J-V* characteristics shows a S-kink effect [112] and causes reduced fill-factor [43, 59, 113]. In case of SCL where photocurrent closely follows 1/2 power dependence on applied voltage, maximum possible fill-factor limited to only 42% [91].

From our simulation results in the next Chapter, we confirm it is not the mobility imbalance which causes the PCE drop but the lower mobility among two mobilities plays the dominating role to reduce the PCE for one or both mobilities lower than the optimum mobility. For mobilities above optimum mobility, if one of the mobilities is increased, PCE decreases, and that is because of increase in mobility after optimum value and not because of the imbalance.

2.7 Photovoltaic Cell Parameters

2.7.1 Equivalent Circuit Diagram

Equivalent circuit diagrams (ECDs) are used to characterize the electrical behavior of semiconductor devices with a network of electrical components. A solar cell can be modeled as a diode in parallel with a constant current source and a shunt resistor, and a series resistor shown in Figure 22.

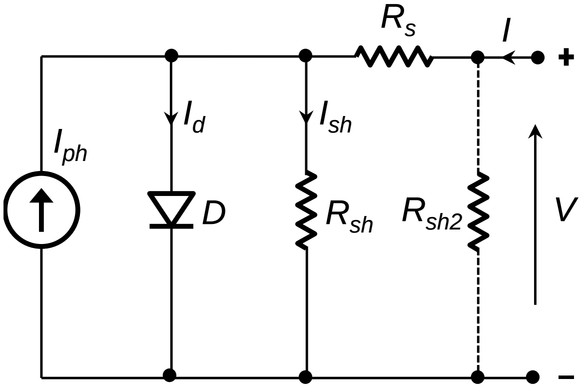

Figure 22: Equivalent circuit diagram for a photovoltaic cell

- **Current source I_{ph} and diode D:** I_{ph} = photocurrent generated by the current source upon illumination before any recombination can take place. I_d = current through the diode D. I_{sh} and I = current through the shunt resistance R_{sh} and R_s respectively. I and V = output current and voltage, respectively. We can formulate the relation:

  $$I + I_{ph} = I_d + I_{sh} = I_d + \frac{V - IR_s}{R_{sh}}$$

  where, current through the ideal diode D is given by Shockley diode equation:

  $$I_d = I_0\left(e^{\frac{q(V-IR_s)}{nkT}} - 1\right)$$

  Rearranging the above two equations, we get the expression of output current I with function of output voltage V:

  $$I = \frac{R_{sh}}{R_{sh} + R_s}\left[\frac{V}{R_{sh}} - I_{ph} + I_0\left(e^{\frac{q(V-IR_s)}{nkT}} - 1\right)\right]$$

  The short circuit current I_{SC} ($I|_{V=0}$) reduces to photocurrent I_{ph} considering diode current is negligible in this case.

- **Shunt resistors R_{sh} and R_{sh2}:** Loss due to recombination of charge carriers near the dissociation sites is represented by R_{sh}. For very small voltages, the diode D does not conduct and the shape of the I-V curve is mainly dominated by the shunt resistance (given $R_{sh} \gg R_s$) which can be derived to:

$$R_{sh} \approx \left[\frac{dI}{dV}\right]_{V\approx 0}^{-1}$$

Sometimes an extra shunt resistor *R_{sh2}* at the output is also considered representing shorts caused by pinholes or conductivity of the bulk material. It also accounts for recombination losses near the electrodes.

- **Series resistor R_s:** Mobility of the charge carriers in PV cell or conductivity can collectively be transferred into a series resistor R_s. It can be adversely affected by space charges, traps, barriers at contacts or thickness of the transport layers. The slope of the *I*-*V* curve can be expressed as:

$$\frac{dI}{dV} = \frac{R_{sh}}{R_{sh} + R_s} I_d \frac{q}{nkT}\left(1 - R_s \frac{dI}{dV}\right)$$

For high forward bias voltages, diode current $I_d \gg I_{sh}$ and the shape of the *I*-*V* curve is dominated by series resistor R_s and the above equation can reduced to:

$$R_s \approx \left[\frac{dI}{dV}\right]_{V\geq V_{OC}}^{-1}$$

To achieve high fill factor, low series resistance and high shunt resistance is desirable.

2.7.2 Open Circuit Voltage:

The open circuit voltage is mainly governed by two energy levels: (1) the effective band gap which is the difference of LUMO level of acceptor and HOMO level of donor ($E_{g,DA}$= $LUMO_A$ – $HOMO_D$), and (2) the difference of the work functions of the electrodes (ΔW_f). In case of bulk heterojunction (BHJ) the bands are parallel which is true for very fine intermixing of the blend constituents. In contrast, a band bending is possible for bilayer solar cells as D-A has only one heterojunction interface and there is large layer width for space charge formation [114].

Cheyns et al considered the thermionic emission at the injection barriers and showed that band bending effect is nullified by injection barriers [115]:

$$\boldsymbol{V_{OC} = \frac{E_g}{q} - \frac{kT}{q}\ln\left(\frac{N_A N_D}{n_i p_i}\right)}$$

Here, E_g is the effective bandgap; kT/q is the thermal voltage; N_D and N_A are the effective density of states (DOS) of donor and acceptor, respectively, p_i and n_i are the hole and electron concentration respectively at the D-A interface.

For BHJ, Koster et al derived the equation for V_{OC} which is based on the quasi-Fermi level difference [116]:

$$\boldsymbol{V_{oc} = \frac{E_g}{q} - \frac{kT}{q} \ln\left(\frac{(1-P)\gamma N^2}{PG}\right)}$$

Here, P is the exciton dissociation probability; G is the exciton generation rate; N is the effective density of states; γ is the Langevin recombination strength.

Scharber et al. determined $\mathbf{V_{OC} = |HOMO_D - LUMO_A|/q - 0.3\ V}$ [117]. The difference of 0.3eV below the effective band gap includes the energy needed for exciton dissociation, energetic disorder and band bending due to charge carrier diffusion.

2.7.3 Efficiencies and Fill Factor:

The sum of the total absorptance (A), transmittance (T), and reflectance (R) must be unity, $A + T + R = 1$. Absorptance of the active layer, η_A = number of photons absorbed in the layer/number of incident photons to the cell.

Internal Quantum Efficiency (IQE) is the quantity defined by ratio of number of electrons in external circuit to number of photons absorbed.

External quantum efficiency EQE or Incident Photon to Current Efficiency (IPCE) of the device is defined by the ratio of number of electrons generated to incident photons in a given time. EQE includes optical losses such as transmission and reflection. This is experimentally determined and measured for monochromatic light. Number of electrons generated/cm^2.s = J_{SC}/e, where J_{SC} is short-circuit current density (A/cm^2) and e is an electronic charge (C). Number of photons generated/cm^2.s = I_λ/E_λ, where, I_λ is the incident light intensity (W/cm^2) and E_λ (=1240×e/λ) is the energy (J) of a photon of wavelength λ (nm), respectively. Therefore,

$$\boldsymbol{IPCE = 1240.J_{\mathrm{SC}}/(\lambda.I_\lambda)}$$
$$\boldsymbol{EQE = \eta_A.IQE}$$

Quantum efficiencies relate the electrical sensitivity of the solar cell to particular wavelength of light and they are often measured over a range of wavelengths. QE does not give information of the overall power conversion efficiency with respect to incident light power.

Power conversion efficiency (PCE) which is the most important parameter in photovoltaics is defined by the ratio of the maximum attainable electric output power from the cell to incident power of light spectrum of interest (or sunlight) to the cell. The current density versus output voltage; and output power versus output voltage has been shown in Figure 23. At point (V_m, I_m) the output power $P_m = (I_m \times V_m)$ is maximum. For a PV cell, the quality of shape of I-V curve is defined by the ratio of the maximum power that can be drawn from the cell and the maximum ideal power output ($I_{SC} \times V_{OC}$). This ratio is called the cell's fill-factor, $\boldsymbol{FF = (I_m \times V_m)/(I_{SC} \times V_{OC})}$. The power conversion efficiency (PCE) for input power P_{in} is defined:

$$PCE = I_m V_m / P_{in} = I_{SC} V_{OC} FF / P_{in}$$

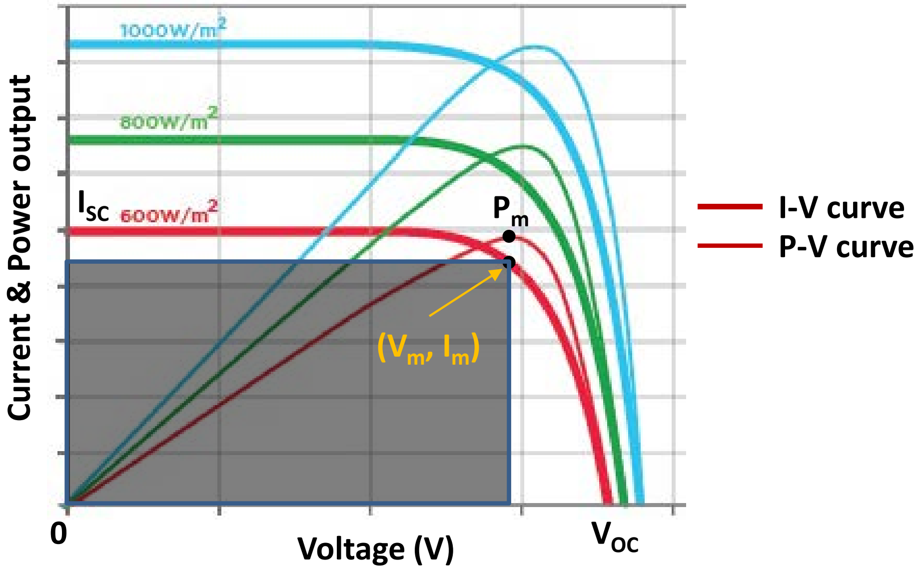

Figure 23: Current and output power versus terminal voltage, i.e. I-V and P-V curve.

If bandgap is wider, open circuit voltage is more. But photons with energy smaller than the bandgap will not be absorbed therefore photon absorption will be less that will lead to reduced short circuit current and vice versa. There must be an optimal bandgap for a given illumination spectrum for which efficiency is at maximum. Shockley and Queisser were the first who theoretically calculated the maximum PCE of 33.7% for a semiconductor with a bandgap of 1.34eV and 29% for silicon with bandgap of 1.12eV [118].

3. Device Model for Organic Solar Cell

3.1 Introduction

The potentially inexpensive and simple fabrication processes for organic solar cells is a key motivation for the scientific community to explore various new polymer materials. However, the low power conversion efficiency and the material degradation is a major roadblock to use such cells for commercial applications. There are many factors that affect the cell performance such as the organic material's charge carrier mobility, mobility imbalance, active layer thickness, exciton diffusion length, optical band gap, absorptivity of sun spectrum. Hence, it becomes important to model the OPV cell to investigate the performance for various parameters and optimization. We are investigating a bilayer OPV cell with the existing model of exciton generation [119] and charge carrier transport with known parameters [120]. Electric field at the D-A interface used by Ray et al. [120] is unaffected by space charge formation while it is changed considerably when hole and electron mobilities are different or donor and acceptor layer thicknesses are not the same. We present a more accurate calculation of electric field at the D-A interface that is needed to solve the two-boundary-valued problem. We have optimized the design for mobility and layer thicknesses of donor and acceptor using our modified model. We also study the effect of increasing mobility of one type of charge carrier (either hole or electron) or making mobilities imbalanced.

3.2 Device Operation and Model System

3.2.1 Exciton Model of Photocurrent Generation

The exciton flux to the donor-acceptor (D-A) interface of the in bilayer organic solar cell is calculated based on layer thickness, exciton diffusion length, exciton dissociation and recombination properties, and spectral absorption. The model is based on following assumption:

- Incident light is perpendicular to active layer surfaces. Scattering or reflection and interference are ignored.
- Light intensity has an exponential decay following Beer-Lambert's law.
- Dissociation occurs at D-A interface only.
- All excitons recombine at the electrodes.

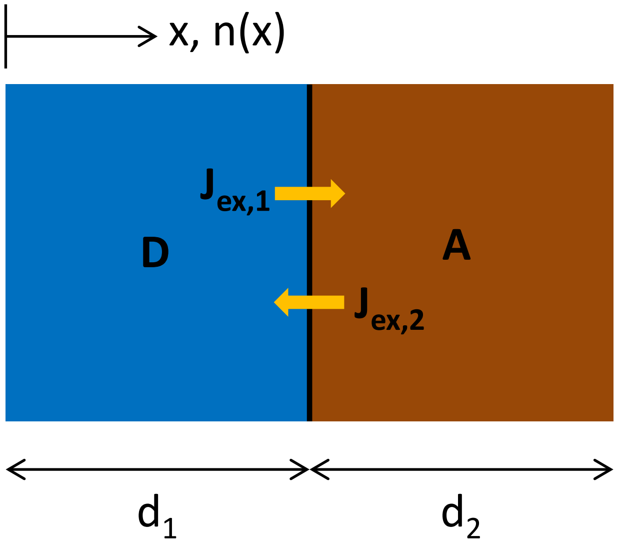

Figure 24: Active bi-layers of organic solar cell with light incidents at *x*=0. D-A interface is at x=d_1

Figure 24 shows the active bilayers with layer thicknesses d_1 (for front layer or illuminated side) and d_2 (for back layer) of the cell where light incidents at x=0. According to Beer-Lambert's law, photon flux density at a distance x is $\phi = \phi_0 e^{-\alpha x}$, where wavelength dependent $\phi_0$and α are incident photon flux density and absorption coefficient of the material, respectively. The exciton generation rate G_{ex} and recombination rate R_{ex} at a distance x are

$$G_{ex} = -\frac{d\phi}{dx} = \alpha\phi_0 e^{-\alpha x};\ \ R_{ex} = n_{ex}/\tau_{ex}$$

We first model the exciton diffusion in the donor layer. We will then generalize the expression to the acceptor layer with minor modifications. At the metal-semiconductor junction (x=0) where excitons are quenched and the D-A interface (x=d_1) where excitons are completely dissociated, the exciton concentration is zero. Exciton diffusion is described by a second order differential equation and with the appropriate boundary conditions can be written as:

$$D\frac{d^2 n_{ex}}{dx^2} + \alpha\phi_0 e^{-\alpha x} - \frac{n_{ex}}{\tau_{ex}} = 0$$

$$n_{ex}(x = 0) = 0;\ \ n_{ex}(x = d_1) = 0$$

where, n_{ex} is the exciton concentration at x, D is the diffusion constant of the excitons, α is the absorption coefficient, Φ_o is the photon flux density, d_1 is the donor layer thickness, τ_{ex} is the exciton life-time, L_{Dex} is the exciton diffusion length, $\beta = 1/L_{Dex} = 1/\sqrt{(D_{ex}\tau_{ex})}$. The solution for n_{ex}, exciton flux density J_{ex} at distance x are given by[119, 121],

$$n_{ex} = \frac{\alpha\phi_0}{D(\beta^2 - \alpha^2)}\left\{\frac{\left(e^{\beta d_1} - e^{-\alpha d_1}\right)e^{-\beta x} - \left(e^{-\beta d_1} - e^{-\alpha d_1}\right)e^{\beta x}}{(e^{-\beta d_1} - e^{\beta d_1})} + e^{-\alpha x}\right\}$$

$$J_{ex} = -D\frac{dn_{ex}}{dx}$$

Now, exciton flux density at the interface due to front layer $J_{ex,1}$ and back layer $J_{ex,2}$ has to be calculated separately using above equations and are expressed as follows[119],

$$J_{ex,1} = \frac{\alpha_1\phi_0 e^{-\alpha_1 d1}}{\left({\beta_1}^2 - {\alpha_1}^2\right)}\left\{\alpha_1 - \beta_1 + 2\beta_1\frac{e^{\beta_1 d_1} - e^{\alpha_1 d_1}}{e^{\beta_1 d_1} - e^{-\beta_1 d_1}}\right\}$$

$$J_{ex,2} = \frac{-\alpha_2\phi_0 e^{-\alpha_1 d1}}{\left({\beta_2}^2 - {\alpha_2}^2\right)}\left\{\alpha_2 - \beta_2 - 2\beta_2\frac{e^{-\beta_2 d_2} - e^{-\alpha_2 d_2}}{e^{\beta_2 d_2} - e^{-\beta_2 d_2}}\right\}$$

$$J_{ex,i} = J_{ex,1} + J_{ex,2}$$

where, $J_{ex,i}$ is total exciton flux density at the D-A interface with the assumption of complete dissociation of excitons at the interface.

The total generated current density J_G for the whole incident light spectrum is obtained by integrating with respect to wavelength λ.

$$J_G = \int J_{ex,i}\big(\alpha(\lambda), \phi_0(\lambda)\big)d\lambda$$

3.2.2 Carrier Transport

Once the excitons are dissociated at the interface the charge carriers move towards the respective electrodes under internal electric field and diffusion with hole and electron currents confined exclusively within the donor and acceptor materials, respectively. Due to the absence of minority carriers, recombination takes place mostly at the interface and not in the bulk (we neglect bulk recombination). Carrier transport is modeled by the Poisson equation and the continuity equation with appropriate drift-diffusion formulations and recombination models [120, 122, 123].

1. **Poisson equation:**

$$\frac{d^2\psi}{dx^2} = \frac{q}{\varepsilon}[n_e - n_h]$$

ε is the permittivity, and ψ is the electric potential, $n_{e(h)}$ are charge carrier concentrations of electrons and holes.

2. **Continuity equation:**

$$\frac{dJ_e}{dx} = -q[G_e(n_{ex}) - R_e(n_e, n_h)]$$

$$\frac{dJ_h}{dx} = q[G_h(n_{ex}) - R_h(n_e, n_h)]$$

where, $J_{e(h)}$ is the current density, $G_{e(h)}$ and $R_{e(h)}$ are charge carrier generation and recombination rate respectively. In the case of a bilayer device, $dJ_{e(h)}/dx=0$ in the bulk.

3. **Recombination equation [123, 124]:**

$$R_{e(h)} = \gamma[n_e n_h - {n_{int}}^2]$$

$$\gamma = \frac{q}{\varepsilon}(\mu_e + \mu_h)$$

where, R is the recombination rate, γ is the Langevin recombination strength, n_{int} is the intrinsic carrier density at the D-A interface. Following assumptions are made for charge carriers recombination in bilayer structure; (i) All the excitons are dissociated at D-A interface, $J_h = J_e = J_{ex,i}$ (ii) Excitons are dissociated within a very small D-A interface width of w_{int} only and charge carrier generation in D-A interface width is $J_{ex,i}/w_{int}$ per volume (iii) Recombination happens only within this D-A interface width w_{int} and not beyond that. D-A interface width shall not be smaller than 0.1 nm which is an approximate thickness of an atom. In a typical case of mobilities $\mu_h = \mu_e$

= 10^{-5} cm^2/V-s, when D-A interface width w_{int} was changed in our simulation from 0.1nm to 1nm (10 times), PCE decreases by less than 25%. Further increment in w_{int} does not change the PCE very much. Ray et al. have selected the D-A interface width of 1nm [120] and we have selected w_{int} = 0.8nm, randomly between 0.1 to 1nm.

$$\frac{dJ_{e(h)}}{dx} = \mp q\left(\frac{J_{ex,i}}{w_{int}} - R_{e(h)}\right); \quad \text{for } |x| \leq w_{int}$$

4. Drift-diffusion equation:

$$J_e = q\left[n_e\mu_e E + D_e\frac{dn_e}{dx}\right]$$

$$J_h = q\left[n_h\mu_h E - D_h\frac{dn_h}{dx}\right]$$

where, $\mu_{e(h)}$ are the charge carrier mobilities, $D_{e(h)}$ are the diffusion coefficients and E is the electric field.

5. Hole boundary condition:

The hole concentration in donor HOMO at the anode junction can be expressed as:

$$n_h(x=0) = N_v e^{-\frac{HOMO_D-\phi_a}{kT}}$$

6. Electron boundary condition:

The electron concentration in acceptor LUMO at the cathode junction can be expressed as:

$$n_e(x=d) = N_c e^{-\frac{\phi_c-LUMO_A}{kT}}$$

where, d is the the total thickness (d_1+d_2) of the active bilayer, ϕ_a and ϕ_c are anode and cathode work functions, HOMO$_D$ and LUMO$_A$ are HOMO of the donor and LUMO of the acceptor, respectively, $N_{c(v)}$ are the effective density of states for $LUMO_A$ and $HOMO_D$.

7. Electric field boundary condition:

For solving the two-boundary-value problem, it is necessary to calculate the electric field at the D-A interface. An approximation of the electric field E_I at the interface $x = d_1$ is proposed by Ray et al [120] and expressed by

$$E_I = \frac{V_{bi} - V}{d}$$

where, V_{bi} built-in potential, V applied voltage, $d=d_1+d_2$ total film thickness. However, the electric field is not uniform between electrodes and is nonlinearly modified by the space charge distribution. We in this thesis, calculate the accurate electric field at the interface by an iteration process. With an initial guess of E_{I} given above, we get a solution for electric field and integrate with respect to distance through the thickness of the active layer to calculate the potential drop. The actual total potential drop from anode to cathode due to band alignment should be built-in voltage less applied voltage, i.e. $V_{\mathrm{bi}} - V$. Any error will accordingly modify the E_{I} for the next iteration until it is less than a tolerance value (0.001V). The two-boundary-value problem itself is solved by an iterative process hence solving for the interfacial electric field is an iterative process using one loop inside another loop.

3.3 Simulation Results and Discussion

The simulation parameters and their values used are given in Table 2. Fixed parameters of exciton diffusion lengths in donor and acceptor, effective density of states of donor-HOMO and acceptor-LUMO, relative permittivity, and diffused D-A interface width are used from a literature [120].

Table 2: Simulation Parameters

d_1, d_2	Thickness of front and back layers	(10 to 90nm)
μ_e, μ_h	Mobility of electron in acceptor and hole in donor	(10^{-7} to 10^{-2}) cm^2/V/s
w_{int}	Effective width of the diffused D-A interface	0.8nm
L_{Dex}	Exciton diffusion lengths in donor and acceptor	20nm, 5nm
N_c, N_v	Effective density of states	10^{21} /cm^3
ε_r	Relative permittivity	3
D_e, D_h	Diffusion coefficients of electrons in acceptor and holes in donor	$k_{\mathrm{B}}T\mu_{e(h)}/q$
γ	Langevin bimolecular recombination strength	/cm^3/s
n_{int}	Intrinsic carrier density at D-A interface	10^{11} /cm^3
$LUMO_{\mathrm{D}}$	Lowest unoccupied molecular orbital of donor	3.0 eV

$HOMO_{\mathrm{D}}$	Highest occupied molecular orbital of donor	4.9 eV
$LUMO_{\mathrm{A}}$	Lowest unoccupied molecular orbital of acceptor	3.7 eV
$HOMO_{\mathrm{A}}$	Highest occupied molecular orbital of donor	6.0 eV
Φ_c	Cathode work function (Al)	3.9 eV
Φ_a	Anode work function (ITO)	4.7 eV
Φ_o	Wavelength dependent photon flux density	/cm^2/s
α	Wavelength dependent absorption coefficient	/cm
R_{ex}	Exciton recombination rate	/cm^3/s
G_{ex}	Exciton generation rate	/cm^3/s
n_{ex}	Steady state exciton density	/cm^3
$R_{e(h)}$	Carrier recombination rate near the interface	/cm^3/s
J_G	Generated current density at the interface	mA/cm^2
$J_{e(h)}$	Electron (hole) current density in acceptor (donor)	mA/cm^2

We study the effect of changing the mobility of holes in donor and electrons in acceptor on various output parameters such as open circuit voltage, short circuit current, fill-factor and power conversion efficiency of the OPV device. We also study the effect of layer thicknesses on cell performance. Typical case of absorbance spectrum of WSP and fullerene (C_{60}) has been considered for the simulation. For an optimal width of donor (50nm) and acceptor (50nm) we have shown in next section, we obtain the exciton flux at the D-A interface to be 10^{15}/cm^2 which corresponds to a maximum photocurrent to be $q\times10^{15}$/cm^2 = 1.288 mA/cm^2.

3.3.1 Effect of Mobilities, Layer Thicknesses & Interface Widths

With the help of simulation results, the effect of mobilities and layer thicknesses on open circuit voltage, fill factor, short circuit current and power conversion efficiency will be discussed below. For fixed donor and acceptor thicknesses, first, *J-V* characteristics, power conversion efficiencies (PCE), space charge formations, electric fields and band energies for various mobilities ($\mu_h = \mu_e$) will be examined. Then surface plots of electrical output parameters for the case of variation in donor and acceptor thicknesses and mobility will be discussed. After determining the optimal donor and acceptor thicknesses, surface plots of electrical output parameters for various combinations of donor and acceptor mobilities will be investigated. The effect of increasing mobilities or imbalance in mobilities will also be examined. Interface width w_{int} has the direct effect on charge carrier recombination and hence the power conversion efficiency which is also studied in this section.

3.3.1.1 Electrical parameters for various mobilities ($\mu_h = \mu_e = \mu$)

Initially we simulated the device for equal hole and electron mobilities varying from 10^{-7} to 10^{-2} cm^2/V-s, i.e. $\mu_h = \mu_e = \mu$ = [10^{-7}, 10^{-6}, 10^{-5}, 10^{-4}, 10^{-3}, 10^{-2}] cm^2/V-s (Figure 25 to Figure 29). The donor and the acceptor thicknesses are [50nm, 50nm]. Other simulation parameters are given in Table 2. As we increase the mobility from 10^{-7} to 10^{-2} cm^2/V-s the open circuit voltage (V_{OC} = [0.80, 0.763, 0.715, 0.664, 0.606, 0.547] V) decreases considerably, Figure 25. The short circuit current remains almost same for mobility values between 10^{-5} and 10^{-2} cm^2/V-s, but starts decreasing below 10^{-5} cm^2/V-s. For very low mobilities (<10^{-5} cm^2/V-s), space charge formation is so high that recombination at the D-A interface results in reduction in short circuit current.

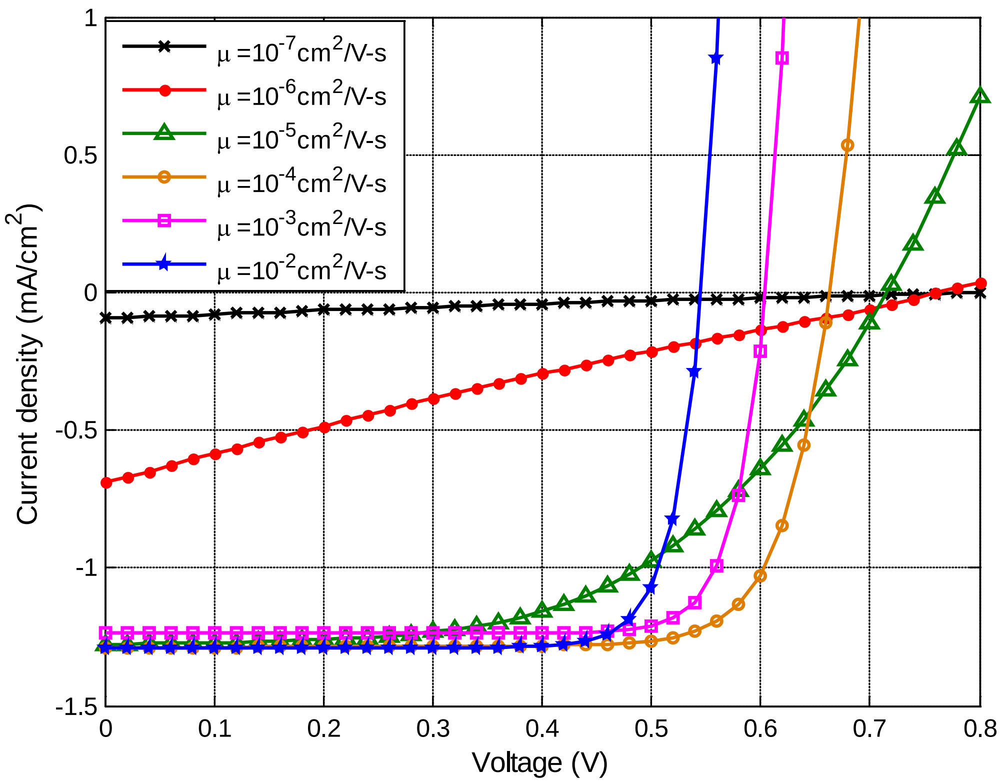

Figure 25: J-V characteristics of simulated bilayer OPV cell. Thickness $d_1 = d_2$ = 50nm; $\mu_h = \mu_e = \mu$. With increase in mobility, open circuit voltage decreases. Short circuit current does not change

much for mobility range of 10^{-5} - 10^{-2} cm^2/V-s but decreases with decrease in mobility below 10^{-5} cm^2/V-s.

For optimal donor and acceptor layer thicknesses, [donor: 50nm, acceptor: 50nm], PCE is plotted for mobility range of 10^{-7} - 10^{-2} cm^2/V-s (Figure 26). PCE increases with increase in mobility until it reaches to maximum (0.67%) at mobility = 10^{-4} cm^2/V-s and then decreases afterwards. The detailed performance study is done in the following sections.

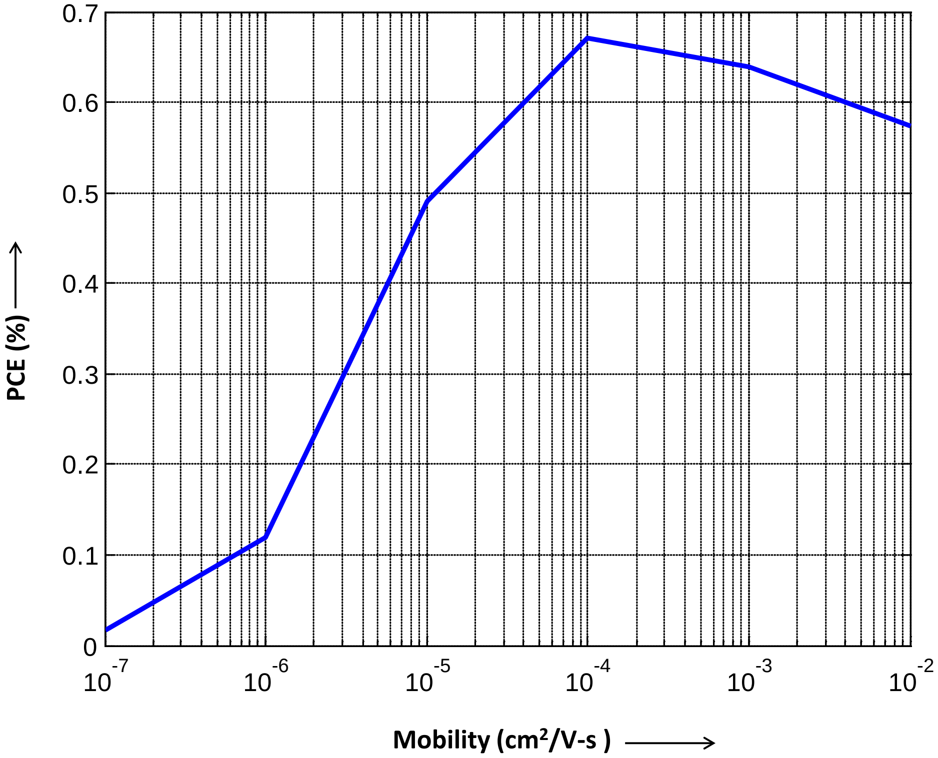

Figure 26: OPV power conversion efficiency at various mobilities ($\mu_h = \mu_e = 10^{-7}$ to 10^{-2} cm^2/V-s) for donor and acceptor thicknesses of 50nm each. PCE increases with mobility increase until it reaches to maximum at mobility = 10^{-4} cm^2/V-s. PCE starts decreasing thereafter.

For the open circuit condition, the simulated values for the charge carrier concentration in donor and acceptor regions with respect to distance are plotted in Figure 27. Thickness of both donor and acceptor are 50 nm and the D-A interface location is at 0. Other simulation parameters are given in Table 2. By increasing the mobility ($\mu_h = \mu_e = \mu$) of holes and electrons the concentration of holes in the donor and electrons in the acceptor decreases. This reduction in charge concentration at the D-A interface compared to anode and cathode interface (x = –50nm and 50nm, respectively) results in band lowering at D-A interface shown in Figure 29. This band bending increases the difference of donor LUMO at anode and acceptor LUMO at cathode.

Therefore, the split between donor HOMO at anode and acceptor LUMO at cathode decreases resulting in reduction in the open circuit voltage, Figure 29. Current in open circuit condition is zero and hence the direction of the electric field is opposite to diffusion current. We find that diffusion current at the D-A interface is from right to left (from acceptor to donor) for low mobilities (10^{-6} to 10^{-4} cm^2/V-s) and left to right (from donor to acceptor) for high mobility 10^{-2} cm^2/V-s, Figure 27. Therefore, the electric field at the D-A interface will be negative (donor to acceptor) for low mobilities (10^{-6} to 10^{-4} cm^2/V-s) and positive for high mobility (10^{-2} cm^2/V-s), shown in Figure 28. This increase in electric field with increase in mobility bends the band downward at D-A interface, Figure 29.

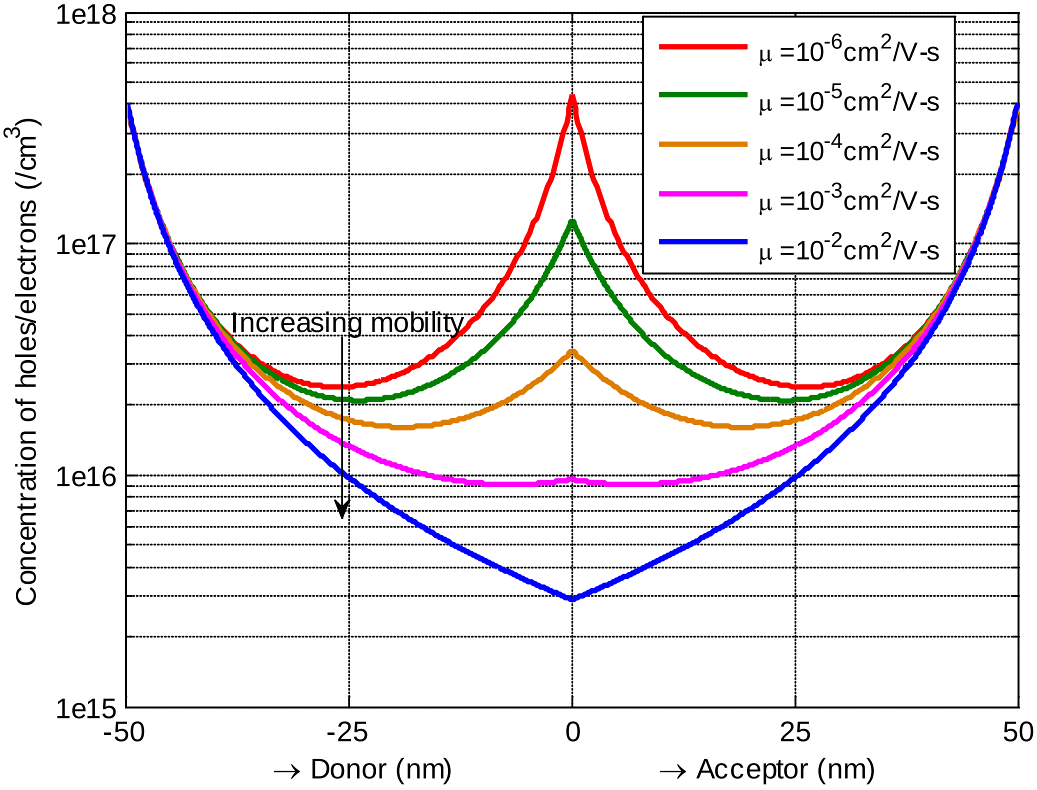

Figure 27: Concentration (/cm^3) of holes in the donor and electrons in the acceptor for various mobilities ($\mu_h = \mu_e = \mu$). The thickness of the donor and the acceptor both are 50nm and D-A interface is at distance 0. The charge accumulation at the D-A interface decreases with increasing mobility.

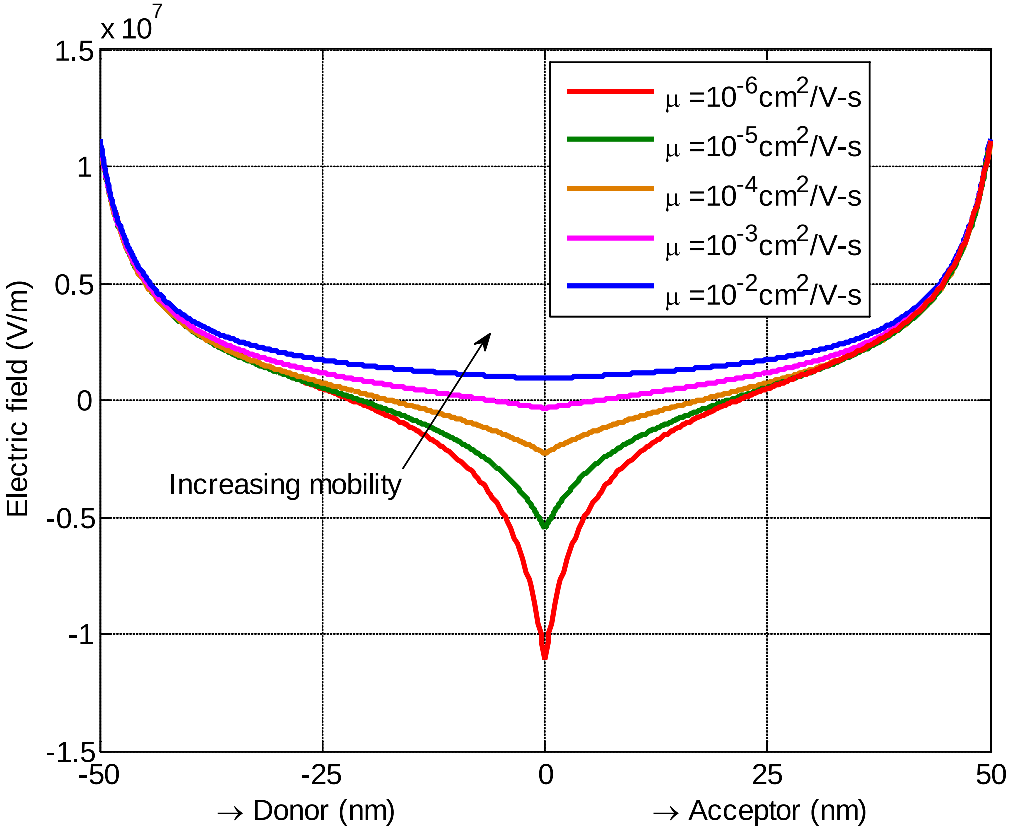

Figure 28: Electric field in the donor and the acceptor for various mobilities ($\mu_h = \mu_e = \mu$) in open circuit condition. The thickness of the donor and the acceptor both are 50nm and D-A interface is at distance 0. Electric field at D-A interface increases with increasing mobility.

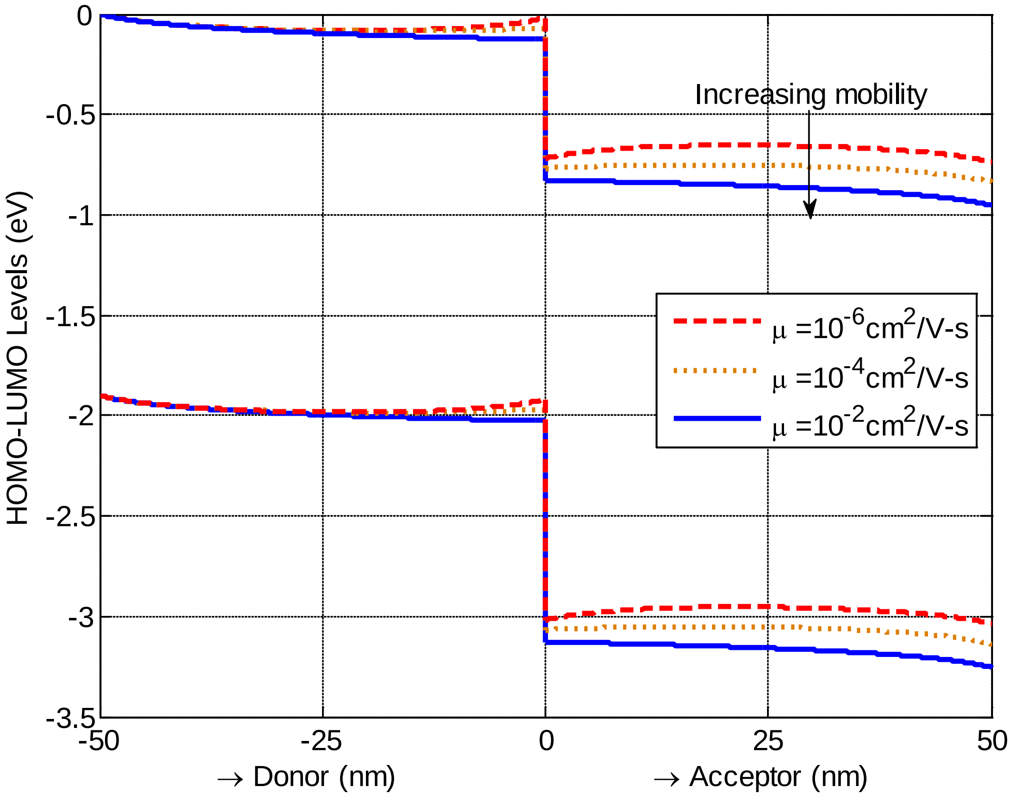

Figure 29: Relative levels of HOMO-LUMO energy of donor and acceptor in open circuit condition for three mobilities (μ_h=μ_e=μ) 10^{-6} cm^2/V-s, 10^{-4} cm^2/V-s and 10^{-2} cm^2/V-s. Donor LUMO level is set at 0 eV for the convenience. The thickness of the donor and the acceptor both are 50nm and D-A interface is at distance 0. As mobility increases, the difference between the donor LUMO and the acceptor LUMO increases and thus, the split between the donor HOMO and the acceptor LUMO decreases.

For clarity in Figure 29, we consider only three mobilities ($\mu_h = \mu_e = \mu$), 10^{-6}, 10^{-4} and 10^{-2} cm^2/V-s. Other conditions are same as mentioned before. The donor LUMO is set at zero level for analytical convenience and the relative energy levels of the other HOMO-LUMO levels are plotted. As the mobility increases, the difference between the donor LUMO at the anode and the acceptor LUMO at the cathode increases. Therefore, the split between the donor HOMO and the acceptor LUMO decreases which indicates a reduction in open circuit voltage.

3.3.1.2 Variation in donor thickness and mobility ($\mu_h = \mu_e = \mu$)

In this section, we study the effect of donor of various donor thicknesses and mobilities (($\mu_h = \mu_e = \mu$) on electrical output parameters. We keep the acceptor thickness at 50nm. Surface plots of all four parameters open circuit voltage, short circuit current, fill factor and power conversion efficiency are shown in Figure 30 to Figure 33 . These plots are helpful in determining the optimal donor thickness and mobility.

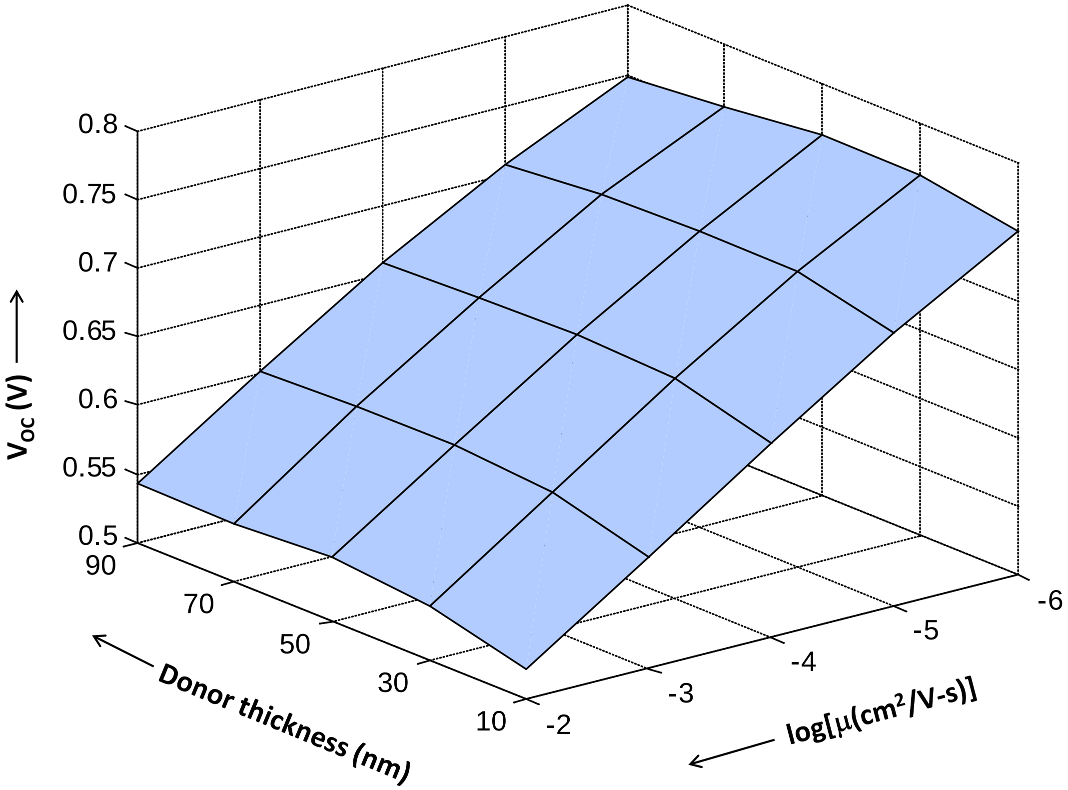

Figure 30: Open circuit voltage of OPV device with donor thicknesses [10, 30, 50, 70, 90] nm and mobilities μ_h=μ_e = [10^{-6}, 10^{-5}, 10^{-4}, 10^{-3}, 10^{-2}] cm^2/V-s. V_{OC} decreases with increase in mobilities but does not change much with change in donor thickness.

It has been explained earlier that open circuit voltage decreases with increase in mobilities of hole and electron as the potential split between donor HOMO to acceptor LUMO decreases with increasing mobilities. Decrease in V_{OC} with increasing mobility has been shown in Figure 30.

At very low mobility, μ = 10^{-6} cm^2/V-s, recombination is quite significant due to high concentration of charge carriers at the D-A interface and hence the short circuit (SC) current is low, as shown in Figure 31. When the electron and hole mobilities both increase, the carrier concentration of electrons and holes at the D-A interface decreases. Since, Langevin recombination is proportional to the product of carrier concentrations ($n_h \times n_e$) and the sum of the electron and hole mobilities ($\mu_h + \mu_e$), carrier concentrations play a large role in determining the recombination parameter. Therefore, an increase in mobility sharply increases the SC current and soon saturates as the electric field that increases with mobility extracts the almost all generated carriers quiet efficiently. Increasing the donor thickness absorbs more of incident photons to generate more excitons and hence photocurrent. But a thicker than a certain value will not improve the exciton flux at D-A interface as many excitons will not reach to the interface due to its very short diffusion length. Also, the thicker donor will reduce the electric field at the interface and charge carrier extraction suffers.

The fill factor surface plot is shown in Figure 32. For relatively high mobilities ($\geq 10^{-4}$ cm^2/V-s) it remains almost the same for all the donor thicknesses. However, for lower mobilities, the fill factor decreases with increase in donor thickness.

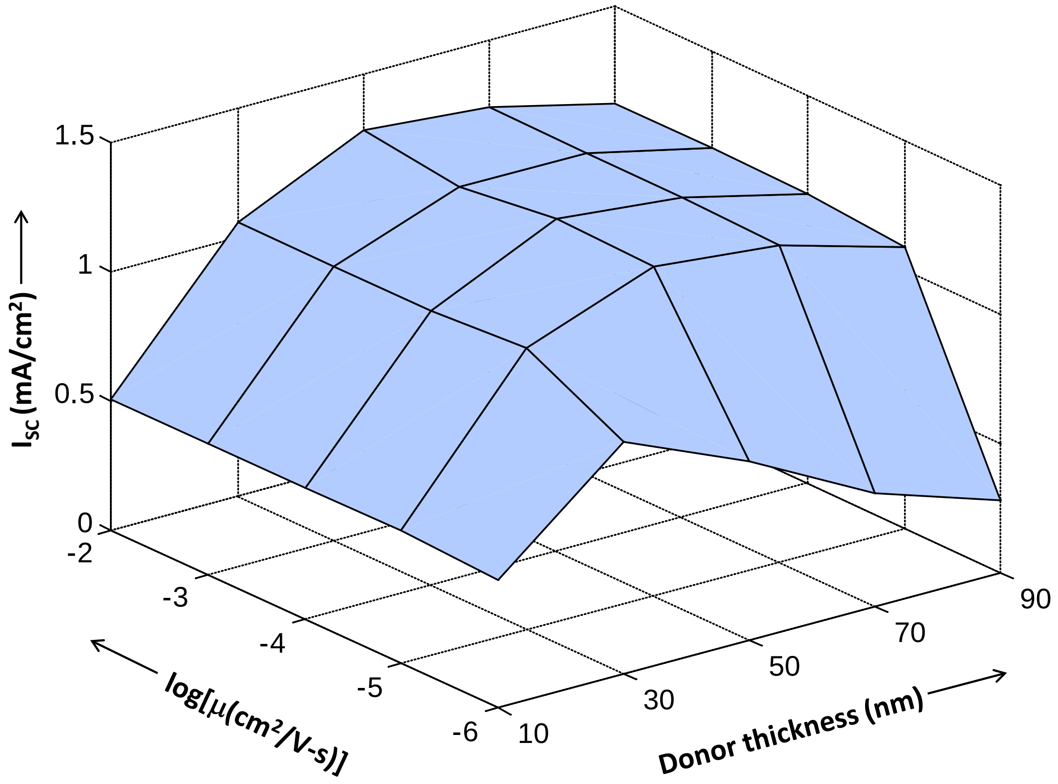

Figure 31: Short circuit current of OPV device with donor thicknesses [10, 30, 50, 70, 90] nm, acceptor thickness 50nm and mobilities $\mu_h = \mu_e = [10^{-6}, 10^{-5}, 10^{-4}, 10^{-3}, 10^{-2}]$ cm²/V-s. I_{SC} sharply increases for mobility greater than 10^{-6} cm²/V-s and then saturates. I_{SC} also increases with increase in donor thickness and reaches maximum for 50nm and then a gradual decrease follows.

Combined effect of all three characteristics V_{OC}, I_{SC}, and FF, power conversion efficiency is calculated and a surface plot is shown in Figure 33. It is found that for donor widths, PCE increases with increase in mobility ($\mu_h = \mu_e$) starting at 10^{-6} cm²/V-s. PCE has a maximum value of 0.67% for 50 nm thick donor with mobility of 10^{-4} cm²/V-s. Further increase in mobility causes a slight decrease in PCE mainly due to monotonic decrease in open circuit voltage as other parameters I_{SC} and FF have almost flat profiles for the mobilities in that range.

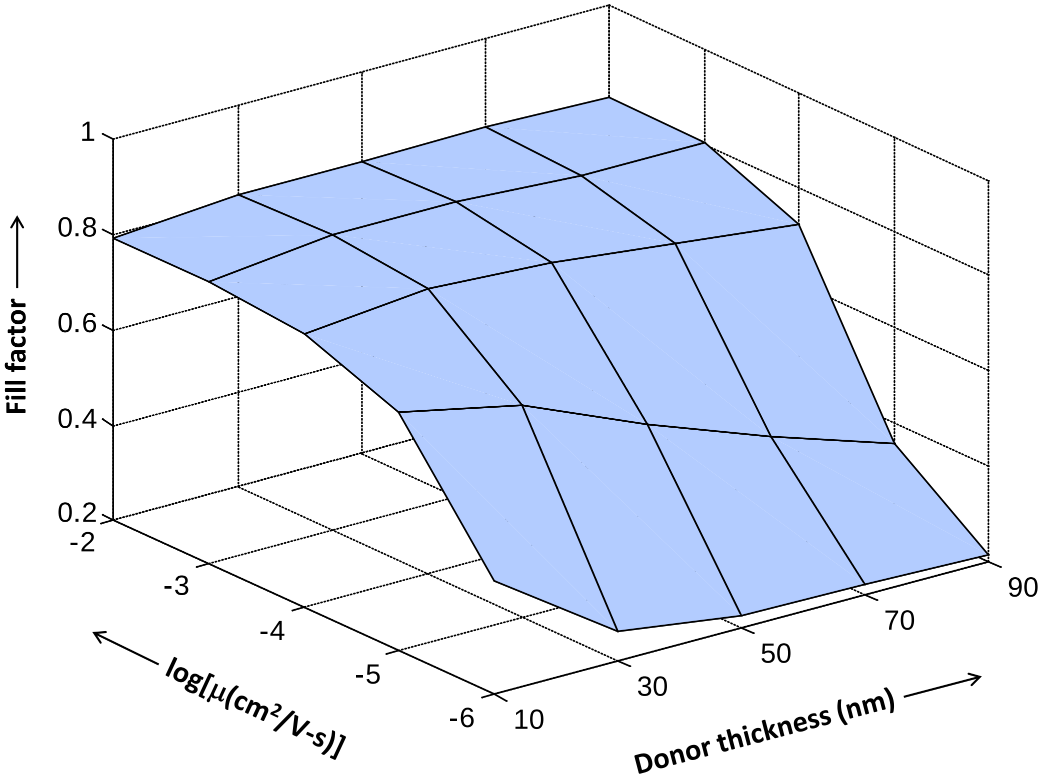

Figure 32: Fill factor of OPV device with donor thicknesses [10, 30, 50, 70, 90] nm, acceptor thickness 50nm, and mobilities $\mu_h = \mu_e = [10^{-6}, 10^{-5}, 10^{-4}, 10^{-3}, 10^{-2}]$ cm^2/V-s. FF is almost constant for higher mobilities ($\geq 10^{-4}$ cm^2/V-s) for all thickness. FF for low mobilities decreases with increase in donor thickness.

PCE for the highest mobilities case ($\mu_e = \mu_h = 10^{-2}$ cm^2/V-s) was found to be 0.57% which is about 15% less than the optimum PCE (0.67%). While designing an OPV cell with a given material, there is almost no choice to change its mobility, hence parameters of active layers thickness (donor and acceptor) that can easily be changed during fabrication, an optimal thickness is determined by the surface plot. For mobilities between 10^{-4} cm^2/V-s and 10^{-2} cm^2/V-s, it is found that 50nm thick donor delivers maximum PCE whereas for mobility of 10^{-5} and 10^{-6} cm^2/V-s, PCE is maximum for 30nm thick donor (Figure 33).

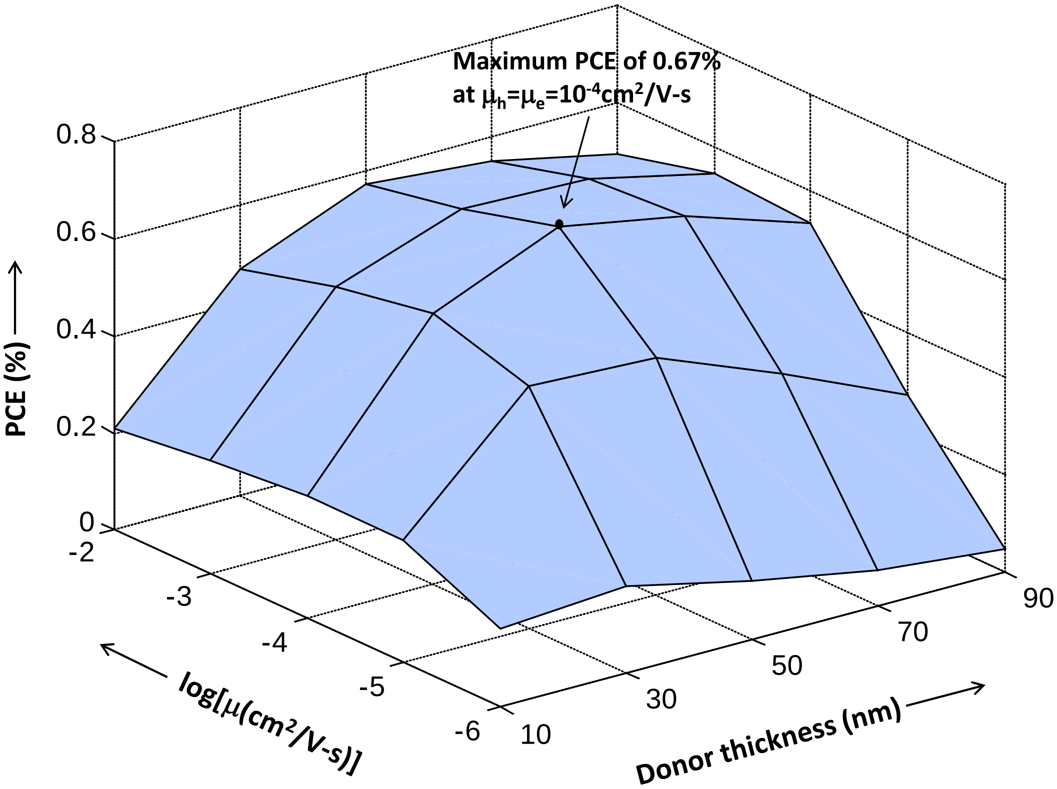

Figure 33: Power conversion efficiency of OPV device with donor thicknesses [10, 30, 50, 70, 90] nm, acceptor thickness 50nm and mobilities $\mu_h = \mu_e$ = [10^{-6}, 10^{-5}, 10^{-4}, 10^{-3}, 10^{-2}] cm^2/V-s. PCE is found to be maximum of 0.67% at 50nm thick donor with electron and hole mobility of 10^{-4} cm^2/V-s.

Below is the surface plot of PCE of OPV for three different acceptor thicknesses [10, 30, 50] nm, donor thicknesses [10, 30, 50, 70, 90] nm, and mobilities $\mu_h = \mu_e = \mu$ = [10^{-6}, 10^{-5}, 10^{-4}, 10^{-3}, 10^{-2}] cm^2/V-s (Figure 34). It is found that for lower mobility range μ = [10^{-6} - 10^{-5}] cm^2/V-s, maximum PCE is found to be 0.59% at [donor: 30nm, acceptor: 10 nm] (dashed line surface). For higher mobilities μ = [10^{-4} - 10^{-2}] cm^2/V-s, maximum PCE is found to be 0.67% for 50nm thick donor and 50nm thick acceptor (solid line surface).

For a thinner active layer, the electric field is higher and the charge carrier concentration is lower at the D-A interface and hence reduced recombination near the maximum power point, results in a higher fill factor. This effect of increase in fill factor for thinner active layers compared with thicker ones is more pronounced for very low mobilities (10^{-6}, $10^{-5}$$cm^2/V$-s). Therefore, the PCE is improved for thinner active layers (donor: 30nm, acceptor: 10nm) in case of lower mobilities (10^{-6}, $10^{-5}$$cm^2/V$-s). However, reducing the donor thickness to 10nm, the PCE is decreased, as thinner donor (≤ 10nm) is not able to absorb enough photons. For higher mobilities (≥$10^{-4}$$cm^2/V$-

s), the fill factor is high (~0.7-0.8) and more improvement in it is not possible by making the active layer thinner and hence PCE is not improved further.

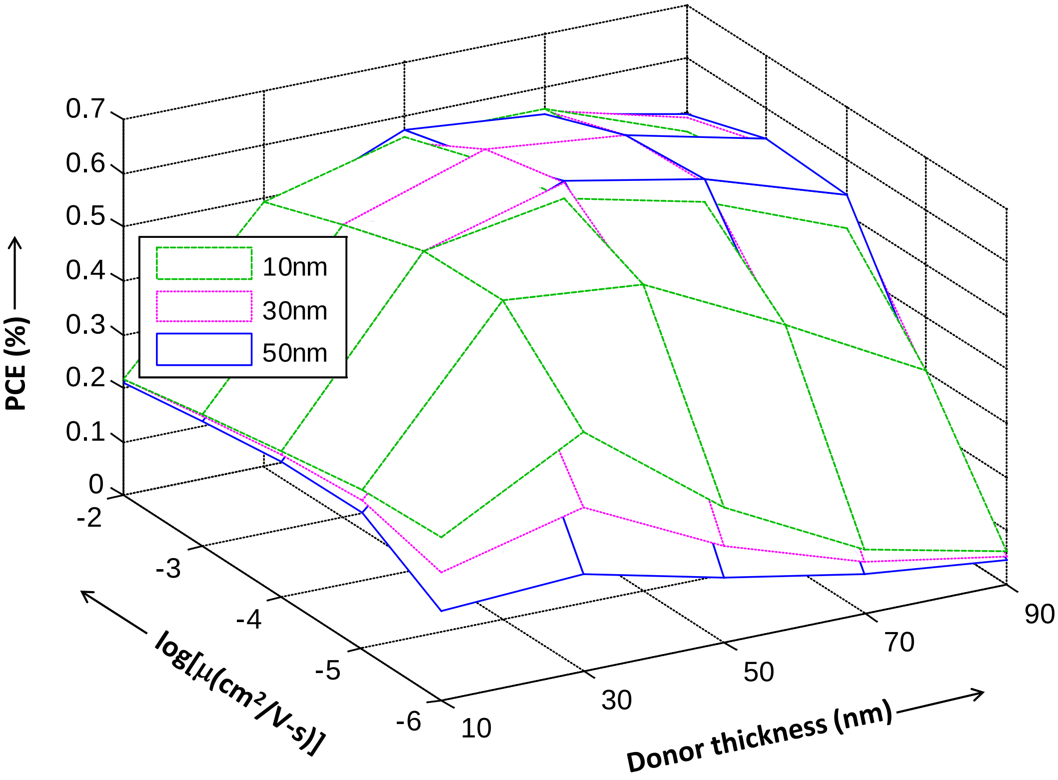

Figure 34: Power conversion efficiency of OPV for acceptor thicknesses [10, 30, 50] nm, donor thicknesses [10, 30, 50, 70, 90] nm, and mobilities $\mu_h = \mu_e = \mu$ = [10^{-6}, 10^{-5}, 10^{-4}, 10^{-3}, 10^{-2}] cm^2/V-s. For mobility range μ = [10^{-6}-10^{-5}] cm^2/V-s, maximum PCE is found to be 0.59 % when the donor thickness is 30nm and the acceptor thickness is 10nm (dashed line surface). For higher mobility range μ = [10^{-4}- 10^{-2}] cm^2/V-s, maximum PCE is found to be 0.67 % for 50nm thick donor and 50nm thick acceptor (solid line surface).

3.3.1.3 Variation in hole and electron mobility

In the previous section we found from the surface plot that the optimal thickness of the donor is 50 nm and mobility is $10^{-4}$$cm^2$/V-s. In this section we will study the cell performance for various electron and hole mobilities which are independently varied. Simulations were performed for various combinations of hole mobility in donor and electron mobility in the acceptor, keeping both the donor and acceptor thicknesses at 50nm. Three-dimensional surface plots are shown in

Figure 35 to Figure 38. The mobility of holes and electrons are varied from 10^{-7} cm^2/V-s to 10^{-2} cm^2/V-s, i.e. μ_h = [10^{-7}, 10^{-6}, 10^{-5}, 10^{-4}, 10^{-3}, 10^{-2}] cm^2/V-s and μ_e = [10^{-7}, 10^{-6}, 10^{-5}, 10^{-4}, 10^{-3}, 10^{-2}] cm^2/V-s and for each combination of [μ_h, μ_e] the device is simulated.

The decrease in V_{OC} with increasing mobility ($\mu_h = \mu_e$) has been explained in the previous section. Here we will study the change in V_{OC} when hole and electron mobilities are varied independently, Figure 35. At balanced mobility conditions, when either hole or electron mobility decreases, V_{OC} remains almost unchanged; and by increasing mobility of one of the charge carriers, V_{OC} decreases fast, Figure 35.

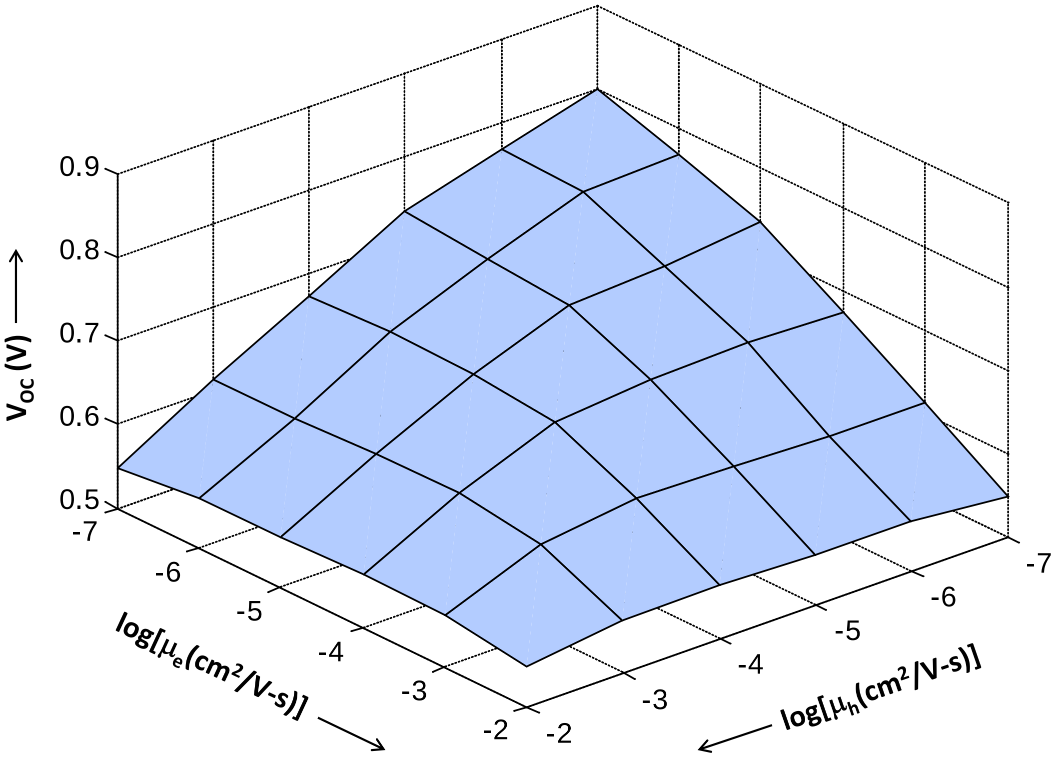

Figure 35: Open circuit voltage (V_{OC}) of OPV device for electrons and holes mobilities both varying from [10^{-7} to 10^{-2}] cm^2/V-s. V_{OC} increases as mobilities decrease. For high mobility (10^{-2}cm^2/V-s) of either of electrons or holes, open circuit voltage is about 0.55 V and does not change much.

That implies that V_{OC} is mainly determined by the higher among hole and electron mobility value. In case of open circuit condition and balance mobility ($\mu_h = \mu_e$), the electric field at D-A interface is very low or even negative for low mobilities and a large pile up of space charge forms at D-A interface. At slight increase in mobility of either hole or electron, carrier concentration at D-A interface reduces rapidly and more flatter profile of band is found. This reduces the open circuit voltage. Similarly, charge carrier concentration at D-A interface and hence energy bands and hence V_{OC} does not change rapidly if mobility of one of the charge carriers is decreased from balanced mobility condition. A monotonic decrease of V_{OC} is found as the mobilities ($\mu_h = \mu_e$) increase.

A surface plot (Figure 36) of the fill factor for the previous conditions show a minimum fill factor of 0.18 for the lowest mobility (10^{-7} cm^2/V-s) and 0.8 for the highest mobility (10^{-2}cm^2/V-s).

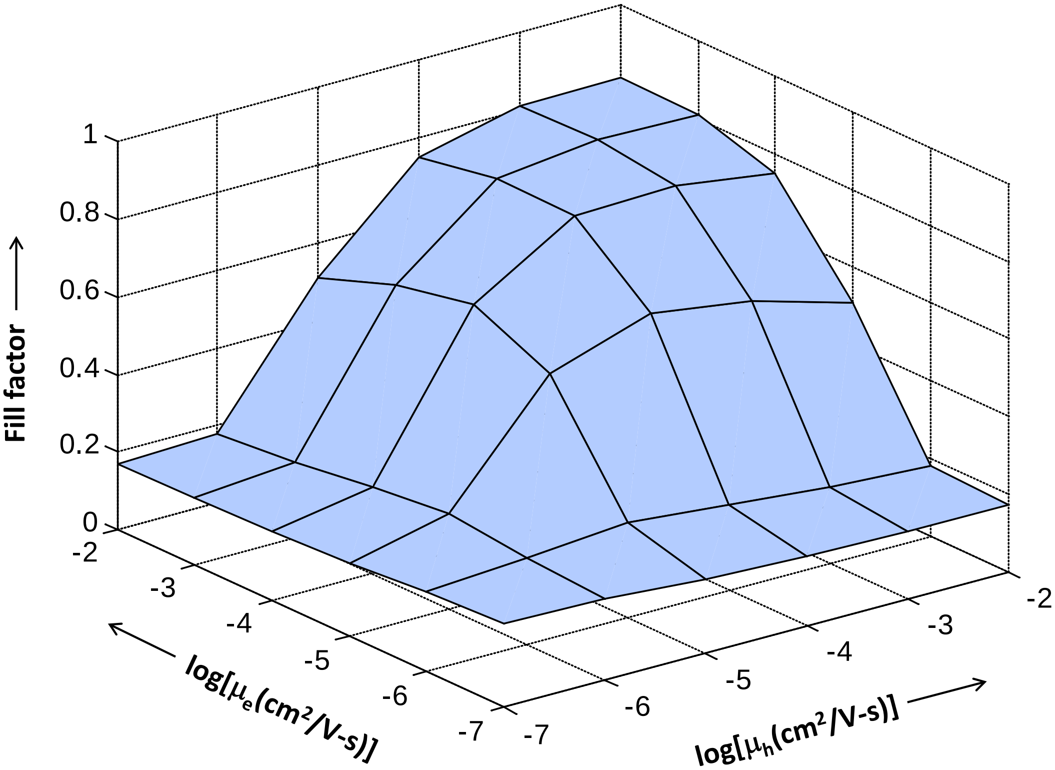

Figure 36: Fill factor of OPV cell for electrons and holes mobilities both varying from [10^{-7} to 10^{-2}] cm^2/V-s. FF is higher for higher mobilities and decreases sharpely for mobilities below 10^{-4}cm^2/V-s.

Figure 37 shows a surface plot for the short circuit current density (I_{SC}) of OPV cell for electrons and holes mobilities both varying from [10^{-7} to 10^{-2}] cm^2/V-s. It is assumed that all the excitons are dissociated at the D-A interface and current density J_{ex} before recombination at the D-A interface is fixed for a given light input. The photocurrent density is $J_{ph} = J_{ex} - J_{rec}$.

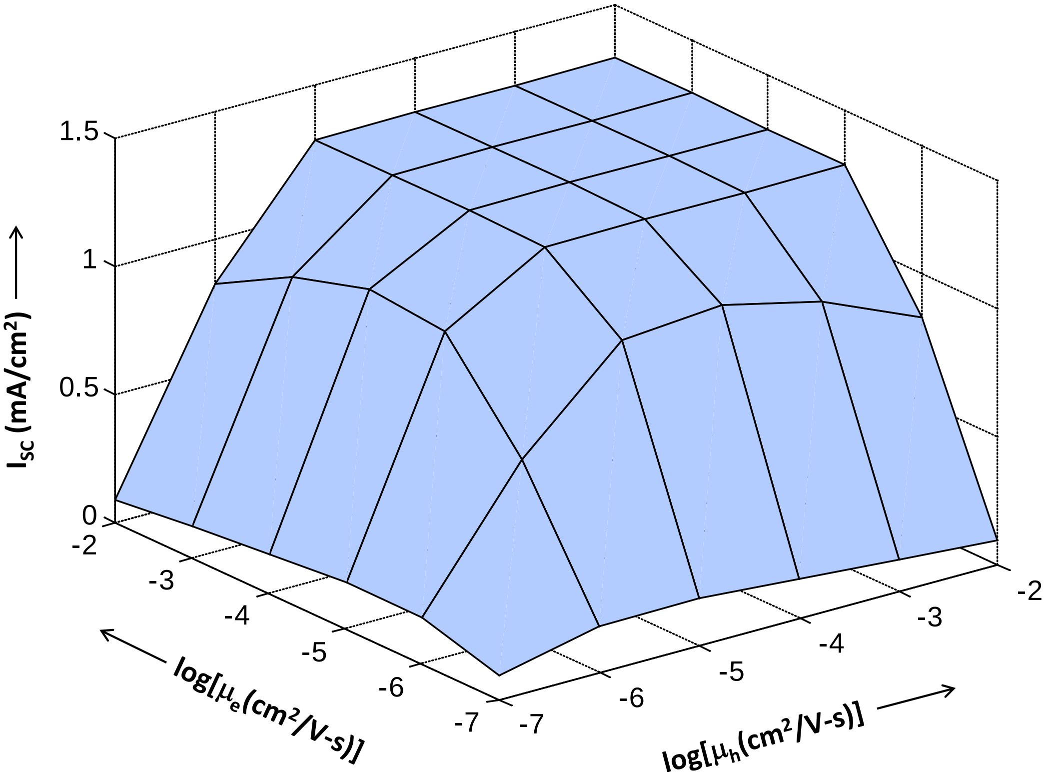

Figure 37: Short circuit current density (I_{SC}) of OPV cell for electrons and holes mobilities both varying from [10^{-7} to 10^{-2}] cm^2/V-s. I_{SC} does not change much for mobilities of electrons and holes between 10^{-5} and 10^{-2} cm^2/V-s but sharp decrement is found below the value of 10^{-5} cm^2/V-s.

For higher mobilities ($\geq 10^{-5}$cm^2/V-s), electric field is high in short circuit condition and space charge density at the D-A interface is very low. Therefore, recombination is negligible in these cases and short circuit current profile for mobilities ($\geq 10^{-5}$cm^2/V-s) is flat in the surface plot. However, I_{SC} start decreasing sharpely for hole or electron mobility below 10^{-5}cm^2/V-s as recmobination current density increases due to large space charge formation near the D-A interface. Keeping the electron mobility of the acceptor constant (10^{-7}cm^2/V-s), if we increase the hole mobility in the donor, space charge formation in the donor depletes and reduces the hole concentration at the D-A interface. This leads to reduced recombination at the interface and hence increased short circuit current. Further increases in hole mobility saturate I_{SC} as even in the presence of a small electric field, most holes are efficiently extracted from the donor material and not much improvement could be done. In fact for low electron mobilities (μ_e = 10^{-7} and 10^{-6}cm^2/V-s), I_{SC} starts decreasing if the hole mobility is increased above μ_h = 10^{-4}cm^2/V-s. In this case of mobility ratio (μ_h /μ_e $\geq$ 100), for such a low electron mobility a dense space charge is always present in the acceptor and carrier recombination is dominated by increasing hole mobility in the donor than depletion of hole carrier concentration. The similar explanation can be given for fixing hole mobility and varying electron mobility as the 3-D surface plot is symmetrical along both mobilities.

Percentage power conversion efficiency (PCE) of OPV device for electrons and holes mobilities both varying from [10^{-7} to 10^{-2}] cm^2/V-s is shown in Figure 38. Maximum PCE of 0.67% is found at electrons and holes mobilities, $\mu_h = \mu_e = 10^{-4} cm^2/V$-s and almost saturates beyond that point or a slight decrease in efficiency was found. Further increases in mobilities, the conversion efficiency slightly decreases. Overall minimum PCE was found to be 0.009% for $\mu_h = 10^{-7}$ cm^2/V-s, $\mu_e = 10^{-2} cm^2/V$-s.

We have seen that for low mobilities ($<10^{-5}$ cm^2/V-s), V_{OC} decreases slowly (Figure 35) compared to sharp rise in I_{SC} (Figure 37) when mobility of either or both charge carriers (hole and electron) is increased. For higher mobilities ($\geq 10^{-5}$ cm^2/V-s), I_{SC} remains almost unchanged and fill factor (Figure 36) increases slowly but V_{OC} which decreases monotonically with increasing mobilities mainly dominates the profile of PCE. Therefore, overall PCE decreases after an optimum point of mobility $10^{-4} cm^2/V$-s.

Mobility is termed as balanced when $\mu_h = \mu_e$. In PCE surface plot Figure 38, we have observed that beyond the dotted boundary increase in mobility ratio ($\mu_h / \mu_e > 10$ or, $\mu_h / \mu_e < 1/10$) causes a drop in PCE. For example, PCE [μ_e: μ_h $=10^{-5}$:10^{-5} cm^2/V-s] = 0.49%, PCE [μ_e: μ_h $=10^{-5}$:10^{-4} cm^2/V-s] = 0.54% and PCE [μ_e: μ_h $=10^{-5}$:10^{-2} cm^2/V-s] = 0.37%. In this case, percentage decrease in PCE for mobility ratio of 1000 compared to balance mobilities is = (0.49-0.37)/0.49 = 25%. For the simultaneous increase in balanced mobility, PCE increases for low mobilities ($\mu = 10^{-7}$-10^{-4} cm^2/V-s) but decreases for higher mobilities ($\mu = 10^{-4}$-10^{-2} cm^2/V-s, and that has already been shown in Section 3.3.1, Figure 26. To study the effect of mobility imbalance or various mobility ratios, we show a bar plot for PCE percent change when mobility of one of the charge carriers (either holes or electrons) is increased (Figure 39).

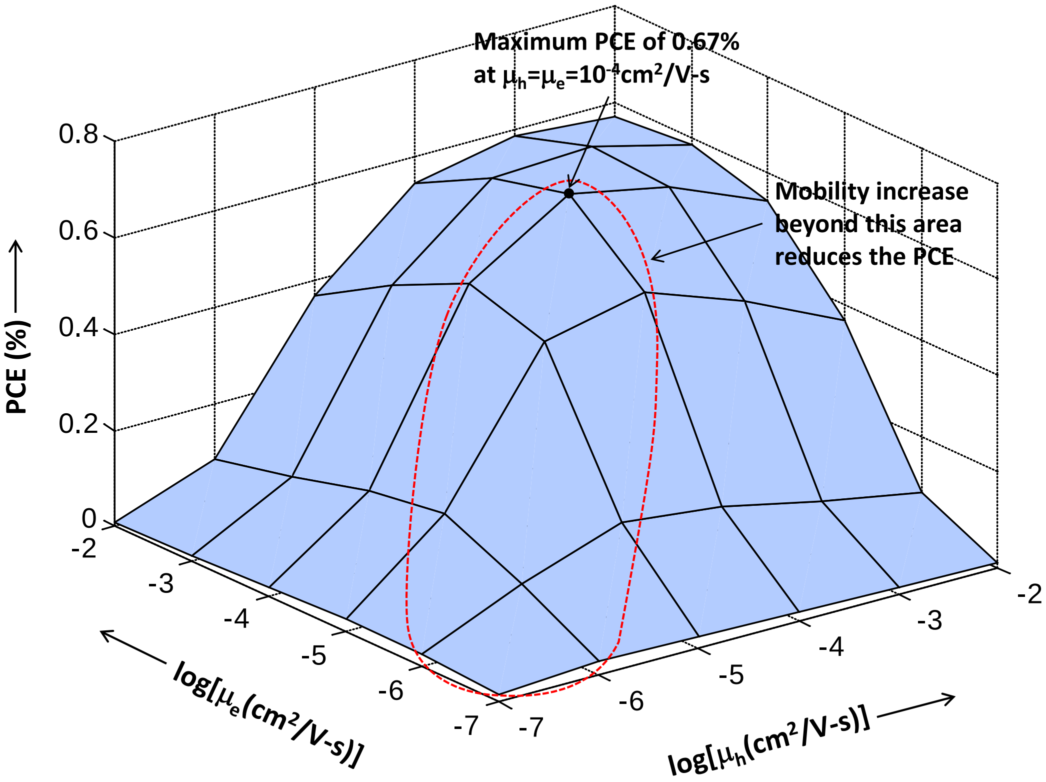

Figure 38: Percentage power conversion efficiency (PCE) of OPV device for electrons and holes mobilities both varying from [10^{-7} to 10^{-2}] cm^2/V-s. Maximum PCE of 0.67% is found at electrons and holes mobilities, $\mu_h = \mu_e = 10^{-4}$cm^2/V-s. Further increases in mobilities, the conversion efficiency slightly decreases.

It was found that increase in mobility ratio has adverse impact on PCE for higher mobility cases ($\geq 10^{-4}$ cm^2/V-s) and percentage PCE decrement increases with increase in mobility ratio. But for lower mobilities ($<10^{-5}$ cm^2/V-s), smaller mobility ratios (up to 100) in fact enhances the PCE and only larger imbalance ($\geq 10^4$) causes a reduction in PCE when it is compared with the PCE in balanced mobility case. For lower mobilities ($<10^{-5}$ cm^2/V-s), even small increase in mobility or mobility ratio there is a sharp rise in short circuit current, leads to increased PCE but for larger mobility ratios ($\geq 10^4$), PCE decreases as short circuit current decreases due to increased recombination at D-A interface. For higher mobilities ($\geq 10^{-4}$ cm^2/V-s), monotonic decrease in open circuit voltage and very less change in short circuit current with increase in mobility ratios lead to PCE decrease.

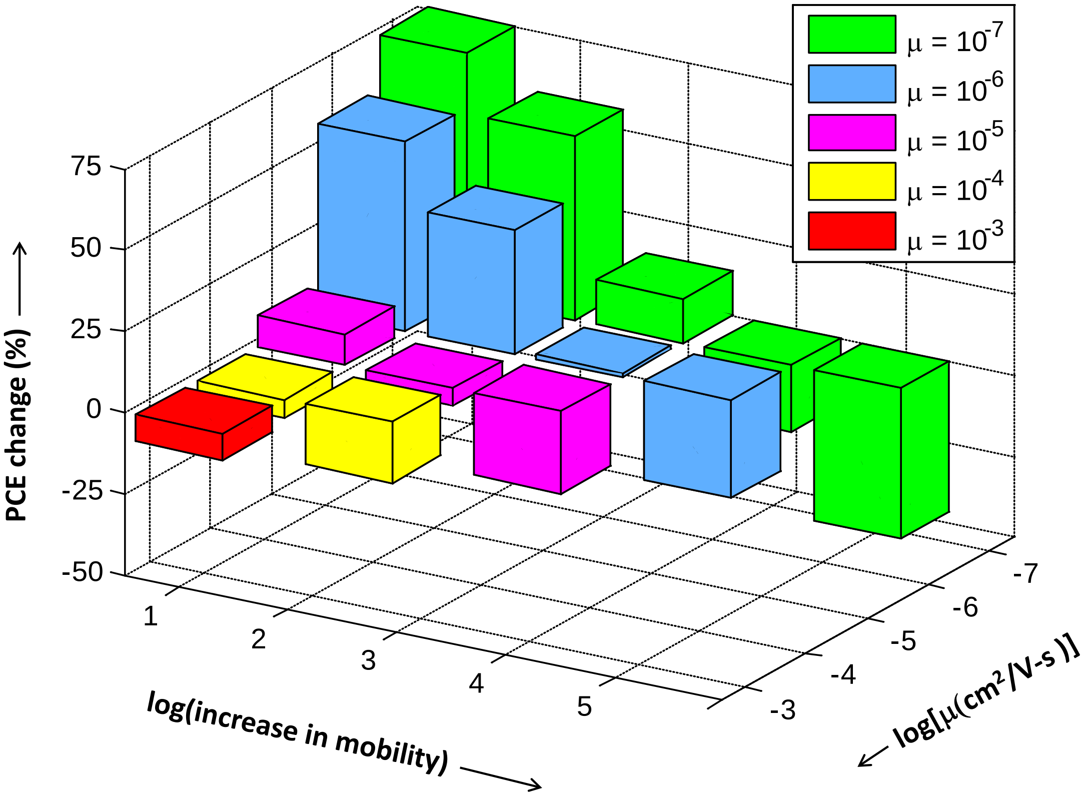

Figure 39: Bar plot of percentage change in PCE for various mobilities and mobility imbalance ratios. For higher mobilities (10^{-4}, 10^{-3}) cm^2/V-s, PCE drops at even lower mobility ratio (10). For lower mobilities (10^{-6}, 10^{-7}) cm^2/V-s, PCE drops at higher mobility ratios (>10^4).

3.3.1.4 Effect of interface widths (w_{int})

By increasing the depleted interface width w_{int}, recombination of charge carriers at the D-A interface increases. We, in our simulation, have examined the effect of various w_{int} [0.4 0.8 1.2 2.0] nm for two different mobilities (10^{-4}cm^2/V-s and 10^{-6}cm^2/V-s) to see how it affects the PCE for lower and higher charge carrier mobilities (Figure 40 and Figure 41). We have kept hole and electron mobility equal, ($\mu_e = \mu_h$). For the higher mobility case (10^{-4}cm^2/V-s), charge carrier extraction is efficient and hence D-A interface recombination under short circuit conditions is quite small with an increase in w_{int}. For higher applied voltage (near V_{OC}), the charge recombination at D-A interface is pronounced due to very low electric field and hence recombination current that increases with increase in w_{int}, leads to lowering the open circuit voltage (as early crossing of zero axis) (Figure 40).

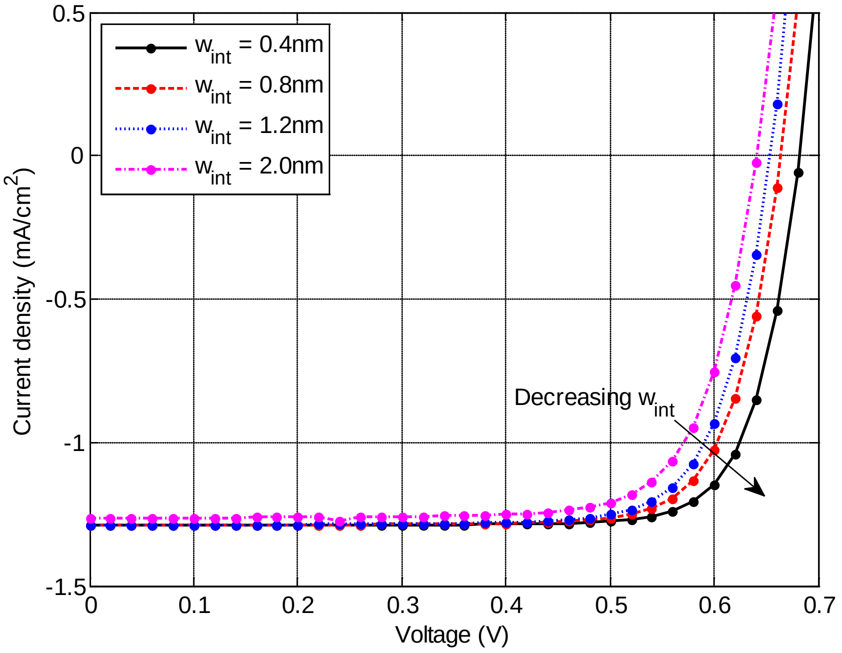

Figure 40: J-V characteristics of OPV cell for four different interface widths *w_{int}* = [0.4 0.8 1.2 2.0] nm and $\mu = \mu_e = \mu_h = 10^{-4}$cm^2/V-s. Short circuit current does not change much for change in interface width. Open circuit voltage reduces with increase in *w_{int}*.

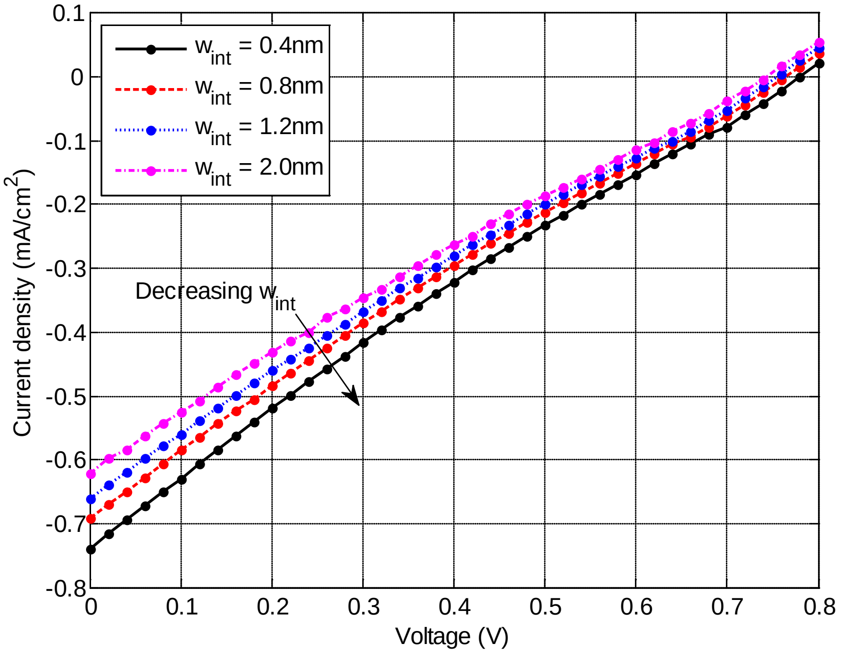

Figure 41: J-V characteristics of OPV cell for four different interface widths *w_{int}* = [0.4 0.8 1.2 2.0] nm and $\mu = \mu_e = \mu_h = 10^{-6}$cm^2/V-s. Short circuit decreases with increase in interface widths. A slight open circuit voltage drop is also found with increase in *w_{int}*.

For the lower mobility case (<10^{-6}cm^2/V-s), charge carrier extraction is poor due to large space charge formation near the D-A interface and the short circuit current is lower due to increased recombination at the D-A interface. For larger interface widths w_{int}, the recombination current is more and hence short circuit current density is lower (Figure 41).

Power conversion efficiency is plotted for various interface widths and two mobility values (10^{-4}cm^2/V-s and 10^{-6}cm^2/V-s), shown in Figure 42. The PCE drops with increases in w_{int} for both mobilities. In the case of higher mobility (10^{-4}cm^2/V-s), PCE decreases by only 12% when the interface width is increased 5 times from 0.4nm to 2nm. For the lower mobility case (10^{-6} cm^2/V-s), the PCE decreases by 17.4%, for the same increase in interface width. The PCE is more sensitive to interface width change for lower mobilities.

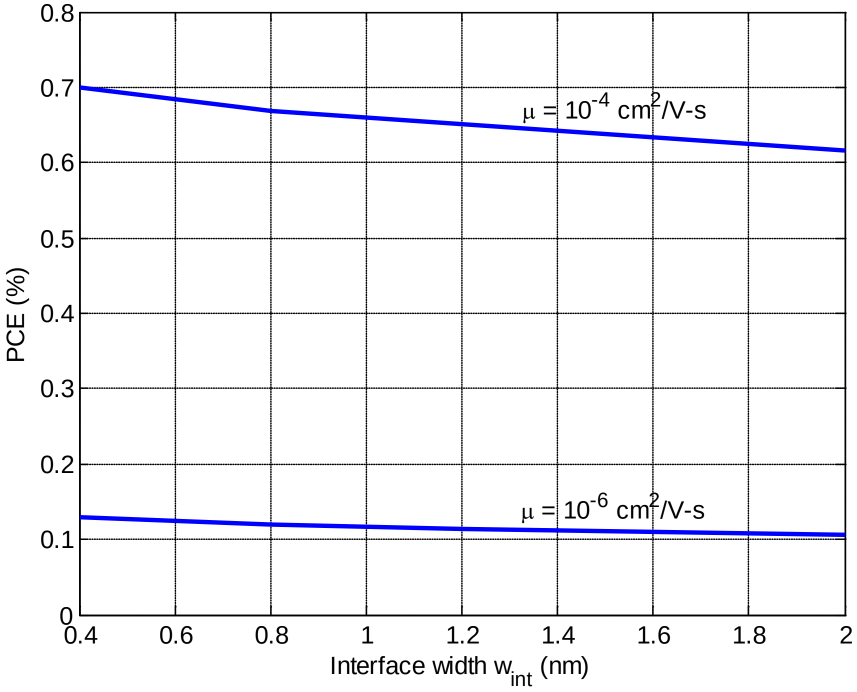

Figure 42: Percentage PCE of OPV cell for four different interface widths w_{int} = [0.4 0.8 1.2 2.0] nm and $\mu = \mu_e = \mu_h$ = [10-6 and 10^{-4}]cm^2/V-s. PCE decreases with increase in interface widths for both mobilities.

3.3.1.5 Effect of exciton diffusion length in the donor (L_{dd})

The exciton diffusion length is a key parameter in OPV devices and directly affects the exciton flux density at the D-A interface. A small diffusion length limits the active layer thickness of the device and therefore reduces the possible light absorption, impacting the PCE. The contribution of the exciton flux from the acceptor layer (C_{60}) compared with the flux from the donor layer (or front layer) is very small (typically a 20:1 ratio) because of the small exciton diffusion length (5 nm) and the fact that only some of the light penetrates through to the acceptor layer. Hence in this section we examine the effect of various exciton diffusion lengths in the donor layer, L_{dd} = [10 20 30 50 80]nm, on the power conversion efficiency. When increasing the diffusion length L_{dd}, however, the donor thickness needs to be increased to achieve the maximum PCE (in order to absorb more light). Hence, for each L_{dd}, the donor thickness is optimized to obtain the maximum PCE. The results are plotted in Figure 43. The acceptor thicknesses were also readjusted while optimizing the PCE. This resulted in only small changes to the optimum acceptor thickness, from about 50 nm to 40 nm as the donor thickness increased. The acceptor exciton diffusion length was kept constant at 5nm as its contribution to the exciton flux at the D-A interface is small. Donor and acceptor mobilities of 10^{-4}cm^2/V-s ($\mu = \mu_e = \mu_h$)were used for this simulation.

We find that the PCE increases when the diffusion length of exitons in the donor is increased and also that the optimized donor thickness d_1 increases accordingly. The PCE saturates for exciton diffusion lengths more than 50nm as shown in Figure 44. Also shown in Figure 44 is that the optimized donor thickness varies almost linearly with L_{dd}.

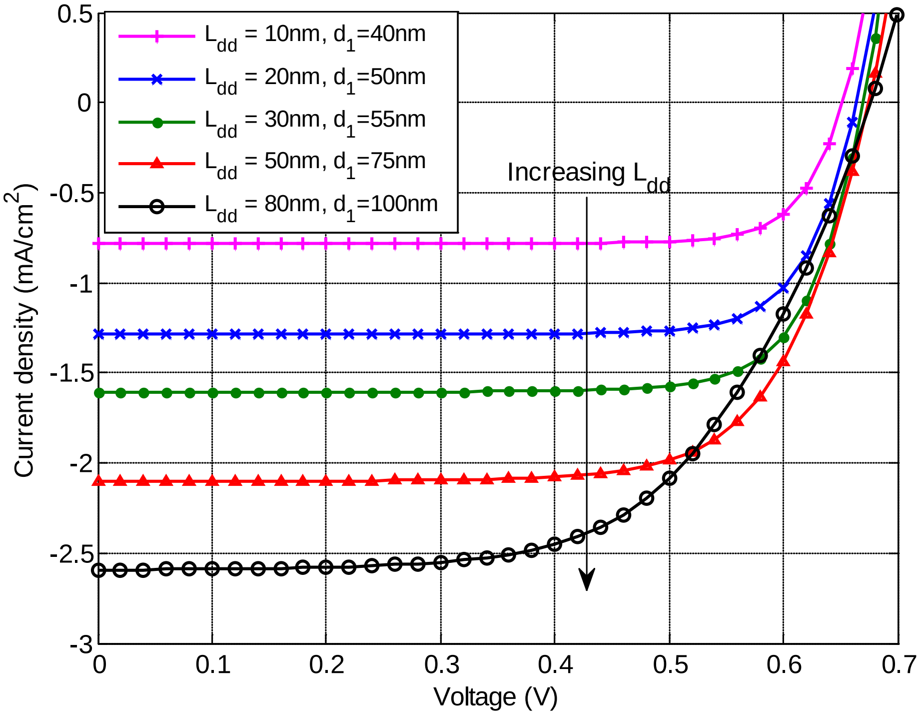

Figure 43: J-V characteristics of OPV cell for five different exciton diffusion lengths in the donor, L_{dd} = [10 20 30 50 80] nm and $\mu = \mu_e = \mu_h = 10^{-4}$ cm2/V-s. OPV cell performance is much better for higher exiton diffusion lengths.

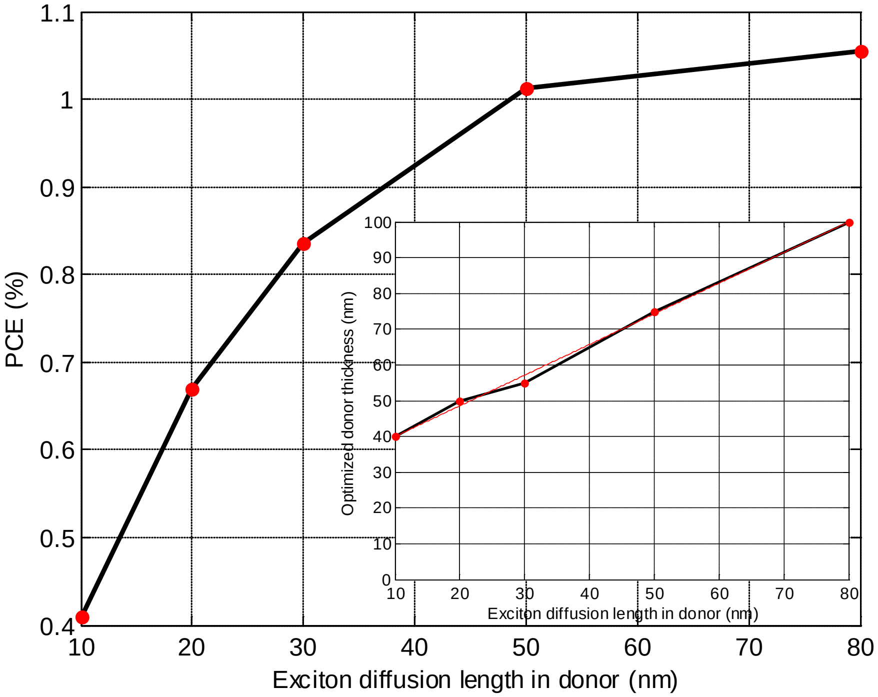

Figure 44: Percentage PCE of OPV cell for five different exciton diffusion lengths in the donor, L_{dd} = [10 20 30 50 80] nm and mobility $\mu = \mu_e = \mu_h = 10^{-4}$ cm^2/V-s. PCE increases with L_{dd} but saturates beyond 50nm. *Inset:* Optimized donor thickness varies almost linearly with L_{dd}.

4. OPV Based on Water Soluble Pentacene

In this chapter, we will briefly discuss the first pentacene derivative that is soluble in water and was synthesized by Prof. Glen Miller's group at University of New Hamphshire, Durham. This water soluble pentacene (WSP) shows field-effect transistor and photovoltaic behavior. The fabrication procedure and its challenges for making the OPV cell based on WSP will be discussed in detail. The cell performance or electrical characterization will also be discussed.

4.1 Introduction

Pentacene is a polycyclic aromatic hydrocarbon consisting five linearly connected benzene rings. This is a p-type organic semiconductor which generates excitons upon absorption of UV or visible light.

π-conjugated molecules of pentacene have high HOMO levels and can easily donate electrons. Such organic materials are good candidates for p-type semiconductors. Pentacene is one of the most investigated conjugated organic molecules due to its potential application in organic electronics with its high hole mobility in organic field-effect transistors (OFETs) of up to 5.5 $cm^2/(V.s)$ [125, 126]. Its poor solubility limits the processability of devices. Due to fast photo-degradation in the presence of air, pentance needs extra care while processing. Design and synthesis of functionalized [127-132] pentacenes with enhanced solubility and solution stability potentially allow for low cost fabrication of thin film devices [133-137] by solution process methods such as spin coating, spray coating, ink-jet printing and doctor blading etc.

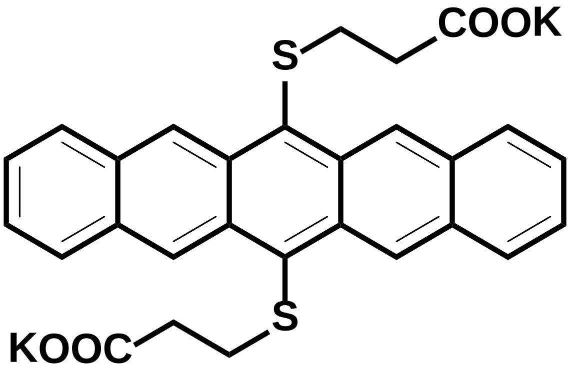

Figure 45: Chemical structure of water soluble pentacene or Potassium 3,3’-[(pentacene-6,13-diyl)bis(sulfanediyl)]dipropanoate [138]

WSP is a derivative of a pentacene containing COOK$^-$ (potassium salt of carboxylic) groups as shown in Figure 43, and its chemical name is Potassium 3,3’-[(pentacene-6,13-diyl)bis(sulfanediyl)]dipropanoate. The synthesis steps for WSP are briefly summarized in Figure 44 along with the optical image of its water solution in a flask [138]. Its high HOMO level of -5.16 eV makes it a good donor material (p-type) and the HOMO-LUMO gap is about 1.95 eV. The half-life of WSP in an aqueous buffer solution with exposure to light and air is approximately four days (96 hours) making it one of the most solution-stable pentacene derivatives known [127]. UV-Vis absorption spectra of WSP in water, methanol and a buffer solution of pH 10 are shown in Figure 45. It shows a good absorption between green and red light.

In a bulk heterojunction OPV, a solution of donor and acceptor materials are used for coating of active layer via such as spin method where a common organic solvent like chlorobenzene (CB), dichlorobenzene (DCB) toluene etc. is used. These organic solvents are toxic and environmental unfriendly. A solution of WSP in water or a much less harmful solvent like ethanol can be used for spin coating the donor active layer and the acceptor of C_{60} can be thermally evaporated. In a bilayer solar cell, orthogonal solvents for the donor and the acceptor are needed in order not to dissolve or damage the first active layer while the second active layer is spin coated using another solvent. Since WSP is not soluble in organic solvents such as CB or DCB, it is safe for spin coating a solution of fullerene in CB or DCB on the donor layer of WSP.

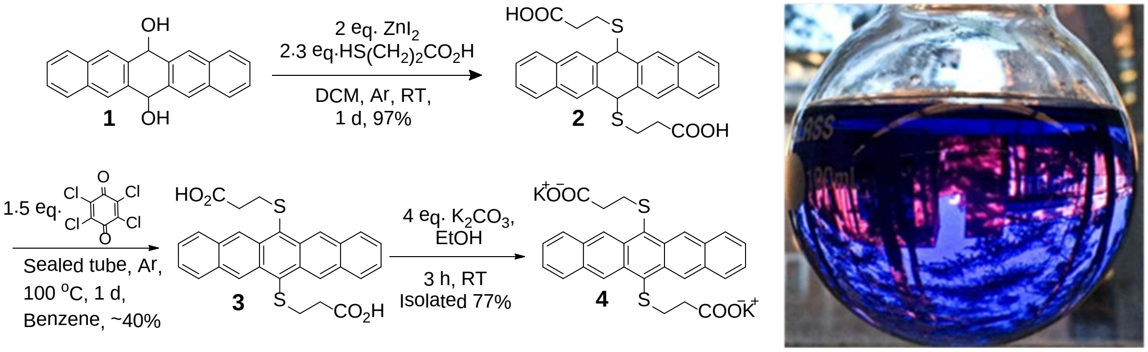

Figure 46: *Left*: Synthesis of the first water soluble pentacene; *Right*: WSP dissolved in water

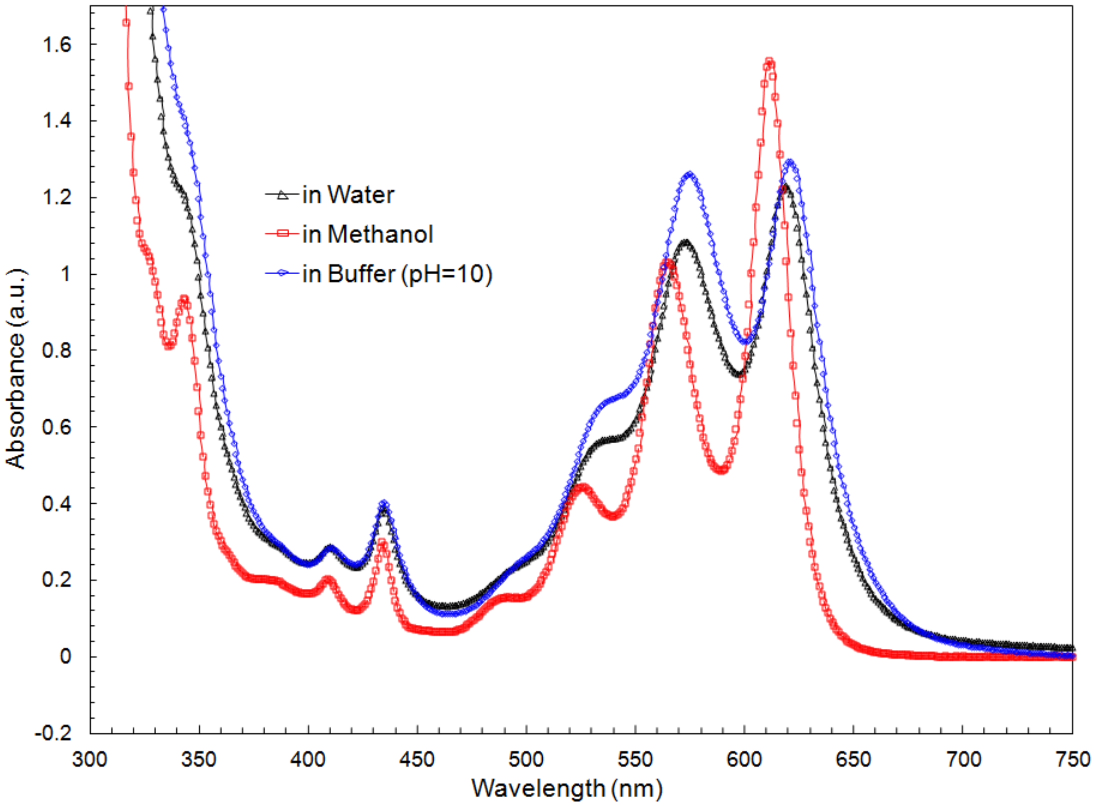

Figure 47: UV-Vis absorbance spectra for WSP in water, methanol and a buffer solution of pH 10[138]

4.2 Substrate Coating with WSP

WSP is very soluble in polar solvents such as dimethyl sulphoxide (DMSO), ethanol, methanol and water. For the fabrication of bilayer OPV cell, it's important to make thin and continuous films of donor and acceptor active materials for the efficient exciton generation and charge transport. However, spin coating of solutions of WSP in solvents mentioned above resulted in with crystal formation on the substrate. We are discussing the substrate coating with WSP in above solutions and a method to achieve the WSP film is described.

(a) WSP in DMSO

DMSO is a colorless, polar solvent that dissolves both polar and nonpolar compounds and miscible in a wide range of organic solvents as well as water. The methyl groups of DMSO are somewhat acidic and hence supposedly do not harm the slightly acidic PEDOT: PSS film on ITO. A solution of crystalline WSP (10mg) in DMSO (1ml) was prepared and filtered with 0.45µ filter. The solution was spin coated on a PEDOT: PSS film and baked on a hot plate at 120℃ for 2min. Micron-size crystals of WSP were formed over the surface and convex rings were observed where most of the crystals were located. Optical images are shown at 100X and 1000X magnification in Figure 46. The Dektak Profilometer measurement shows WSP crystals as thick as 200 nm were formed on 70-80 nm thin films of PEDOT: PSS, as shown in Figure 47.

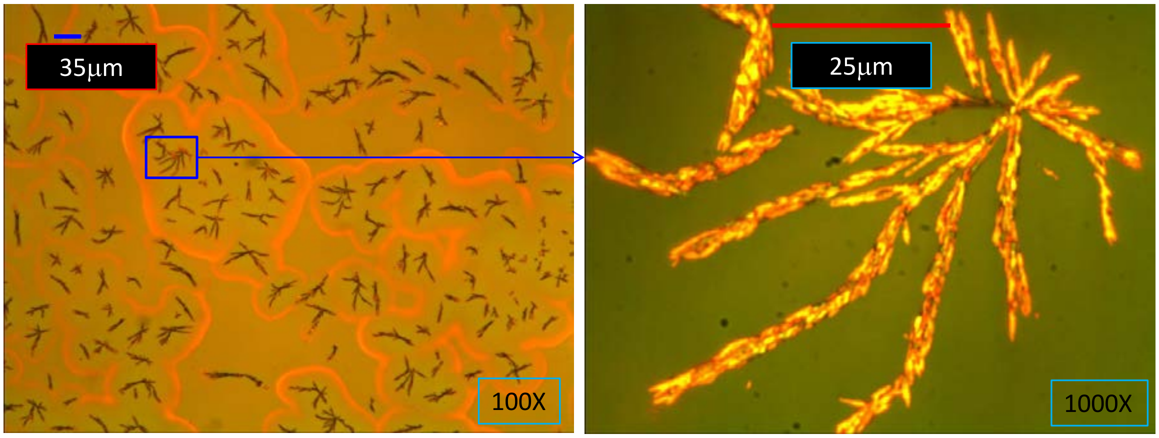

Figure 48: Crystalline WSP solution in DMSO spin coated on PEDOT: PSS film. Micron size crystals were found all over the surface of PEDOT: PSS film.

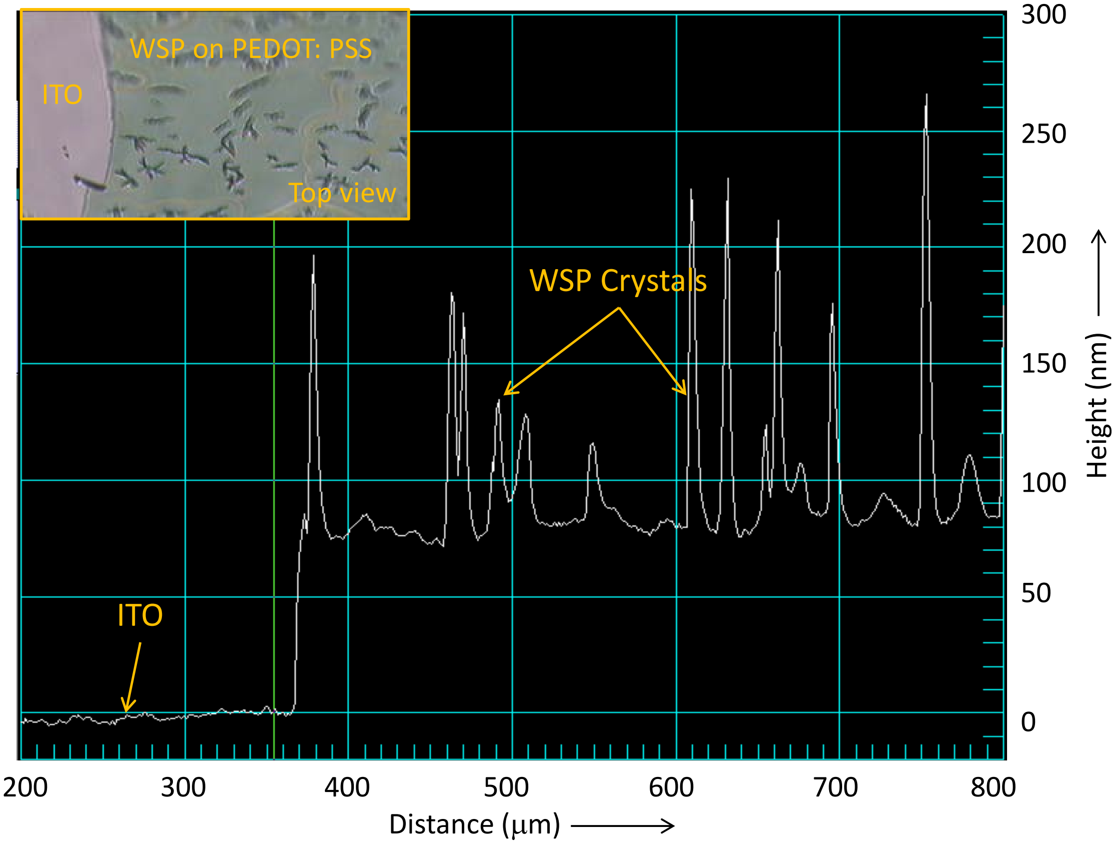

Figure 49: ***Dektak profilometry*: WSP crystals of as tall as 200nm were observed on a 70-80 nm thick PEDOT: PSS film; *inset*: Optical image of ITO surface and WSP on PEDOT: PSS film**

(b) WSP in DI water

Solutions of WSP (10mg) in DI water (1ml) were filtered (0.45µ pore size) and spin coated on PEDOT: PSS films on ITO substrates and also directly on ITO coated glass. The optical image in Figure 48(a) shows some randomly deposited pilled out films of existing PEDOT: PSS film. It is observed that PEDOT: PSS film is damaged when WSP solution, which is basic in DI water, is spin coated on it. WSP crystals were found all over the ITO surface, shown in Figure 48(b). These crystals were so loosely attached to ITO that they were displaced while making DekTak measurements. A preliminary device was made of WSP without any acceptor with structure ITO/PEDOT: PSS/WSP/Al. WSP was dissolved in DI water and spin-coated on PEDOT: PSS film. The detail of the fabrication is described in Section 4.3. The device was active and showed a short-circuit current of 1.7 μA/cm^2 and open circuit voltage of 0.3V. Several circular boundaries of WSP crystals of micron sizes were found, Figure 49.

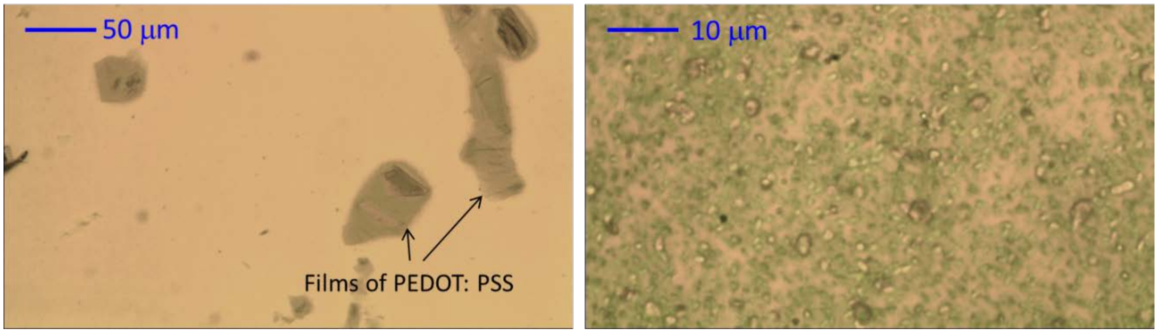

Figure 50: For DI water as solvent, *Left*: (a) WSP on PEDOT: PSS - broken or pilled out films of PEDOT: PSS were found re-deposited randomly on WSP film; *Right*: (b) WSP on ITO coated glass – crystals were found on the surface and were quite loosely attached to ITO that DekTak measurement was not possible.

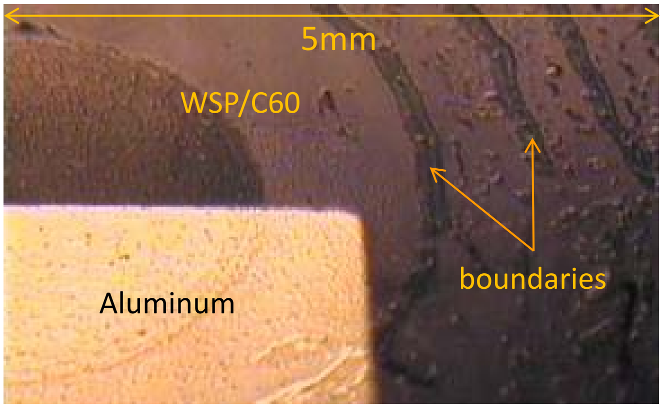

Figure 51: Optical image of the first fabricated OPV cell using WSP, showed a photovoltaic effect. (V_{OC}=0.3V, I_{SC}=1.7μA/cm^2). Many circular boundaries of WSP crystals of micron sizes were observed. WSP coating in a solid circular pattern of about 2-4 mm diameter at the center of the chip was also found.

(c) WSP in ethanol and methanol

A WSP solution in ethanol or methanol, unlike DI water, when spin coated on a PEDOT: PSS film does not seem to damage the film. However, the coating is quite non uniform and discontinuous. The optical images demonstrate the micron size crystal formations on the surface when a solution of WSP in ethanol Figure 50(a) or methanol Figure 50(b) is spin coated.

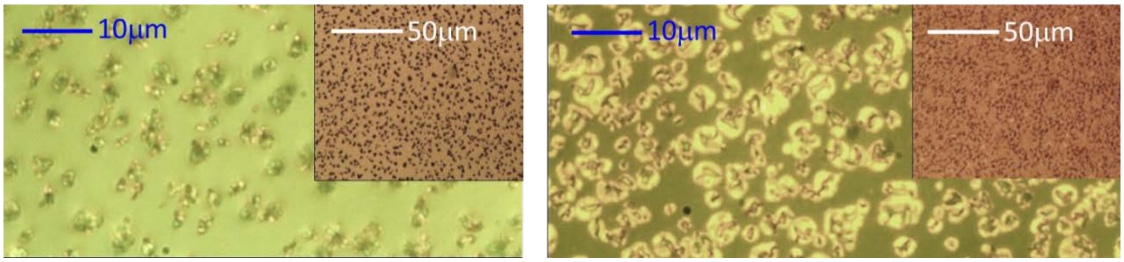

Figure 52: Optical images of WSP spin coated on PEDOT: PSS film when; *Left*: (a) WSP solution in ethanol; *Right*: (b) WSP solution in methanol. In both the cases micron size crystals were found on whole substrate.

(d) Spin coating of WSP in ethanol at raised temperature

WSP solution in ethanol did not damage the PEDOT: PSS film. The crystallite formation described above was almost completely overcome using infrared (IR) heating of the substrate and the solution during the coating process. 1 wt% of WSP (10mg) solution in ethanol (1ml) is filtered through 0.45μ pore size filter. The substrate and the solution are heated using IR lamp to 60-80℃ just prior to and during the spin coating process. The spin speed was set to 2000 rpm for 1 min and the film was baked at 80℃ for 2 min. This yielded a much more uniform film compared to previous WSP coating processes. Optical images of the film in the middle of the substrate and near the corner are shown in Figure 51.

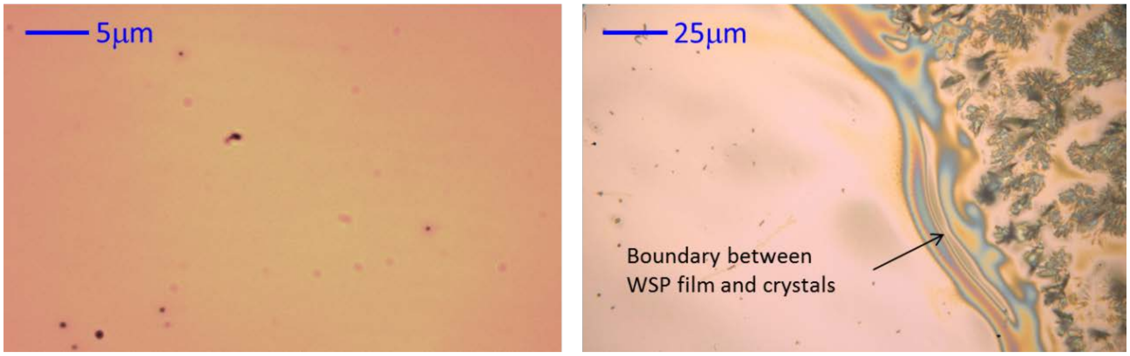

Figure 53: WSP solution in ethanol spin coated on a PEDOT: PSS film while substrate and solution were heated with IR lamp. *Left*: WSP film in the middle of the substrate and *Right*: Image near the corner showing WSP film and crystals separated by a boundary

4.3 Fabrication

Below is the schematic of the OPV cell made of active layers WSP/C_{60}, Figure 52(a). The device has a simple structure ITO/PEDOT: PSS (80nm)/WSP (55nm)/C_{60} (25nm)/Al (110nm). Dektak Profilometer measurements are shown for the active layers combined (PEDOT: PSS/WSP/C_{60}) and aluminum cathode, Figure 52(b). The main fabrication steps are shown pictorially in Figure 53. A run sheet for the fabrication is given in the Appendix.

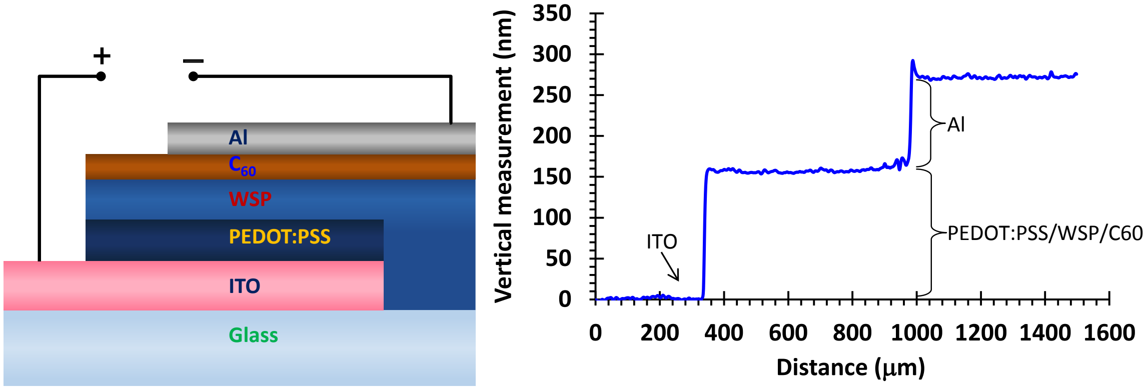

Figure 54: (a) Schematic of WSP based OPV cell with electron blocking layer (b) Dektak Profilometer reading of various layers

Materials used

ITO coated glass (1.1mm with 120nm thick ITO) – Delta Technologies.

PEDOT: PSS (high conductive grate) and ethanol (99.5%) – Sigma-Aldrich.

WSP (crystalline) – Prof. Glen's group at University of New Hamphshire, Durham.

C_{60} (fullerene 99.95%) – SES Research.

Al (99.99%) – Sigma-Aldrich.

(a) Dicing and first cleaning

An ITO coated glass sheet is diced into square chips (15mm X 15mm X 1.1mm) using the Micro Automation Dicing Saw (Model # 1006), where the ITO thickness was 120 nm. Chips were first cleaned using the acetone gun to remove oil and big particles. Ultrasonication of the chips for 10 min in soap, 3 min in acetone, and 1 min in IPA followed by a 3 min DI water overflow rinse was performed at each step and dried by N_2 blow.

(b) ITO etch

ITO coated glass was partially masked using Kapton Polyimide tape and 1813 PR was spin coated (4000 rpm, 1min) and baked at 115℃ for 1min. The tape was then removed and the exposed ITO was chemically etched in HCl (37%) for 6 min at room temperature and rinsed in DI water for 3 min.

(c) Substrate clean

The PR on the chips was removed using the acetone gun and then ultrasonicated for 10 min in acetone, and 3 min in IPA followed by a 3 min DI water dump rinse at each step. Finally the chips were dried using N_2.

(d) Substrate bake and plasma clean

Substrates were baked on hotplate for 1 hour at 150℃ to remove any absorbed moisture and organic contamination on the surface. Oxygen plasma cleaning for 1 min was then performed in ICP Plasma Therm 7900 to get rid of any residual organics on the ITO surface. A DC bias of about 30 V and a RF plasma power of 300W were maintained. A base pressure of 50 mTorr and an oxygen flow of 50 sccm (standard cubic centimeters per min) were maintained.

(e) Spin coat the electron blocking layer

High conductive grade PEDOT: PSS solution was first filtered through 0.45μm pores of PVDF filters. The filtered solution was then spin coated (4000 rpm, 1min) on the plasma cleaned substrates to make a thin film of electron blocking layer. Substrates are baked on a hot plate for 20 min at 120℃ and moved immediately into the nitrogen filled glove box (H_2O < 1ppm, O_2 < 1ppm).

(f) Spin coat the donor layer

1 wt% of WSP solution in ethanol (10mg/ml) was prepared and filtered through PVDF 0.45μm filters. An infrared (IR) lamp (250W) was used inside the glove box to heat both the substrate and the solution of WSP for spin coating using the method is described before to obtain uniform and smoother film of WSP.

(g) Evaporation of the acceptor material and cathode

At a base pressure of 5×10^{-7} torr in the Veeco Thermal Evaporator, a 25 nm film of C_{60} as an acceptor was evaporated at a rate of 1~2 Å/s. Using a shadow mask, 110 nm of aluminum as a cathode was evaporated at a rate of ~10 Å/s.

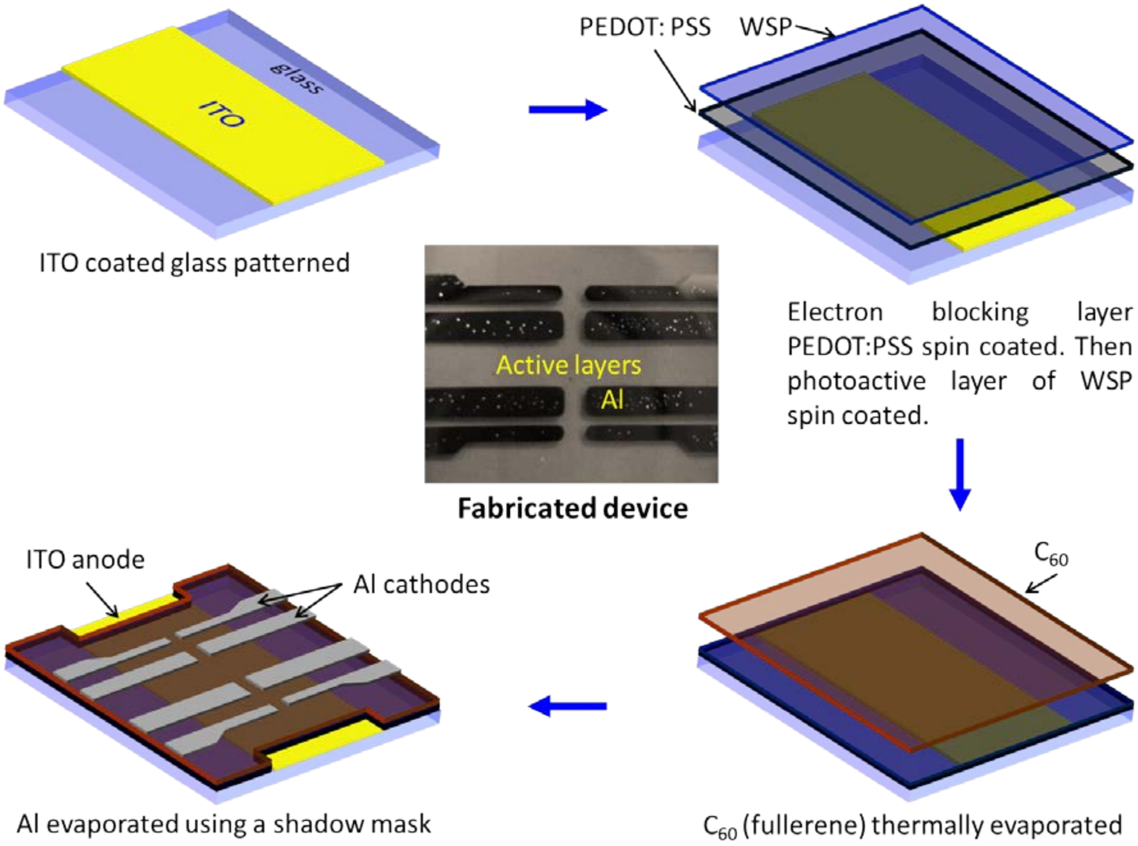

Figure 55: Fabrication steps for WSP based OPV. The actual fabricated device is in center

4.4 Measurement and Characterization

A Keithley 2410 source-meter and a 4155A HP Semiconductor analyzer were used for I-V measurements under the illumination of a calibrated halogen lamp (Dolan Jener Fiber-lite). The calibration was done by comparing the short-circuit current under sunlight of known intensity and also the halogen light source. The short-circuit current from the device under test was 0.382 times the short circuit current with the sunlight of 83.5mW/cm^2 intensity. The spectral irradiance of sunlight is significantly different than halogen light and therefore the photon absorption by the device in these two conditions will be different. However, calibration of halogen light equivalent to sunlight as power input can be calculated by 0.382×83.5 = 31.9mW/cm^2. The LabVIEW program was used for generating I-V characteristics of the OPV cell. Table 3 shows the performance of five samples of WSP based cells. Figure 54 corresponds to the J-V characteristics of the best performing cell.

Table 3: WSP based OPV cell performance for five samples. Tested under the halogen light calibrated to generate 0.382 times the short-circuit current with sunlight of 83.5mW/cm2 (AM2) intensity. Halogen light equivalent sunlight input = 0.382×83.5 = 31.9 mW/cm^2.

Sample	Pin (mW/cm^2)	Jsc (mA/cm^2)	Voc (V)	FF	PCE (%)
1	31.9	0.181	0.525	0.446	0.132
2	31.9	0.202	0.525	0.432	0.144
3	31.9	0.191	0.515	0.415	0.125
4	31.9	0.193	0.482	0.431	0.125
5	31.9	0.153	0.485	0.352	0.082

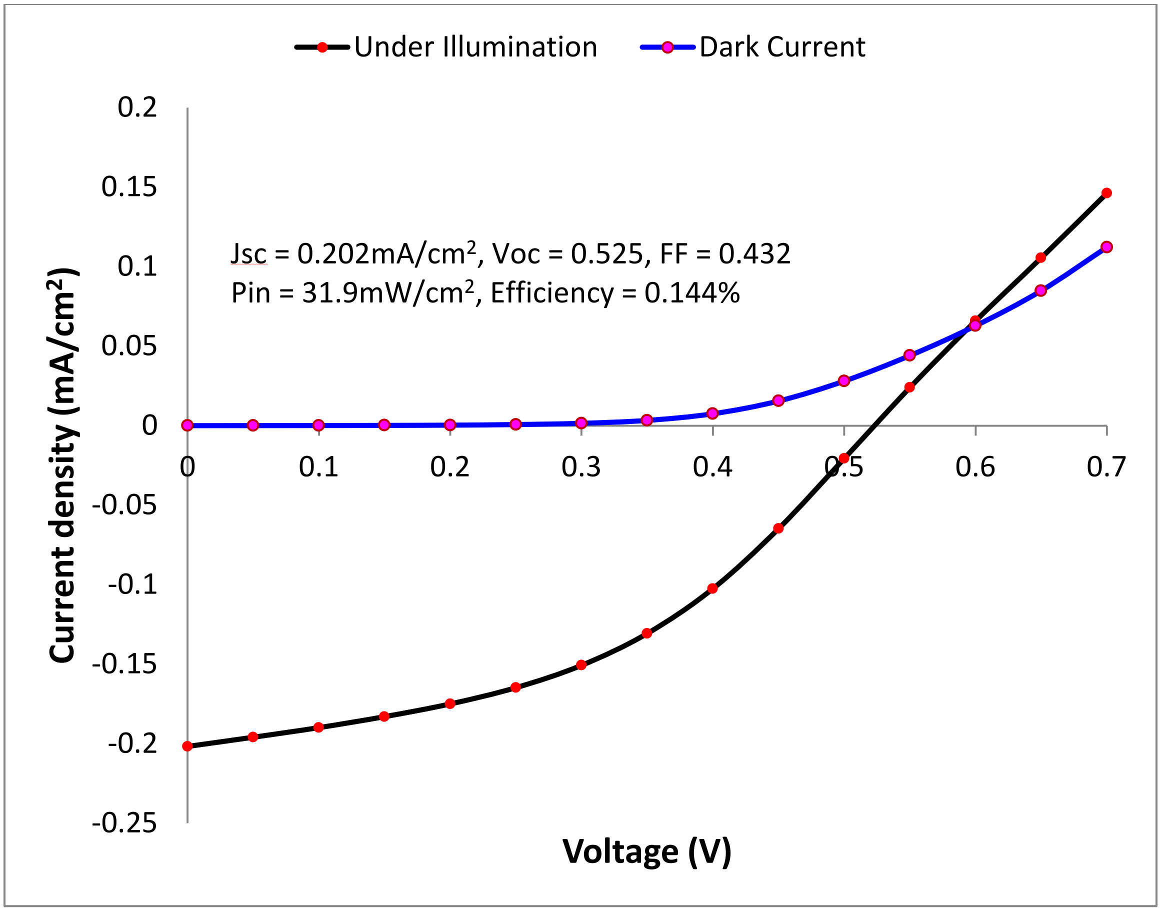

Figure 56: J-V characteristics of WSP based OPV cell under dark and illumination

4.5 Results and Discussion

WSP spin coating using DMSO resulted in micro crystals scattered all over the substrate as shown in Figure 46. DMSO has a high boiling point and evaporation of the solvent is quite slow during the spin process and hence crystal formation was faster than the solution could evaporate. Dektak Profilometer measurements showed that the crystals were as tall as 200 nm and the base of the crystals was at the height of about 70-80nm which was the thickness of PEDOT: PSS, Figure 47. This means there was almost no film of WSP after the spin coating, only crystals.

The basic solution of WSP in DI water had damaging effects on the slightly acidic PEDOT: PSS film. Micro crystals of WSP in circular patterns and a much bigger solid circle at the center were found. Crystallization occurs if the diffusion rate of WSP is faster than the solvent evaporation rate. The rotational speed during spin coating is higher as we move away from the center of the chip. Therefore, DI water starts drying farthest from the center first and approaching towards the center of the chip at last. This causes more crystallization at the center, Figure 49. The same WSP solution was also spin coated on ITO coated glass and again micro crystals were observed, possibly due to slower evaporation than the rate of crystal diffusion, Figure 48.

In case of ethanolic and methanolic solution of WSP, crystallite formation (Figure 50) on the PEDOT: PSS surface can be explained as before, i.e. a possible faster diffusion of the material than solution's evaporation rate.

A thin, continuous and uniform film of WSP as a donor layer is required in order for OPV solar cell to work effectively. To obtain a continuous film, the solution's evaporation rate was increased by heating it and the substrate while spin coating. An IR lamp was used to heat the solution and the substrate to 60-80℃ during the spin coating process. We believe that heating the solution increases the evaporation rate more than the diffusion rate, inhibiting crystal formation, and resulting in a continuous film, shown in Figure 51. This explanation is supported by the fact that dense crystal formation is seen near the corners (Figure 51) where more solution is stuck due to the surface tension interacting with the corner of the chip. With the greater volume of solution, it appears that evaporation was slow enough to form crystallites.

Applied voltages and corresponding current densities under light illumination and darkness were recorded and plotted, Figure 54. The short-circuit current J_{SC} was 0.202mA/cm^2, the open circuit voltage V_{OC} was 0.525V, the fill-factor was 0.432, at an equivalent solar power input of 31.9 mW/cm^2 leading to an overall power conversion efficiency (PCE) of 0.144%.

Incorporating the absorption spectra of WSP and C_{60} into our simulation model (Section 3.3), we show that the OPV cell performance can be optimized for parameters such as layer thicknesses and mobilities. The optimal power conversion efficiency is found to be about 0.67% whereas the actual PCE for WSP based cell was found to be 0.145% which is in the same order. The discrepancy could be due to assumptions of non-measured constants such as exciton diffusion lengths, effective density of states ($N_{c,}$ N_v), D-A interface width, band modification at electrode contacts due to charge transfer, chemical reactions or material degradation due chemical reactions etc. The layer thicknesses of donor and acceptor both have been chosen to be 50 nm in the fabricated device which is almost same as the optimal donor (WSP) and acceptor (C_{60}) thickness.

5. OPV Based on TTPO

In this chapter, we have studied the photovoltaic effect of a new and robust pentacene derivative 5,6,7-trithiapentacene-13-one (TTPO) molecule synthesized by Prof. Miller's group at University of New Hampshire, Durham. This pentacene is a small molecule semiconductor, (Figure 55) simple to synthesize and purify, that readily crystallizes, and sublimates in air at about 390^0C without decomposition. It is very stable against degradation in acid-free solutions.

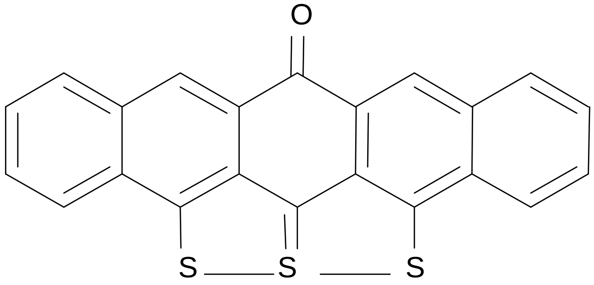

Figure 57: Chemical structure of 5,6,7-(trithia)pentacene-13-one (TTPO)

5.1 Introduction

Among acene groups which contain linearly connected benzene rings, pentacenes are the most widely studied class of organic semiconductor compounds having five benzene rings. They have been utilized as the active layers in organic field effect transistors (OFETs), organic photovoltaics (OPVs) and organic light emitting diodes (OLEDs). However, pentacene and most of its derivatives have photo-instability issues. Pentacenes functionalized with silylethynyl[139, 140] and organothio[141] groups are less prone to photo-degradation compared with unfunctionalized pentacene. In the presence of air and light these are still not very stable at higher temperature. Very few organic semiconductor based devices operating at temperature in excess of 100°C were known. An OFET using a thin film of 6,13-bis(triisopropylsilylethynyl)pentacene (TIPS-pentacene) suffers degradation above 120°C[142]. OFET constructed using 5,5′-bis(2-

anthracenyl)-2,2′-bithiophene and 5,5′-bis(2-tetracenyl)-2,2′-bithiophene continued to show an increased mobilities up to temperatures of 125℃ and 225℃, respectively and then started decreasing[143].

The newly synthesized small molecule TTPO shows excellent photo-oxidative and thermal stabilities. It is prepared from sulphur and pentacene-6,13-diol or 6(13H)-pentacenone. TTPO melts in air at about 390℃ without decomposition and it has optical and electrochemical LUMO-HOMO gaps of 1.9 eV and 1.71 eV respectively. It shows an excellent solid state thermal stability (>400℃) and can be thermally evaporated to obtain uniform thin films. A preliminary study of a FET device fabricated from this material by Erfan Kheirkhahi in our research group showed very small but increasing mobility up to 150 °C temperature.

5.2 Fabrication of TTPO based OPV

We fabricated a bilayer OPV cell using TTPO as the donor and C_{60} as the acceptor active layers. A schematic of the cell with a structure ITO/PEDOT: PSS/TTPO/C_{60}/Al, is shown in Figure 56. The process of cleaning of ITO coated glass substrates, partial etching of ITO, plasma cleaning and then coating of PEDOT: PSS as the electron blocking layer were followed as for fabrication of the WSP based cell mentioned in the previous chapter.

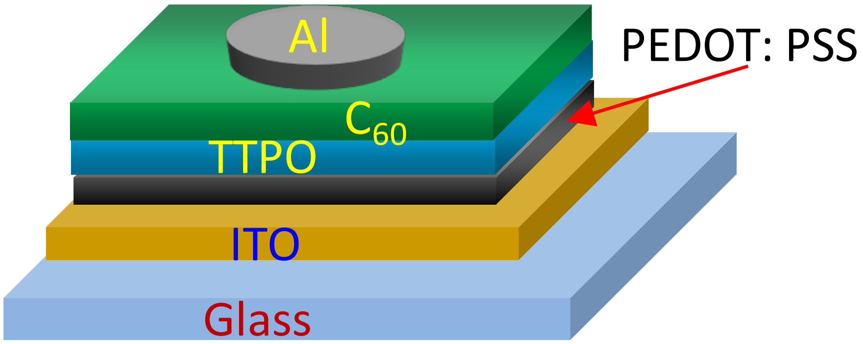

Figure 58: Structure of a TTPO based OPV cell

TTPO (20nm) as a donor layer and C_{60} (80nm) as an acceptor layer was thermally evaporated on top of the PEDOT: PSS layer using the Thermal Evaporator in two sessions with base pressure of $5x10^{-7}$ torr each. In order to not have TTPO and C_{60} coatings on inner wall of the Thermal

Evaporator's chamber, aluminum foil was used. This would help to avoid a secondary evaporation of TTPO and C_{60} during the next evaporation session. Finally, the cathode layer of Al (120nm) was evaporated on the C_{60} substrate using the shadow mask.

5.3 Results and Discussion

A calibrated incandescent halogen lamp described in Section 4.4 was used for light input which was 33.3 mW/cm^2 sunlight equivalents. I-V curves were recorded using a 4155 HP Parameter Analyzer and a LabVIEW program. For taking electrical measurements at higher temperatures, the halogen lamp was shone from the transparent window side of the device while at the same time an IR lamp of 250W was placed nearly 4 inch away from the device to heat it up. Table 4 presents the performance of four TTPO cells at room temperature under halogen light and also light with IR heating. Device performances have been recorded at three different temperatures, i.e. room temperature (23℃), 80℃ and 130℃. At room temperature, PCE of cells was found to be varied in three orders (1.3×10^{-6} % to 1.3×10^{-3} %). Upon heating devices with IR lamp at 80℃ along with halogen light illumination, all cells were found delivering increased short circuit currents but decreased open circuit voltages. Fill factors were slightly improved. Devices at nearly 130℃ showed even further improvement in short circuit currents and slight improvement in fill-factors but decremented open circuit voltages. Three devices showed lower PCE and one showed higher PCE at 130℃ compared it with at 80℃. Overall power conversion efficiencies were found to be increased in all four cells by factor of 3.33, 22.1, 1.1, and 153, respectively when comparing PCEs at room temperature. The best performing cell at room temperature showed a short-circuit current of 7.78µA/cm^2, an open-circuit voltage 0.45V, and a fill-factor of 0.12 rendering a PCE of $1.3\text{x}10^{-3}$%. The same cell was found to deliver the maximum PCE upon heating the device with IR lamp at 130℃ along with halogen light illumination. In this case, the short circuit current was increased 3.2 times to 25µA/cm^2 but open circuit voltage decreased to 0.08 V and PCE with slight improvement of $1.5\text{x}10^{-3}$%.

While keeping light input intensity constant, the device showed an increased photocurrent at raised temperatures possibly because increase in mobilities in TTPO at higher temperatures. In disordered systems, the hopping transport is improved at higher temperatures as barrier created by energetic disorder in an organic semiconductor is overcome as previously discussed in Section 2.5.5 [99]. The mobility of such materials vary exponentially fitted curve with inverse temperature as $e^{(-\Delta/T)}$ where Δ is the activation energy relating the amount of disorder in the system. The same can also be explained by multiple trap and release (MTR) model where charge carriers in localized or trap states thermally activated into band states, i.e. thermal energy $k_BT >$ trap energy, and mobility is increased [95, 99].

Table 4: Performance of TTPO based cells under light only and light with IR heating

Light illumination only (Room temperature)				**Illumination + IR heating (~80℃)**				**Illumination + IR heating (~130℃)**			
V_{OC} (V)	**J_{SC} (μA/cm^2)**	**FF**	**PCE (%)**	**V_{OC} (V)**	**J_{SC} (μA/cm^2)**	**FF**	**PCE (%)**	**V_{OC} (V)**	**J_{SC} (μA/cm^2)**	**FF**	**PCE (%)**
0.30	1.50	0.20	2.7×10^{-4}	0.25	6.00	0.20	9.0×10^{-4}	0.11	8.21	0.25	6.8×10^{-4}
0.19	0.14	0.18	1.4×10^{-5}	0.18	2.88	0.20	3.1×10^{-4}	0.10	4.50	0.22	3.0×10^{-4}
0.45	7.78	0.12	1.3×10^{-3}	0.20	11.7	0.20	1.4×10^{-3}	**0.08**	**25.6**	**0.25**	$\mathbf{1.5\times10^{-3}}$
0.25	0.015	0.23	1.3×10^{-6}	0.13	2.12	0.25	2.0×10^{-4}	0.09	3.11	0.22	1.8×10^{-4}

The best performing cell had a PCE of 1.5×10^{-3} % which is about 1000 times less than conventional OPV made of pentacene/C_{60} bilayer. A reason for such poor performance is its very low mobility in the order of 10^{-9} cm^2/V/s which is measured by Erfan Kheirkhahi in our research group.

Although, mobility was found to be increasing with temperature up to 150℃, OPV cells had reduced PCE at 130℃ compared with 80℃ mainly due to sharp decrease in open circuit voltages. Such loss of open circuit voltages at higher temperatures could have been the result of degradation of either TTPO or C_{60} or both changing the HOMO-LUMO levels or chemical reactions at interfaces changing the band alignment etc.

In our simulation results (Section 3.3), we have shown that PCE start decreasing fast for mobilities below 10^{-5} cm^2/V/s. For TTPO hole mobility and C_{60} electron mobility [10^{-7} cm^2/V/s, 10^{-4} cm^2/V/s], simulated PCE is 0.018% and this is mainly because of a low hole mobility. We had difficulty with simulating the model for lower mobilities ($<10^{-7}$ cm^2/V/s) due to convergence issues as charge carrier concentration and electric field at interfaces changes very sharply.

6. BHJ OPV Cell using $BC_{60}DTP$

A new organic semiconductor material, a [60]fullerene adduct of 6,13-bis(decylthio)pentacene or $BC_{60}DTP$ has been synthesized by the research group of Prof. Glen Miller at University of New Hampshire, Durham. In this chapter, we will study the photovoltaic effect of $BC_{60}DTP$. The fabrication procedure and the cell's characteristics for different photoactive layer widths will also be discussed.

6.1 Introduction

Recently, Kaur et. al. has found that thio-substituted pentacene has a half-life time of 750 min is considerably more stable than many other available functionalized pentacenes [127]. Cyclo-addition of [60]fullerene with 6,13-bis(decylthio)pentacene or DTP to form $BC_{60}DTP$ is done in either solution form at room temperature or refluxing in solid form at higher temperature (> 100°C)[Prof. Miller group's unpublished data]. The chemical structure of $BC_{60}DTP$ is shown in Figure 57. The material carries two fullerene molecules and it acts as an acceptor. BHJ solar cells have advantages over planar or bilayer structures as its three dimensional donor-acceptor intermixed domains causing increased interfacial area that is much more efficient in exciton generation. Properly fabricated and optimized BHJ devices with bi-continuous path to its respective electrodes make them more efficient compared to planar cells. Solution processable donors or acceptors are ideal choice for OPV as it requires much less time to spin coat the layer compared with evaporation method. A slow drying after spin coating the material results in phase segregation that is important for percolated paths for charge transport. Since $BC_{60}DTP$ is well soluble in organic solvents like toluene, carbon disulphide and o-dichlorobenzene (o-DCB) etc., a BHJ solar cell fabrication is possible coupled with donor such as P3HT which is also soluble in toluene, CB or o-DCB.

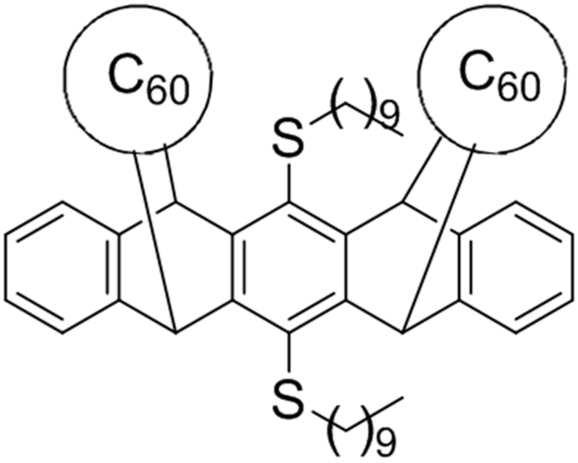

Figure 59: Chemical structure of BC$_{60}$DTP acceptor [*Prof. Miller group's unpublished result*]

6.1.1 Electronic Properties of BC$_{60}$DTP

UV-Vis and Cyclic voltammetry (CV) studies were done in o-DCB solution and compared with C$_{60}$ acceptor [*Prof. Miller group's unpublished result*]. Absorption spectrum of BC60DTP was found to be superior to that of C$_{60}$ between 350nm and 750nm range, shown in Figure 58. CV results for HOMO-LUMO energy levels and optical gap for BC$_{60}$DTP and C$_{60}$ are shown in Table 5 below. LUMO for both materials is same but HOMO for BC$_{60}$DTP varies between -5.64 eV and -5.44 eV [*Prof. Miller group's unpublished result*].

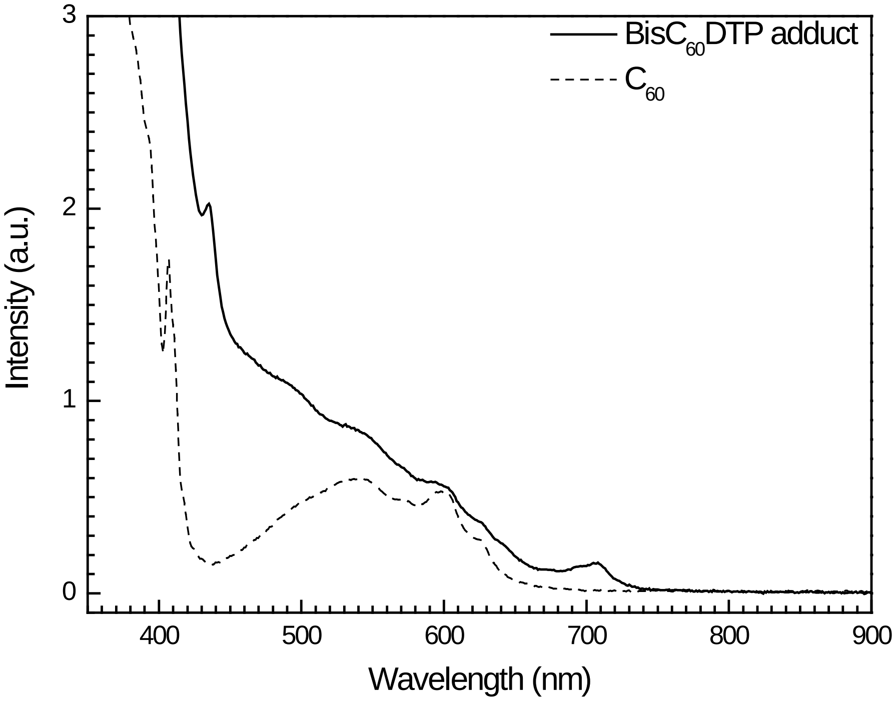

Figure 60: UV-Vis spectra of $BC_{60}DTP$ and C60 in o-DCB [*Prof. Miller group's unpublished result*]

Table 5: LUMO-HOMO energy and optical band gap for [60]fullerene and $BC_{60}DTP$

Materials	LUMO (eV)	HOMO (eV)	Optical bandgap (eV)
C_{60}	-3.74	-5.66	1.92
$BC_{60}DTP$	-3.74	-5.44 to -5.64	1.7 – 1.9

6.2 Bulk Heterojunction Solar Cell Fabrication and Characterization

The basic device structure of $BC_{60}DTP$ based OPV cell is shown in Figure 59. Glass substrate coated with ITO acts as a transparent anode and PEDOT: PSS as an electron blocking layer. Aluminum cathode is on the top of the layer of P3HT: $BC_{60}DTP$ blend.

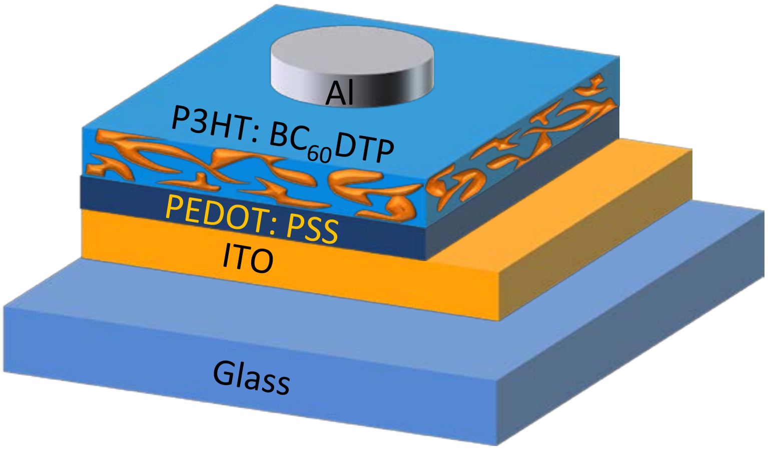

Figure 61: Schematic of $BC_{60}DTP$ based OPV device

The fabrication steps of dicing, cleaning, etching and spin coating of the electron blocking layer (PEDOT: PSS) are the same as the fabrication steps followed in Chapter 4. The step which differs here in fabricated a bulk heterojunction (BHJ) solar cell (Figure 60) is coating the film of the active layer.

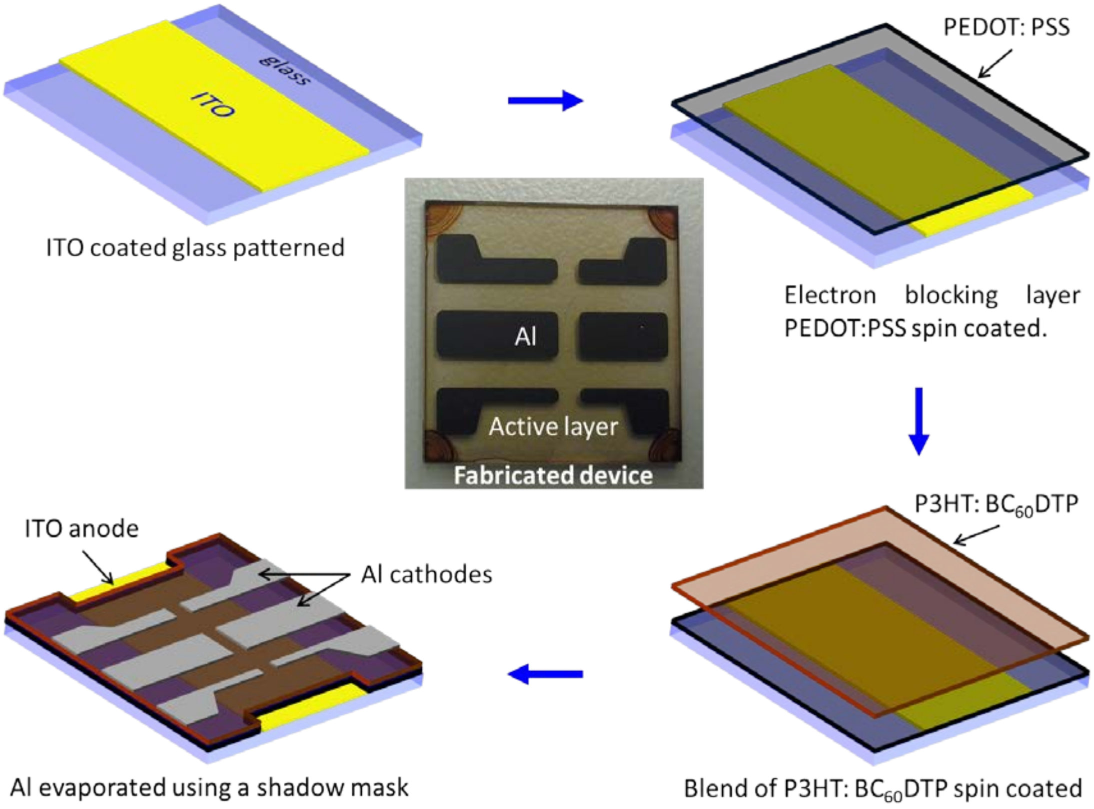

Figure 62: Fabrication steps of $BC_{60}DTP$ based OPV device

We used two different concentrations of P3HT and $BC_{60}DTP$ and dissolved in 1ml of o-DCB as both are well soluble in CB or o-DCB. Two blends of P3HT: $BC_{60}DTP$ (10mg: 9.5mg and 20mg: 18mg) in 1 ml of o-DCB are prepared by using a hot plate at 60℃ and magnetic stirring for 30min. The solution is then filtered using a PVDF filter with 0.45µm pores. To get different thicknesses of the active layer, three spin speeds (1000 rpm, 1500 rpm and 2000 rpm) were used for 1 min using a Laurell WS-400 Spinner. The substrates were baked for 2 min on a hotplate at 120℃.

At a base pressure of $5x10^{-7}$ torr in the Veeco Thermal Evaporator, a 110 nm of aluminum as a cathode layer was evaporated at the rate of ~10 Å/s, using a shadow mask.

Post fabrication baking of devices was done for 1 min on the hotplate at 100℃ before electrical characterization of OPV cells. Post fabrication bake is a standard process to achieve a better phase segregation BHJ devices.

4155A HP Semiconductor analyzer was used for I-V measurements under the illumination of calibrated halogen lamp (Dolan Jener Fiber-lite). The calibration was done by comparing the short-circuit current under the sunlight of known intensity and also the halogen light source, as discussed in Section 4.4. The halogen light sunlight equivalent intensity is $32mW/cm^2$. A LabVIEW program was used for generating I-V characteristics of the OPV cell. Table 6 and Table 7 show the fabrication parameters and device electrical measurements for two different blends of P3HT: $BC_{60}DTP$ (10mg: 9.5mg)/ml and (20mg: 18mg)/ml, respectively in o-DCB solvent.

6.3 Results and Discussion

P3HT as a donor and $BC_{60}DTP$ as acceptor material are blended (10mg: 9.5mg)/ml in o-DCB to make a BHJ active layer film on PEDOT: PSS substrate. Three different spin speeds were chosen. Spin coating at 2000 rpm yielded a film of 45nm. Similarly, lower spin speeds (1500 and 1000 rpm) gave thicker films (65nm and 85nm respectively). It is observed that the short circuit current was the least in case of 45nm thick film and the highest for 85nm film. This concludes that 85nm thick film was able to absorb more light and generate more useful charge carriers. The fill-factor was found to be less than 0.25 for all samples. Using the halogen lamp equivalent power input of $32mW/cm^2$, the power conversion efficiency was found to be quite low (45nm:

0.002%, 65nm: 0.034%, 85nm: 0.055%). This is mainly because of cells suffered from quite low short circuit (SC) current and also low fill-factor.

We approximately doubled the concentration of P3HT and $BC_{60}DTP$ both almost twice than before, i.e. 20mg: 18mg dissolved in 1ml of o-DCB to increase the thickness of the active layer. Cells fabricated from this blend are characterized under the same condition as before. The fabrication parameters and electrical output characteristics of the cells made from this blend are shown in Table 7. These samples were spin coated at 1500 rpm.

In sample 8, the electron blocking layer (PEDOT: PSS) coating was skipped to see the cell performance in absence of it. The short circuit current was found to be very low (0.9μA/cm^2). This confirms that excitons are being quenched and also dissociated electrons being recombined with holes at anode-active layer interface.

Table 6: Fabrication parameters and electrical output results of OPV cell with blend of P3HT: $BC_{60}DTP$ (10mg: 9.5mg)/ml in o-DCB

Sample #	1	2	3
Spin speed (rpm)	2000	1500	1000
Active layer thickness (nm)	45	65	85
Post spin-coat baking (℃, min)	120℃, 2m	120℃, 2m	120℃, 2m
Post fabrication bake (℃, min)	100℃, 1m	100℃, 1m	100℃, 1m
J_{SC} (μA/cm^2)	16	120	162
V_{OC} (V)	0.22	0.50	0.47
FF	0.19	0.18	0.23
% PCE	0.002	0.034	0.055

The thickness of the active layer for other samples (4-7) was found to be between 115-140nm. Samples with 130nm and 140nm thin film showed much larger short circuit currents (0.356 and

0.417mA/cm^2, respectively) and this is possibly due to thicker active layers that could absorb more of sunlight to convert into useful current. Interestingly, samples with 115nm and 120nm thin film, on the other hand, showed much poorer performance, especially the SC currents (1.7 and 2 mA/cm^2, respectively). The only difference in these two cases is that samples of 130nm and 140nm films were baked after spin coating whereas samples of 115nm and 120nm films were not. Since the solvent o-DCB was still trapped inside the thick active layer of the blend in case of 115nm and 120nm film samples which were not baked after the spin coating, the acceptor material BC$_{60}$DTP might have degraded in non-solid state phase during the span of rest of the fabrication processes.

Table 7: Fabrication parameters and electrical output results of OPV cell with blend of P3HT: BC$_{60}$DTP (20mg: 18mg)/ml in o-DCB

Sample #	4	5	6	7	8
Spin speed (rpm)	1500	1500	1500	1500	1500 (no EBL)
Active layer thickness (nm)	140	130	115	120	50
Post spin-coat baking (℃, min)	120℃, 2m	120℃, 2m	No bake	No bake	120℃, 2m
Post fabrication bake (℃, min)	100℃, 1m	100℃, 1m	100℃, 1m	100℃, 1m	100℃, 1m
I_{SC} (μA/cm^2)	356	417	1.7	2	0.9
V_{OC} (V)	0.24	0.40	0.10	0.31	0.28
FF	0.19	0.222	0.19	0.12	0.13
% PCE	0.05	0.115	1×10^{-4}	2×10^{-4}	3.3×10^{-4}

I-V characteristics of the best performing BHJ solar cell with 130nm thick active layer film of P3HT: BC$_{60}$DTP blend is shown in Figure 61. Maximum efficiency recorded was 0.116% which is about 40-50 times lower than the standard P3HT: PCBM based OPV cells.

Although absorption spectrum of $BC_{60}DTP$ is very much similar to that of PCBM, it fails to deliver a comparable performance of P3HT: PCBM based bulk heterojunction device. The low fill-factor (high series resistance) and low short circuit current indicates $BC_{60}DTP$ has possibly a very low hole mobility, i.e. much lower than electron mobility in P3HT (~$10^{-4}cm^2/V/s$). In such a case, lower mobile charge carriers mainly decide the performance of the cell as after dissociation the higher mobile carriers (electrons) have to wait for the lower mobile carriers (holes) to recombine. Another reason could be that we used the blend of only 1:1 weight ratio and $BC_{60}DTP$ sample has two fullerene molecules where more appropriate blend ratio could have been about 2:1 (P3HT: $BC_{60}DTP$).

Vertical gradient of phase has been found during spin cast method where PCBM-rich phase near the anode and P3HT-rich phase is near cathode due to difference in surface energy differences between P3HT and PCBM. Such vertical gradient has been reported by X-ray photoelectron spectroscopy [109]. Such kind of reverse phase segregation could be more pronounced in P3HT and $BC_{60}DTP$ system where hole diffusion towards cathode will directly reduce the short circuit current. Hence, an XPS study could be a right approach to confirm this.

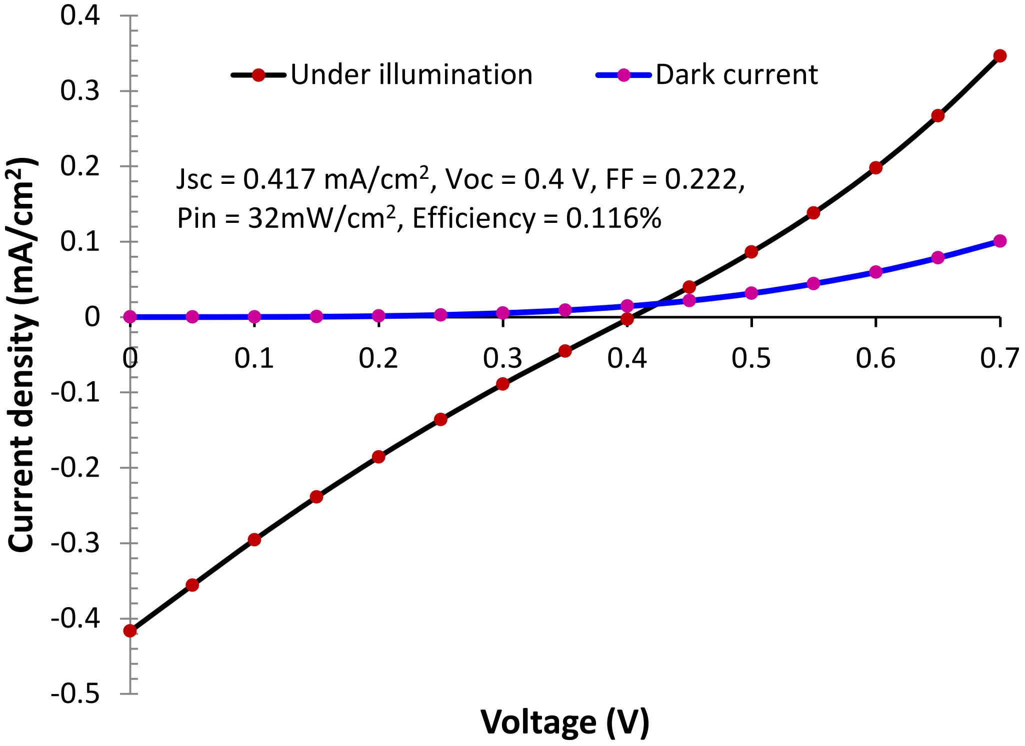

Figure 63: J-V characteristics of $BC_{60}DTP$ based BHJ solar cell

7. Conclusions and Future Work

We built OPV cells based on three new organic semiconductor materials synthesized by Prof. Glen Miller's group at UNH, Durham.

Water Soluble Pentacene (WSP), a new derivative of pentacene is environmental friendly as it can be dissolved in water and does not need harmful organic solvents like chlorobenzene. It can be solution processed whereas most of the pentacenes need more expensive evaporation techniques to make the thin film. Forming a thin and continuous film coating from this new pentacene molecule was a challenge as it formed crystals during the spin coating process. A method of infrared heating while spin coating the WSP solution, was found to solve the problem. Bilayer solar cells were successfully fabricated to achieve an efficiency of 0.145%. A fill factor of 0.432 which is still low compared to other pentacene based OPV cells (FF = 0.6-0.65) suggests that the cell has a high series resistance. Low mobility is a likely cause for low FF and low short circuit current, given that the layer thicknesses are optimized.

A new pentacene derivative, TTPO is very stable up to the temperature of 400℃ and yields a nice, controllable thin film by sublimation in thermal evaporator. TTPO behaves as a donor when coupled with the acceptor C_{60}. The active layers were coated by evaporation of TTPO and C_{60} in the thermal evaporator and a bilayer OPV cell was fabricated. Characterization at three temperatures was done and showed that the photovoltaic performance increased with increasing temperature up to 80℃. Since the mobility was recorded to be quite low (10^{-9}cm^2/V/s) (measured by Erfan Kheirkhahi, PhD candidate from our research group), we believe this may be the reason for the low efficiency (1.5×10^{-3}%). From our simulation results, it shows that for pentacene/C_{60} bilayer system power conversion efficiency decreases sharply for hole or electron (or both) mobilities below 10^{-5}cm^2/V-s.

$BC_{60}DTP$, another newly synthesized pentacene derivative is fullerene adduct that acts as an acceptor. Because of its solubility in chlorobenzene or similar solvents and its very good stability in the solution form, it is a good candidate for solution processed OPVs. A bulk heterojunction solar cell was successfully fabricated with P3HT as a donor and characterized. A maximum efficiency of 0.115% was measured with a fill factor of 0.22. Since hole mobility in the donor (P3HT) is about 10^{-3}cm^2/V/s, a much lower electron mobility in $BC_{60}DTP$ could be the reason for low short-circuit current and fill factor.

OPV device modeling and simulation for a bilayer structure was performed for ITO/pentacene/C_{60}/Al system to investigate the effect of cell parameters on electrical performances such as short circuit current, open circuit voltage, fill-factor and power conversion efficiency. A very simple model of exciton generation was taken from a literature source and utilized in standard drift-diffusion equation to formulate the problem. The model was modified to calculate electric field at the donor-acceptor interface more accurately. This was done by minimizing the error between calculated anode-to-cathode potential difference and effective applied voltage, to a tolerance level. Accurate calculation of interface electric field was necessary to find the more accurate solution of two boundary valued problem. First, keeping hole and electron mobilities equal, the performance was optimized for donor and acceptor layer thicknesses and their mobility in a bilayer cell. It was found that for lower mobilities (10^{-6} and 10^{-5} cm^2/V-s), PCE had maximum values for 30nm thick donor and 10nm thick acceptor. For higher mobilities ($\geq 10^{-4}$ cm^2/V-s), 50nm thick donor and 50nm thick acceptor showed the highest efficiency. Overall highest PCE of 0.67% was found at mobilities of hole and electron both were 10^{-4} cm^2/V-s. We also studied the effect of mobility imbalance and quantified by the ratio of mobilities of hole and electron or vice versa. It was found that mobility imbalance has adverse impact on PCE for higher mobility cases ($\geq 10^{-4}$ cm^2/V-s). But for lower mobilities ($<10^{-6}$ cm^2/V-s), smaller imbalance (up to 100) in mobilities in fact enhances the PCE and larger imbalance ($\geq 10^4$) causes a reduction in PCE when it is compared with the PCE in balanced mobility case. Therefore, we state that it's not pure imbalance in mobilities which cause the drop in PCE but increase in mobility one of the charge carriers above 10^{-4} cm^2/V-s decreases the PCE.

PCE rapidly increases with increase in exciton diffusion length in the donor L_{dd} initially and showed saturation for $L_{dd} > 50$nm. Hence, the efforts can be made to enhance diffusion length up to 50nm.

Future Work and Suggestions

Pentacene based OPVs in the literature generally show power conversion efficiency (PCE) about 2% whereas the water soluble pentacene (WSP) based OPVs studied here showed PCE up to 0.15%. One reason could be its low mobility. This should be confirmed by measuring it directly. Knowing the mobility of WSP can give an idea if the material can be used for pursuing further research on improving the cell efficiency. Mobility extraction by the time-of-flight method will be more useful as it measures the mobility of a thin film perpendicular to it (or bulk mobility) which is the way charge carriers transport to the electrode in OPVs.

A damaging effect of a basic solution of WSP on acidic PEDOT: PSS film has been observed and presented in this thesis. This effect might have a negative impact on charge carrier transport and hence the efficiency. Hence, 2-dimethylaminoethanol (DMAE) or ammonium hydroxide can be used to neutralize the PEDOT: PSS solution before it is spin coated on ITO [144]. Molybdenum trioxide (MoO_3) can also be used as an alternative to PEDOT: PSS as electron blocking layer. Thin film coating of MoO_3 on ITO surface can be sublimated in thermal evaporator above 800℃ temperature.

Titanium dioxide (TiO_2) can be incorporated in WSP based OPV cell design for following many reasons – (i) it has LUMO-HOMO levels of 4.4 eV and 6.4 eV, respectively that is an excellent electron acceptor and its LUMO level perfectly aligns up with aluminum electrode (ii) TiO_2 has a good mobility ($\sim 5\times10^{-4}$ $cm^2/V\text{-}s$) near to our calculated optimal value to achieve maximum power conversion efficiency, (iii) TiO_2 nanoparticles can be well suspended in ethanol and WSP being soluble in ethanol, a bulk heterojunction solar cell with new structure ITO/PEDOT: PSS/WSP:TiO_2/Al can be fabricated. This fabrication will lead to a reduction in fabrication cost as it does not need expensive and time consuming thermal evaporation of fullerene (C_{60}) as an acceptor as well as bulk heterojunction structure will be more efficient in exciton dissociation due to increased donor-acceptor interface area. TiO_2 can easily be prepared by hydrolysis of titanium isopropoxide in ethanol in presence of acetic acid [145].

Absorption profile of $BC_{60}DTP$ is much superior to C_{60} and hence it has a great potential in making high efficiency OPV cell given that it has mobility greater than 10^{-4} $cm^2/V\text{-}s$. Hence, we need to measure its bulk mobility as we discussed for WSP. $BC_{60}DTP$, a fullerene adduct of 6,13-bis(decylthio)pentacene has two C_{60} molecules which act as acceptors. We successfully fabricated and tested BHJ solar cells with a blend of P3HT (as donor) and $BC_{60}DTP$ (as acceptor) in 1:1 ratio. The blend of P3HT: $BC_{60}DTP$ in a ratio of 2:1 may be a better matching of donor-acceptor interface for more efficient charge dissociation. We have studied the performance up to the active layer thickness of 140nm and a thicker layer (>150nm) can also be studied. By spin coating the blend of P3HT (20mg): $BC_{60}DTP$ (19mg) in 1ml of o-DCB yielded 140nm thick active layer. In the new design we can use P3HT (30mg): $BC_{60}DTP$ (15mg) in one ml of o-DCB solvent. The phase segregation is important for effective charge transport and PCE is very sensitive to the amount of segregation which is dependent on pre/post baking of devices. Hence, the effect of baking (temperature and bake time) on phase segregation of active layer must be studied via AFM phase imaging or SEM contrast imaging.

Based on our simulation results for pentacene (50nm)/C_{60} (50nm) bilayer system in a typical case of exciton diffusion lengths (pentacene: 20nm, C_{60}: 5nm), we found that ratio of exciton flux density at the D-A interface due to donor and acceptor is about 26:1. The contribution of C_{60} in exciton generation is very low due to its narrow absorption spectrum and smaller diffusion length. Hence, we should look for alternative acceptor materials having larger diffusion length and suitable absorption profile that compliments the absorption spectrum of the front active layer or donor material for absorbing sunlight more efficiently.

Organic semiconductors and polymers are known for degradation under oxygen, moisture and UV light. Parylene, an inexpensive material has excellent physical and chemical properties such as high tensile and yield strength, conformal and tension free coating, excellent transparency in visible light and great UV light absorbent outstanding barrier or very low permeability to moisture and gases. We can coat the parylene C by CVD process as protective layer for OPV cells and evaluate the time dependent device performance [146].

The ITO, used as an anode in OPVs, has a planner form. Cihan et al [147] at Center for High Rate Nanomanufacturing, NEU Boston are able to assemble gold nanoparticles in the form of nanopillars. They are also able to make nanopillars from other conducting nanoparticles. Having nanopillars of (~100 nm diameter) ITO equally spaced by submicron length on ITO substrate can dramatically increase the surface area. Spin coat with WSP followed by thermal evaporation of C_{60} will make three dimensional bilayer structures. Such WSP cells with much enhanced interface area will improve exciton dissociation that may deliver the higher photocurrent and hence the PCE. Having the ITO nanopillars on ITO substrate might also be able to trap and collect more light leading to further increased photogeneration.

Bilayer OPV cells show maximum efficiency for hole and electron mobility at about $10^{-4}cm^2/V$-s according to our simulation finding. We need to focus on exploring new organic semiconductors having mobilities about this value. A similar attempt of optimizing the design for bulk heterojunction cells can be done.

8. Appendix

8.1 Measurement Setup

Input light power to the solar cell is needed for efficiency calculation. *I-V* characteristics of the solar cells are plotted using HP Parameter Analyzer 4155A and also Keithley 2410 with the help of LabVIEW program. Portable Keithley 2410 is used for the OPV cell characterization under the actual direct sunlight with known intensity and the data is used for calibrating the intensity of the halogen light source we used for cell characterization with HP Parameter Analyzer 4155A.

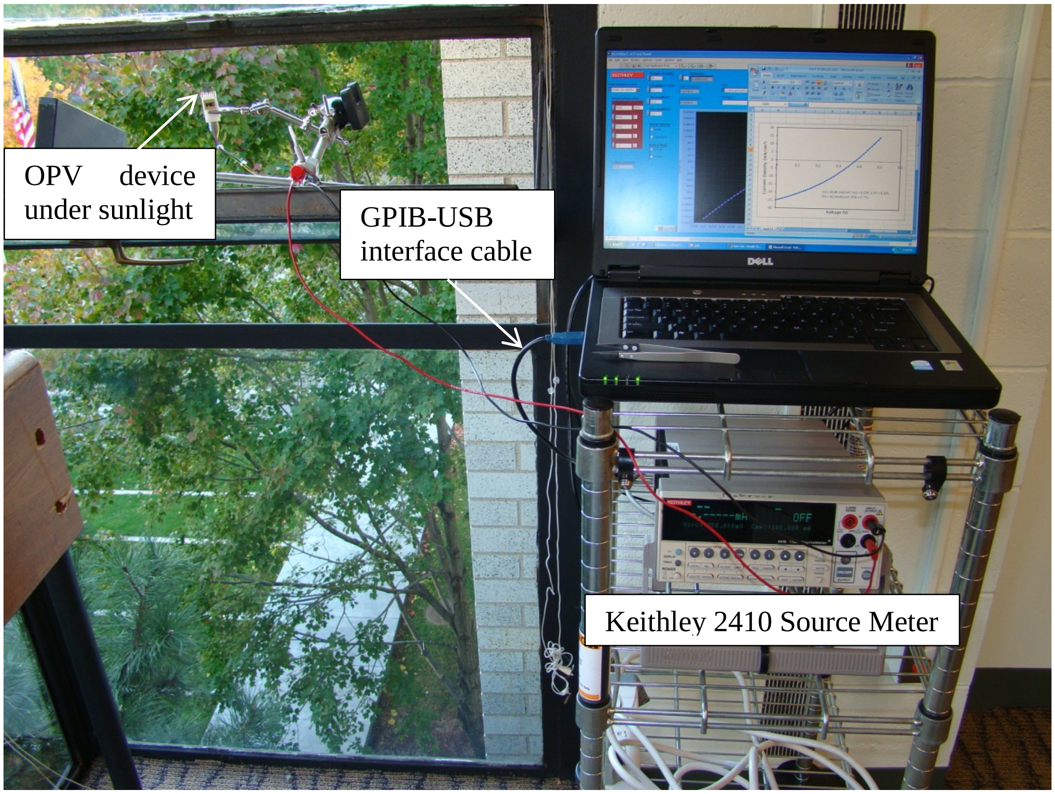

Figure 64: OPV device test under sunlight

Depending on the sun's inclination or zenith angle, date and location of the *I-V* measurement, air mass is estimated which is used for calculating direct and/or global incident or input power needed for efficiency calculation. A description about air mass is given in the following section.

8.1.1 Solar Radiation

8.1.1.1 Solar Spectrum and Air Mass

Solar spectrum closely matches the radiation of a black body at about 5777 K [148]. As sunlight travels through the earth's atmosphere, it is attenuated due to absorption and scattering, Figure 63. Ozone in the upper atmosphere absorbs the major part of the ultraviolet and small wavelength light. Water vapor attenuates many separate bands of wavelengths. Similarly, gases like nitrogen, oxygen, and carbon dioxide contribute to this process. Scattering of higher frequency lights results in reduced intensity of such lights reaching to earth basically causes the sky to appear blue and sun having yellowish tinges. Greater the distance the light travels, the more the absorption and scattering.

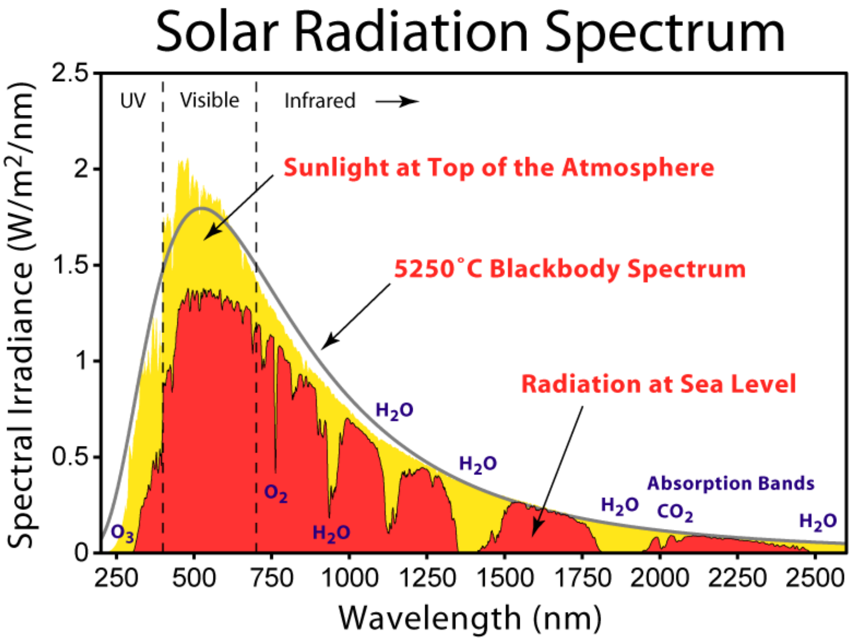

Figure 65: Solar radiation spectrum for direct light at both the top of the Earth's atmosphere and at sea level. (The curve is based on American Society for Testing and Materials (ASTM) Terrestial Reference Spectra).

Air mass is a unit-less quantity defined as the ratio of direct sunlight path length through the Earth's atmosphere to path length vertically upward or shorted path length. For a path length 'L' through the atmosphere and zenith angle 'z' relative to vertical axis to the Earth's surface, the air mass coefficient is defined by

$$AM = \frac{L}{L_o} \approx \frac{1}{\cos z}$$

Where, 'L_o' is the vertical path length from the Earth's surface at sea level, Figure 64. Air mass is approximated by the inverse of cosine of zenith angle considering a very large Earth's curvature and is reasonably accurate for the zenith angle up to 75°. AM0 means zero atmosphere, is the air mass coefficient normal to the Earth's surface outside the atmosphere (in space). AM0 spectrum is used for space applications. Similarly, AM1.5 and AM2.0 are the air mass coefficients for zenith angle 48.2° and 60° respectively. AM1.5 is the standard value of air mass based on yearly average energy received on mid latitude of the Earth's surface for which solar cells are mostly characterized.

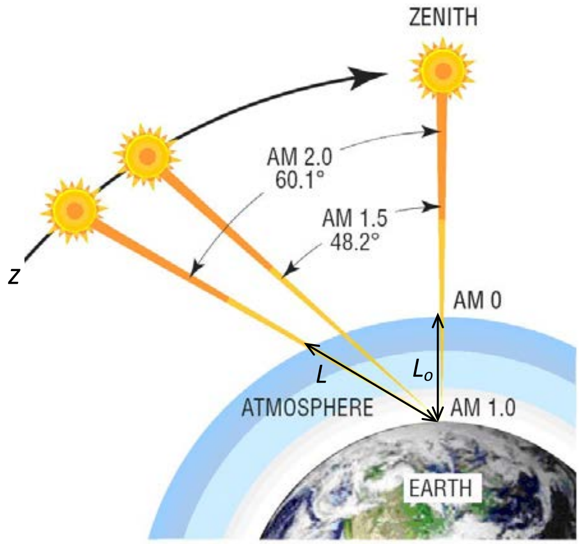

Figure 66: Representation of path length and zenith angle

From the above formula AM value is infinity for the Sun at horizon, i.e. at zenith angle 90°. But considering the Earth's curvature the path length is finite and geometrically it can be derived as [149]:

$$AM = \sqrt{(r\cos z)^2 + 2r + 1} - r\cos z$$

Where, $r = R_E/Y_{atm} \cong 708$. R_E is the radius of earth ≈ 6371km and Y_{atm} is the effective atmospheric height ≈ 9km. Air mass coefficient calculated from the above equation nearly equals 38 for the Sun at horizon.

8.1.1.2 Solar Light Intensity

As air mass coefficient increases the solar intensity decreases but not in linear fashion due nonlinear effect of the atmosphere. For example, AM2.0 is more than half the intensity of AM1.0 and similarly the intensity of the Sun at horizon is greatly attenuated by the lower level of dense atmosphere. An empirical relation for solar intensity versus air mass is given by [150]

$$I = 1.1 \times I_0 \times 0.7^{AM^{0.678}}$$

Where, I_0 is the intensity at external to Earth's atmosphere, AM0 = 1353W/m^2. The factor 1.1 is multiplied for the reason that the diffused sunlight contributes additional 10%.

8.1.2 A Cheap Alternative Solar Simulator

A solar simulator also called artificial sun produces light output equivalent to sunlight at earth or space. Simulators are also capable of producing lights of the sun at various zenith angles such as 0℃ (AM1.0), 48.2℃ (AM1.5), 60℃ (AM2.0).

The lamps used in solar simulators are mainly xenon-arc lamp, metal halide arc lamp and also quartz tungsten halogen (QTH) lamp. QTH lamps show a low spectral irradiance below 500nm wavelength. The best suited lamps for solar simulators are xenon-arc type. However, Xenon-arc lamps and metal halide arc lamps along with its starter electronic kit and high voltage protection circuitry are expensive and normally they cost more than $10000. We explored a cheaper alternative for such simulator, is to use xenon light source which is widely used for endoscopy in hospitals. Such new device cost around $3000 and used ones somewhere between $400 and $800, Figure 65 and Figure 66. Using fabricated device, the endoscopy lamp can be calibrated with respect to known sunlight intensity.

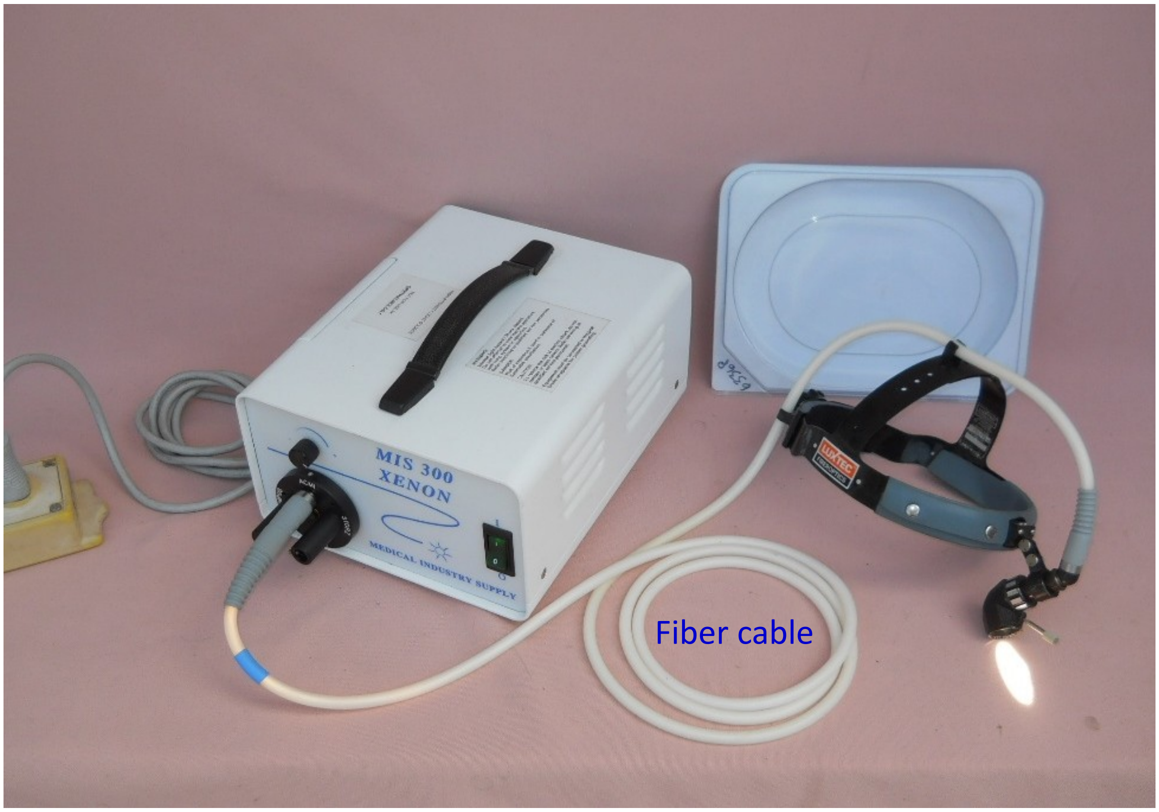

Figure 67: 300 watts xenon light source with fiber cable and surgical headlight used in endoscopy

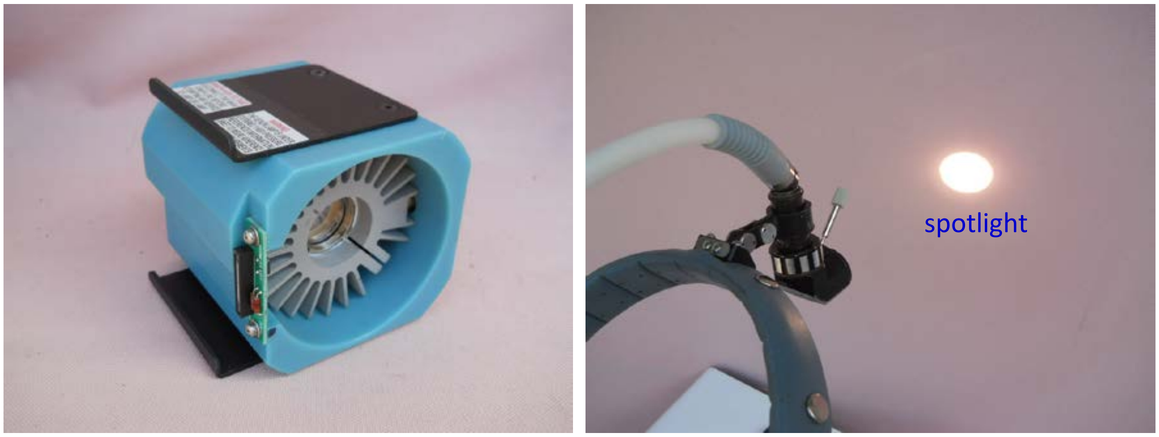

Figure 68: ***Left*****: Xenon lamp module inside the light source;** ***Right*****: spotlight diamete can be adjusted between 3/4 inch and 4 inch**

8.2 Process Run Sheet for WSP based OPV Fabrication:

Dicing and first cleaning:

Step	Process	Equipment	Method	Parameters
1	Dicing	Micro Automation 1006 Dicing Saw	ITO coated glass sheet (1.1 mm + 120nm) diced into 15mmx15mm chips) Kapton Dicing Tape	10000 rpm, 1.25mm/s Depth=1.1-0.1mm RESINOID 400 (35 mic)
2	Post-Dice Clean	Acetone Gun	-Acetone Gun	
			Ultrasonication in:	
			- Soap water	5 min
			- DI water flow rinse	3 min
			- Acetone	3 min
			- IPA	1 min
			- DI water flow rinse	3 min
			- N2 blow dry.	

ITO patterning:

Step	Process	Equipment	Method	Parameters
3	Photoresist masking	Laurell spinner WS 400 Lite, Hot plate	- Partially masked the substrate with Kapton Polyimide tape	
			- Spin coated 1818	
			- Baked on hot plate	4000 rpm, 1 min
			- Tape removed	115^0C, 1 min
4	HCl etching	Stirrer, N2 gun	- Etched in HCl (37%)	RT, 6 min while stirring
			- DI water flow rinse	5 min

Substrate cleaning:

Step	Process	Equipment	Method	Parameters
5	PR Strip	Acetone gun, Sonicator, N2 Gun	- Acetone gun clean Ultrasonication in: - Acetone - IPA - DI water dump rinse - N2 blow dry	 10 min 2 min 3 min

Substrate baking and plasma cleaning:

Step	Process	Equipment	Method	Parameters
6	Baking	Hotplate	Substrate baked	150^0C, 1 hour.
7	Oxygen plasma	ICP Therm 7900	O_2 plasma clean	Bias - 5W, Plasma - 300W 1min

Active layers coating:

Step	Process	Equipment	Method	Parameters
8	PEDOT: PSS spin coating	Laurell Spinner WS 400 Lite, Hot-plate	- PEDOT: PSS filtered - Spin coated - Baked on hot plate	(0.45µm) filter 4000 rpm, 1 min 120^0C, 20 min
9	Active layer spin coating (WSP)	IR Heat Lamp	- WSP in Ethanol filtered - WSP spin coated - Baked on hot plate	10mg/ml (1wt%), (0.45µm) filter, 2000 rpm, 1 min 80^0C, 1min
11	Thermal evaporation (C_{60})	Thermal evaporator	Evaporated C_{60} at slow rate	Press. < 10^{-7} torr evap. rate <$2A^0$/s thickness < 50mg (~60nm)

Cathode deposition:

Step	Process	Equipment	Method	Parameters
12	Thermal evaporation (Al)	Thermal evaporator	- Evaporated Al on substrates with shadow mask	Pressure $<10^{-7}$ torr Evaporation rate $<10A^{o}/s$ (100nm)

Post baking and measurement

Step	Process	Equipment	Method	Parameters
13	Post baking	Hot plate	Devices baked	80^{0} C - 100^{0} C for various times.
14	Measurements	HP Parameter Analyzer 4155, Kethley 2400, Fibre Optic light		I-V characteristics

8.3 MATLAB Code for the Device Simulation:

```
function VaJE = opvsol12(~,q,ep,muh,mue,Dh,De,Jxc,dx,nha,nec,Vbi,d)
   close all;
   clear all;

   Ein = 7.5132e6; j = 1; option = optimset('Display','iter','TolX',1e-3,'DiffMaxChange',1e-3);
   V1 = 0.0; V2 = 0.0; dV =0.05;                    % V1,V2 - Init & final voltage applied with dV volt-steps.
   pts = round((V2-V1)/dV)+1; J = zeros(1,pts); Va = J; Eint = J;
   for jv = 1:pts
      V = V1 + (jv-1)*dV;
      Ein = fzero(@opvsim,Ein,option); Eint(jv) = Ein;
      sprintf('Va = %.2f%s, J = %.4f%s, Recombination = %.3f%s, Ei = %0.5g%s',V,' V',-jh/10,'
mA/cm^2',Rep,'%',Ein,' V/m')
   end
   figure; plot(Va,J/10,'k',Va,J/10,'r.','LineWidth',2,'MarkerSize',16); grid
   xlabel('Voltage (V)'); ylabel('Current density (mA/cm ^{2})');

function delV = opvsim(Ei)
   if j == 1
   muh = 1e-8; mue = 1e-8;                 % hole and electron mobility(m2/V.s);
   d = [50e-9 50e-9]; dx = 0.4e-9;
   Ld = [20e-9 5e-9]; ni = 1e17;           % Ld - diffusion lengths in Donor and Accepotor
   d_l = 5;  q = 1.6022e-19;         % q_e = 6.03175e-9 = q/(eo*er)=1.602e-19/(8.854e-12*3) (V.m).
   kT = 0.0256;   hc = 1.9864e-25;   % kT=0.0256 eV.%  h*c = 6.626e-34*3e8 = 1.986e-25 (m3.kg/s2).
   ep = 2.6562e-11;                  % ep = eo*er
```

```
   Nc = 1e21; phi_c = 3.9; LUMOa = 3.7;   % Nc - effective density of states (/cm3). phi_c = cathode WF (eV)
   Nv = 1e21; phi_a = 4.7; HOMOd = 4.9;  % Nv - effective density of states (/cm3). phi_a = anode WF (eV)

% nx - excition concentration (/m3) at distance x
% a, phi - absorption coefficient (/m), photon flux (/m2.s)..
% Ld, d - excition diffusion length(m), layer thickness(m).
% h, c, e - plank's const(m2kg/s), light-speed (m/s), electron charge(Q)

% Wavelegth lambda (nm) vs Absorption coefficient alpha (/m)
lamb = 300:25:750;
aa1 = 1e7*[2.5 2.0 1.2 0.4 0.22 0.22 0.16 0.12 0.28 0.56 0.72 1.28 0.84 1.24 0.36 0.12 0.04 0.03 0.02];
aa2 = 1e7*[2.5 2.0 1.2 0.4 0.22 0.16 0.12 0.08 0.06 0.05 0.03 0.01 0.0 0.0 0.0 0.0  0.0  0.0  0.0];
Lamb = 300:5:750;
a1 = spline(lamb,aa1,Lamb); a2 = spline(lamb,aa2,Lamb);

load('AM1_5.mat', 'AM1_5');  % 300nm < Lamb < 750nm
%%%%%%%%%%%%%%%%%%%%%%%%%%%
nl = length(AM1_5); sizeD = floor((nl-1)/d_l+1); SI = zeros(sizeD,1); Lamb = SI;
d_W = zeros(sizeD-1,1); d_phi = d_W;  a_1 = d_W; a_2 = a_1;
d_Jxc1 = d_W; d_Jxc2 = d_Jxc1; Jxc1 = 0; Jxc2 = 0; b = 1./Ld;

for i=1:sizeD
   Lamb(i) = AM1_5((i-1)*d_l+1,1);
   SI(i) = AM1_5((i-1)*d_l+1,2);   % spectral irradiance W/m2.nm

   if i > 1
   d_W(i) = (SI(i)+SI(i-1))/2*d_l;                                 % average spectral power (W/m2).
   d_phi(i) = d_W(i)*((Lamb(i)+Lamb(i-1))*1e-9/2)/hc; % av. photon flux.

   a_1(i) = (a1(i)+a1(i-1))/2;  % average absorption coefficient.
   a_2(i) = (a2(i)+a2(i-1))/2;

   d_Jxc1(i) = d_phi(i)*a_1(i)*exp(-a_1(i)*d(1))*(a_1(i)-b(1)+2*b(1)*(exp(b(1)*d(1))-exp(a_1(i)*d(1)))/...
      (exp(b(1)*d(1))-exp(-b(1)*d(1))))/(b(1)^2-a_1(i)^2);
      % exciton flux density (/m2) at the interface due to donor.
   d_Jxc2(i) = -d_phi(i)*a_2(i)*exp(-a_1(i)*d(1))*(a_2(i)-b(2)-2*b(2)*(exp(-b(2)*d(2))-exp(-a_2(i)*d(2)))/...
      (exp(b(2)*d(2))-exp(-b(2)*d(2))))/(b(2)^2-a_2(i)^2);
      % exciton flux density (/m2) at the interface due to acceptor.
   Jxc1 = Jxc1+d_Jxc1(i); Jxc2 = Jxc2+d_Jxc2(i);
   end
end
Jxc = (Jxc1+Jxc2);   % total exciton flux at the interface (/m2/s).
%%%%%%%%%%%%%%%%%%%%%%%%%%%%%%%%%%%%%%%%%%%%%%%%%%%%%%%%%%%%

   nec = Nc*exp(-(phi_c-LUMOa)/kT)*1e6;       % nec - ne (/m3) at cathode. LUMOa - acceptor LUMO (eV).
   nha = Nv*exp(-(HOMOd-phi_a)/kT)*1e6;          % nha - nh (/m3) at anode. HOMOd - donor HOMO (eV)
   Dh = kT*muh; De = kT*mue; Vbi = (phi_a-phi_c);    % De(h) = kT/q*mu (m2/s) as kT = 0.0256 eV &q = 1e

   end
   Jh = q*Jxc; Je = -Jh;  % Jxc - exciton flux (/m2.s)
   nh = 1e23; ne = 1e23; Nh = q*nh; Ne = q*ne; jh = Jh; j = 2; f = 1;
   Vappl = Vbi-V;
%%%%%%%%%%%%%%%%%%%%%%%%%%%%%%%%%%%%%%%%%%%%%%%%%%%%%%%%%%%%
```

```
          dENJ = @(t,y)[y(2)
                    -(y(3)-y(1)*y(2)*muh/ep)/Dh
                    q*(Jxc/dx-y(2)*y(5)*(muh+mue)/(ep*q))*(t<=dx)
                    -y(5)
                    (-y(3)-y(4)*y(5)*mue/ep)/De];

          bcENJ = @(ya,yb)[ya(1)-ep*Ei; yb(2)-q*nha; ya(3); ya(4)+ep*Ei; yb(5)-q*nec];
%%%%%%%%%%%%%%%%%%%%
          option1 = bvpset('Stats','off');
          solinit = bvpinit(linspace(0,d(1),400),[ep*Ei Nh Jh -ep*Ei Ne]);
          sol = bvp4c(dENJ,bcENJ,solinit,option1);
          jh = sol.y(3,end);

          Rep = (1-jh/Jh)*100; Va(jv) = V; J(jv) = -jh;
   Xdon = fliplr(sol.x); Xacc = sol.x; Edon = fliplr(sol.y(1,:))/ep; Eacc = sol.y(4,:)/ep;
   E=[Edon -Eacc]; xx = [-Xdon Xacc]; E1 = [E(2:end) 0]; Eav = (E(1:end-1)+ E1(1:end-1))/2; delx = diff(xx);
   Vx = cumsum(-Eav.*delx); V21 = -Eav*delx'; delV = V21+Vappl;
end
   VaJE = [Va; J; Eint];
toc;
end
```

References

1. *IPCC Second Assessment*, in *Intergovernmental Panel on Climate Change*1995.
2. Hassan, A.Y., *Islamic Technology: An illustrated history*. Donald Routledge Hill, 1986.
3. *World Wind Energy Report 2010*. World Wind Energy Association WWEA, 2011.
4. *Use and Capacity of Global Hydropower Increases*, 2012, Worldwatch Institute.
5. *Basic Research Needs for Solar Energy Utilization*, 2005, US Department of Energy.
6. Perlin, J., *From Space to Earth: The Story of Solar Electricity*. 1999.
7. *Photovoltaic Milestones: US Energy Information Administration*: http://www.eia.gov/cneaf/solar.renewables/renewable.energy.annual/backgrnd/chap11i.htm.
8. Wolden, C.A., et al., *Photovoltaic manufacturing: Present status, future prospects, and research needs*. J. Vac. Sci. Technol. A, 2011. **29**(3): p. 030801.
9. *Crystalline Silicon Photovoltaics Research*, 2011, US Dept. of Energy: http://www1.eere.energy.gov/solar/sunshot/pv_crystalline_silicon.html.
10. Green, M.A., et al., *Solar cell efficiency tables (version 40)*. Prog. Photovolt. Res. Appl., 2012. **20**(5): p. 606-614.
11. Clarke, C., *San Jose Solar Company Breaks Efficiency Record for PV*, 2012: http://www.kcet.org/news/rewire/solar/photovoltaic-pv/san-jose-solar-company-breaks-efficiency-record-for-pv.html.
12. Gratzel, M., *Photoelectrochemical cells*. Nature, 2001. **414**: p. 338-344.
13. Gratzel, M., *Solar Energy Conversion by Dye-Sensitized Photovoltaic Cells*. Inorg. Chem., 2005. **44**.
14. Yella, A., et al., *Porphyrin-Sensitized Solar Cells with Cobalt (II/III)–Based Redox Electrolyte Exceed 12 Percent Efficiency*. Science, 2011. **334**(6056): p. 629-634.
15. Ip, A.H., et al., *Hybrid passivated colloidal quantum dot solids*. Nature Nanotechnology, 2012. **7**: p. 577-582.
16. Sariciftci, N.S., et al., Appl. Phys. Lett., 1993. **62**.
17. Karg, S., et al., *Electrical and optical characterization of poly(phenylene-vinylene) light emitting diodes*. Synth. Met., 1993. **54**(1-3).

18. Marks, R.N., et al., J. Phys. Condens. Mater., 1994. **6**.

19. Yu, G., et al., *Polymer Photovoltaic Cells: Enhanced Efficiencies via a Network of Internal Donor-Acceptor Heterojunctions.* Science, 1995. **270**.

20. Halls, J.J.M., et al., Nature, 1995. **376**.

21. Hoppe, H. and N.S. Sariciftci, *Organic solar cells: An overview.* Journal of Materials Research, 2004. **19**(7): p. 1924-1945.

22. Brabec, C.J., N.S. Sariciftci, and J.C. Hummelen, *Plastic Solar Cells.* Advanced Functional Materials, 2001. **11**(1): p. 15-26.

23. Spanggaard, H. and F.C. Krebs, *A brief history of the development of organic and polymeric photovoltaics.* Solar Energy Materials and Solar Cells, 2004. **83**(2-3): p. 125-146.

24. news, H. *Heliatek consolidates its technology leadership by establishing a new world record for organic solar technology with a cell efficiency of 12%.* 2013.

25. *Energy: Electricity*. Environmental Impact [cited 12/29/2012]; Available from: http://envimpact.org/taxonomy/term/10.

26. Krebs, F.C., *Fabrication and processing of polymer solar cells: A review of printing and coating techniques.* Solar Energy Materials & Solar Cells, 2009. **93**: p. 394-412.

27. Xiao, T., et al., *Simple routes for improving polythiophene:fullerene-based organic solar cells.* Organic Electronics, 2011. **12**(2): p. 257-262.

28. Chen, D., et al., *P3HT/PCBM Bulk Heterojunction Organic Photovoltaics: Correlating Efficiency and Morphology.* Nano Letters, 2011. **11**(2): p. 561-567.

29. Yang, P., et al., *P3HT:PCBM polymer solar cells with TiO2 nanotube aggregates in the active layer.* Journal of Materials Chemistry, 2010. **20**(13): p. 2612.

30. Kim, J.-H., et al., *Bulk heterojunction solar cells based on preformed polythiophene nanowires via solubility-induced crystallization.* Journal of Materials Chemistry, 2010. **20**(35): p. 7398.

31. Yoo, S., B. Domercq, and B. Kippelen, *Intensity-dependent equivalent circuit parameters of organic solar cells based on pentacene and C[sub 60].* Journal of Applied Physics, 2005. **97**(10): p. 103706.

32. Potscavage, W.J., et al., *Encapsulation of pentacene/C60 organic solar cells with Al2O3 deposited by atomic layer deposition.* Applied Physics Letters, 2007. **90**(25): p. 253511.

33. Yang, J. and T.-Q. Nguyen, *Effects of thin film processing on pentacene/C60 bilayer solar cell performance.* Organic Electronics, 2007. **8**(5): p. 566-574.

34. Sullivan, P. and T. Jones, *Pentacene/fullerene (C60) heterojunction solar cells: Device performance and degradation mechanisms.* Organic Electronics, 2008. **9**(5): p. 656-660.

35. Niggemann, M., et al., *Light trapping in organic solar cells* physica status solidi, 2008. **205**(12): p. 2862–2874.

36. Mott, N.F. *Note on the contact between a metal and an insulator or semiconductor.* in *Proc. Cambr. Phil. Soc.* 1938.

37. monch, W., *Metal-semiconductor contacts: electronic properties.* Surface Science, 1994. **299/300**: p. 928-944.

38. Greenham, N.C. and R.H. Friend, *Semiconductor device physics of conjugated polymers.* Solid State Physics, 1995. **49**(1).

39. Chen, L.-M., et al., *Interface investigation and engineering – achieving high performance polymer photovoltaic devices.* Journal of Materials Chemistry, 2010. **20**(13): p. 2575.

40. Mihailetchi, V.D., et al., *Cathode dependence of the open-circuit voltage of polymer:fullerene bulk heterojunction solar cells.* Journal of Applied Physics, 2003. **94**(10).

41. Brabec, C.J., et al., *Origin of the Open Circuit Voltage of Plastic Solar Cells.* Adv Funct. Mater, 2001. **11**(5): p. 374-380.

42. Crispin, X., *Interface dipole at organic/metal interfaces and organic solar cells.* Solar Energy Materials and Solar Cells, 2004. **83**: p. 147-168.

43. Kumar, A., S. Sista, and Y. Yang, *Dipole induced anomalous S-shape I-V curves in polymer solar cells.* Journal of Applied Physics, 2009. **105**(9): p. 094512.

44. Kim, J.Y., et al., *New Architecture for High-Efficiency Polymer Photovoltaic Cells Using Solution-Based Titanium Oxide as an Optical Spacer.* Advanced Materials, 2006. **18**(5): p. 572-576.

45. Wu, S., et al., *pH-neutral PEDOT:PSS as hole injection layer in polymer light* Organic Electronics, 2011. **12**(3): p. 504-508.

46. Koch, N., A. Elschner, and R.L. Johnson, *Green polyfluorene-conducting polymer interfaces: Energy level alignment and device performance.* J. Appl. Phy., 2006. **100**(2).

47. Zhang, F.L., et al., *Influence of buffer layers on the performance of polymer solar cells.* Appl. Phys. Lett., 2004. **84**(19): p. 3906-3908.

48. Kim, Y., et al., *Effects of thickness and thermal annealing of the PEDOT:PSS layer on the performance of polymer solar cells.* Organic Electronics, 2009. **10**(1): p. 205-209.

49. Kim, Y.-H., et al., *Performance and stability of electroluminescent device with self-assembled layers of poly(3,4-ethylenedioxythiophene)–poly(styrenesulfonate) and polyelectrolytes.* Thin Solid Films, 2006. **510**(1-2): p. 305-310.

50. Jong, M.P.d., L.J.v. IJzendoorn, and M.J.A.d. Voigt, *Stability of the interface between indium-tin-oxide and poly(3,4-ethylenedioxythiophene)/poly(styrenesulfonate) in polymer light-emitting diodes.* Appl. Phys. Lett., 2000. **77**(14): p. 2255-2257.

51. Cruz-Cruz, et al., *Study of the effect of DMSO concentration on the thickness of the PSS insulating barrier in PEDOT:PSS thin films.* Synth. Met., 2010. **160**(13-14): p. 1501-1506.

52. Ouyang, J., et al., *On the mechanism of conductivity enhancement in poly(3,4-ethylenedioxythiophene):poly(styrene sulfonate) film through solvent treatment.* Polymer, 2004. **45**: p. 8443-8450.

53. Zhang, C., et al., *Inverted Organic Photovoltaic Cells with Solution-Processed Zinc Oxide as Electron Collecting Layer.* Japanese Journal of Applied Physics, 2011. **50**(8): p. 082302.

54. Dou, L., et al., *Tandem Polymer Solar Cells Featuring a Spectrally Matched Low-Bandgap Polymer.* Nature Photonics, 2012. **6**: p. 180-185.

55. Kim, D.Y., et al., *The effect of molybdenum oxide interlayer on organic photovoltaic cells.* Appl. Phys. Lett., 2009. **95**.

56. Shrotriya, V., et al., *Transition metal oxides as the buffer layer for polymer photovoltaic cells.* Appl. Phys. Lett., 2006. **88**(7).

57. Lögdlund, M. and J.L. Brédas, *Theoretical studies of the interaction between aluminum and poly(p-phenylenevinylene) and derivatives.* J. Chem. Phy., 1994. **101**(5): p. 4357-4364.

58. Antoniadis, H., et al., *Photovoltaic and photoconductive properties of aluminum/poly(p-phenylene vinylene) interfaces.* Synth. Met., 1994. **62**(3): p. 265-271.

59. Gupta, D., M. Bag, and K.S. Narayan, *Correlating reduced fill factor in polymer solar cells to contact effects.* Applied Physics Letters, 2008. **92**(9): p. 093301.

60. Huang, J., Z. Xu, and Y. Yang, *Low-Work-Function Surface Formed by Solution-Processed and Thermally Deposited Nanoscale Layers of Cesium Carbonate.* Adv. Funct. Mater., 2007. **17**: p. 1966-1973.

61. Shaheen, S.E., et al., *Bright blue organic light-emitting diode with improved color purity using a LiF/Al cathode.* J. Appl. Phy., 1998. **84**(4): p. 2324-2327.

62. Hung, L.S., C.W. Tang, and M.G. Mason, *Enhanced electron injection in organic electroluminescence devices using an Al/LiF electrode.* Appl. Phys. Lett., 1997. **70**(2): p. 152-154.

63. Brabec, C.J., et al., *Effect of LiF/metal electrodes on the performance of plastic solar cells.* Appl. Phys. Lett., 2002. **80**(7): p. 1288-1290.

64. Huang, J., et al., *Improving the power efficiency of white light-emitting diode by doping electron transport material.* Applied Physics Letters, 2006. **89**(13): p. 133509.

65. Huang, J., et al., *Achieving High-Efficiency Polymer White-Light-Emitting Devices.* Adv. Mater., 2006. **18**: p. 114-117.

66. Huang, J., et al., *Detailed analysis of bathocuproine layer for organic solar cells based on copper phthalocyanine and C60.* J. Appl. Phy., 2009. **105**.

67. Gommans, H., et al., *On the Role of Bathocuproine in Organic Photovoltaic Cells.* Advanced Functional Materials, 2008. **18**(22): p. 3686-3691.

68. Hayakawa, A., et al., *High performance polythiophene/fullerene bulk-heterojunction solar cell with a TiOx hole blocking layer.* Applied Physics Letters, 2007. **90**(16): p. 163517.

69. Yoshikawa, O., et al., *Enhanced Efficiency and Stability in P3HT:PCBM Bulk Heterojunction Solar Cell by using TiO2 Hole Blocking Layer.* Material Research Society, 2007. **965**.

70. Manor, A., et al., *Enhancing functionality of ZnO hole blocking layer in organic photovoltaics.* Solar Energy Materials and Solar Cells, 2012. **98**: p. 491-493.

71. Hau, S.K., et al., *Air-stable inverted flexible polymer solar cells using zinc oxide nanoparticles as an electron selective layer.* Applied Physics Letters, 2008. **92**(25): p. 253301.

72. Michaelson, H.B., *The work function of the elements and its periodicity.* J. Appl. Phy., 1977. **48**(11): p. 4729-4733.

73. Mihailetchi, V.D., L.J.A. Koster, and P.W.M. Blom, *Effect of metal electrodes on the performance of polymer:fullerene bulk heterojunction solar cells.* Appl. Phys. Lett., 2004. **85**(6): p. 970-972.

74. Ishii, H., et al., *Kelvin probe study of band bending at organic semiconductor/metal interfaces: examination of Fermi level alignment.* phys. stat. sol.(a), 2004. **201**(6): p. 1075-1094.

75. Rajaputra, S., S. Vallurupalli, and V.P. Singh, *Schottky diode solar cells on electrodeposited copper phthalocyanine films.* Sol. Energy Mater. Sol. Cells, 2009. **93**(1): p. 60-64.

76. Kwong, C.Y., et al., *Improvement of the efficiency of phthalocyanine organic Schottky solar cells with ITO electrode treatment.* Appl. Phys. A, 2003. **77**: p. 555-560.

77. Jiangeng Xue, S.U., Barry P Rand, Stephen R Forrest, *4.2% efficient organic photovoltaic cells with low series resistances.* Appl. Phys. Lett., 2004. **84**(16): p. 3013-3015.

78. Peumans, P. and S.R. Forrest, *Very-high-efficiency double-heterostructure copper phthalocyanine/C60 photovoltaic cells.* Appl. Phys. Lett., 2001. **79**(1): p. 126-128.

79. Shaw, P.E., A. Ruseckas, and I.D.W. Samuel, *Exciton Diffusion Measurements in Poly(3-hexylthiophene).* Adv Mater, 2008. **20**(18): p. 3516-3520.

80. Hoppe, H., et al., *Nanoscale Morphology of Conjugated Polymer/Fullerene-Based Bulk-Heterojunction Solar Cells.* Adv Funct. Mater, 2004. **14**(10): p. 1005-1011.

81. Ballantyne, A.M., et al., *Understanding the Influence of Morphology on Poly(3-hexylselenothiophene):PCBM Solar Cells.* Macromolecules, 2010. **43**(3): p. 1169-1174.

82. Chirvase, D., et al., *Influence of nanomorphology on the photovoltaic action of polymer–fullerene composites.* Nanotechnology, 2004. **15**: p. 1317-1323.

83. Padinger, F., R.S. Rittberger, and N.S. Sariciftci, *Effects of Postproduction Treatment on Plastic Solar Cells.* Advanced Functional Materials, 2003. **13**(2): p. 1-4.

84. Minnaert, B. and M. Burgelman, *Modelling MEH-PPV:PCBM (1:4) bulk heterojunction solar cells* Proc. of NUMOS, 2007: p. 327-339.

85. Mihailetchi, V.D., et al., *Compositional Dependence of the Performance of Poly(p-phenylenevinylene): Methanofullerene Bulk-Heterojunction Solar Cells.* Advanced Functional Materials, 2005. **15**(5).

86. Mancal, J.V., et al., *State-of-the-art MDMO-PPV:PCBM bulk hetero-junction organic solar cells : materials, nano-morphology and electro-optical properties.* Proc. SPIE, 2003. **4801**: p. 15-21.

87. Rockett, A., *Organic Semiconductors*, in *The Materials Science of Semiconductors*. 2008, Springer US. p. 395-453.

88. Gregg, B.A., S.-G. Chen, and R.A. Cormier, *Coulomb Forces and Doping in Organic Semiconductors.* Chem. Mater., 2004. **16**(23): p. 4586-4599.

89. Horowitz, G., *Organic Field-Effect Transistors.* Adv Mater, 1998. **10**(5): p. 365-377.

90. Goodman, A.M. and A. Rose, *Double Extraction of Uniformly Generated Electron-Hole Pairs from Insulators with Noninjecting Contacts.* Journal of Applied Physics, 1971. **42**(7): p. 2823.

91. Mihailetchi, V., J. Wildeman, and P. Blom, *Space-Charge Limited Photocurrent.* Physical Review Letters, 2005. **94**(12).

92. Brabeca, C.J., et al., *Tracing photoinduced electron transfer process in conjugated polymer/fullerene bulk heterojunctions in real time.* Chem. Phy. Lett., 2001. **340**(3-4): p. 232-236.

93. Offermans, T., S.C.J. Meskers, and R.A.J. Janssen, *Charge recombination in a poly(para-phenylene vinylene)-fullerene derivative composite film studied by transient, nonresonant, hole-burning spectroscopy.* J. Chem. Phy., 2003. **119**(20).

94. Bassler, H. and A. Kohler, *Charge transport in organic semiconductors.* Top Curr Chem, 2012. **312**: p. 1-65.

95. Mehraeen, S., V. Coropceanu, and J.-L. Brédas, *Role of band states and trap states in the electrical properties of organic semiconductors: Hopping versus mobility edge model.* Physical Review B, 2013. **87**(19).

96. Ashcroft, N.W. and N.D. Mermin, *Solid State Physics*. 1976: Thomson Learning Inc.

97. Li, L., G. Meller, and H. Kosina, *Temperature and field-dependence of hopping conduction in organic semiconductors.* Microelectronics Journal, 2006. **38**: p. 47-51.

98. Bassler, H., *Charge Transport in Disorder Organic Photoconductors a Monte Carlo Simulation Study*. Physica status solidi, 1993. **175**(1): p. 15-56.

99. Coropceanu, V., et al., *Charge Transport in Organic Semiconductors.* Chem. Rev., 2007. **107**(4): p. 926-952.

100. Kirchartz, T., et al., *Mobility dependent efficiencies of organic bulk heterojunction solar cells: Surface recombination and charge transfer state distribution.* Physical Review B, 2009. **80**(3).

101. Mandoc, M.M., L.J.A. Koster, and P.W.M. Blom, *Optimum charge carrier mobility in organic solar cells.* Applied Physics Letters, 2007. **90**(13): p. 133504.

102. Deibel, C., A. Wagenpfahl, and V. Dyakonov, *Influence of charge carrier mobility on the performance of organic solar cells.* physica status solidi (RRL) **-** Rapid Research Letters, 2008. **2**(4): p. 175-177.

103. Shieh, J.-T., et al., *The effect of carrier mobility in organic solar cells.* Journal of Applied Physics, 2010. **107**(8): p. 084503.

104. Koster, L.J.A., V.D. Mihailetchi, and P.W.M. Blom, *Bimolecular recombination in polymer/fullerene bulk heterojunction solar cells.* Applied Physics Letters, 2006. **88**(5): p. 052104.

105. Tress, W., K. Leo, and M. Riede, *Dominating recombination mechanisms in organic solar cells based on ZnPc and C60.* Applied Physics Letters, 2013. **102**(16): p. 163901.

106. Chiu, M.-Y., et al., *Simultaneous Use of Small- and Wide-Angle X-ray Techniques to Analyze Nanometerscale Phase Separation in Polymer Heterojunction Solar Cells.* Adv Mater, 2008. **20**: p. 2573–2578.

107. Savenije, T.J., et al., *The Effect of Thermal Treatment on the Morphology and Charge Carrier Dynamics in a Polythiophene–Fullerene Bulk Heterojunction.* Adv. Funct. Mater., 2005. **15**: p. 1260-1266.

108. Kumar, A., et al., *High efficiency polymer solar cells with vertically modulated nanoscale morphology*. Nanotechnology, 2009. **20**(16): p. 165202.

109. Campoy-Quiles, M., et al., *Morphology evolution via self-organization and lateral and vertical diffusion in polymer:fullerene solar cell blends.* Nature Materials, 2008. **7**: p. 158-164.

110. Stevens, D.M., et al., *Enhancement of the Morphology and Open Circuit Voltage in Bilayer Polymer/Fullerene Solar Cells.* J. phys. Chem., 2009. **113**(26).

111. Koster, L.J.A., et al., *The optimal band gap for plastic photovoltaics.* SPIE newsroom, 2007.

112. Wagenpfahl, A., et al., *S-shaped current-voltage characteristics of organic solar devices.* Physical Review B, 2010. **82**(11).

113. Tress, W., et al., *Imbalanced mobilities causing S-shaped IV curves in planar heterojunction organic solar cells.* Applied Physics Letters, 2011. **98**(6): p. 063301.

114. Deibel, C. and V. Dyakonov, *Polymer–fullerene bulk heterojunction solar cells.* Reports on Progress in Physics, 2010. **73**(9): p. 096401.

115. Cheyns, D., et al., *Analytical model for the open-circuit voltage and its associated resistance in organic planar heterojunction solar cells.* Physical Review B, 2008. **77**(16).

116. Koster, L.J.A., et al., *Light intensity dependence of open-circuit voltage of polymer:fullerene solar cells.* Applied Physics Letters, 2005. **86**(12): p. 123509.

117. Scharber, M.C., et al., *Design Rules for Donors in Bulk-Heterojunction Solar Cells—Towards 10 % Energy-Conversion Efficiency.* Advanced Materials, 2006. **18**(6): p. 789-794.

118. Shockley, W. and H.J. Queisser, *Detailed Balance Limit of Efficiency of p-n Junction Solar Cells.* J. Appl. Phy., 1961. **32**(3): p. 510-519.

119. Wagner, J., T. Fritz, and H. Bottcher, *Computer Modelling of Organic Thin Film Solar Cells.* Physical Review Letters, 1993. **136**: p. 423-432.

120. Ray, B. and M.A. Alam, *Achieving Fill Factor Above 80% in Organic Solar Cells by Charged Interface.* IEEE J. Photovoltaics, 2013. **3**(1): p. 310-317.

121. Ghosh, A.K. and T. Feng, *Merocynanine organic solar cells.* Journal of Applied Physics, 1978. **49**(12): p. 5982.

122. Ray, B. and M.A. Alam, *Random vs regularized OPV: Limits of performance gain of organic bulk heterojunction solar cells by morphology engineering.* Solar Energy Materials and Solar Cells, 2012. **99**: p. 204-212.

123. Koster, L., et al., *Device model for the operation of polymer/fullerene bulk heterojunction solar cells.* Physical Review B, 2005. **72**(8).

124. Langevin, P., Ann. Chim. Phys., 1903. **28**.

125. Yamashita, Y., *Organic semiconductors for organic field-effect transistors.* Sci. Technol. Adv. Mater. , 2009. **10**.

126. Hasegawa, T. and J. Takeya, *Organic field-effect transistors using single crystals.* Sci. Technol. Adv. Mater., 2009. **10**.

127. Kaur, I., et al., *Substituent Effects in Pentacenes: Gaining Control over HOMO-LUMO Gaps and Photooxidative Resistances.* J. Am. Chem. Soc., 2008. **130**: p. 16274-16286.

128. Sakamoto, Y., et al., *Perfluoropentacene: High-Performance p-n Junctions and Complementary Circuits with Pentacene.* J. Am. Chem. Soc., 2004. **126**: p. 8138-8140.

129. Q. Miao, X.C., S. Xiao, R. Zeiss, M. Lefenfeld, C. Kloc, T. Siegrist, M. Steigerwald, C. Nuckolls, *Organization of Acenes with a Cruciform Assembly Motif.* J. Am. Chem. Soc., 2006. **128**: p. 1340-1345.

130. Anthony, J.E., et al., *Functionalized Pentacene: Improved Electronic Properties from Control of Solid-State Order.* J. Am. Chem. Soc., 2001. **123**: p. 9482-9483.

131. Katsuta, S., et al., *Synthesis, Properties, and Ambipolar Organic Field-Effect Transistor Performances of Symmetrically Cyanated Pentacene and Naphthacene as Air-Stable Acene Derivatives.* Organic Letters, 2011. **13**(6): p. 1454-1457.

132. Chen, J., et al., *The influence of side chains on the structures and properties of functionalized pentacenes.* J. Mater. Chem., 2008. **18**: p. 1961-1971.

133. Lloyd, M.T., et al., *Photovoltaic cells from a soluble pentacene derivative.* Organic Electronics, 2006. **7**(5): p. 243-248.

134. Jiang, Y., et al., *Impact of regioregularity on thin-film transistor and photovoltaic cell performances of pentacene-containing polymers.* J. Mater. Chem., 2012. **22**: p. 4356-4363.

135. Palilisa, L.C., et al., *Organic photovoltaic cells with high open circuit voltages based on pentacene derivatives.* Organic Electronics, 2008. **9**(5): p. 747-752.

136. Gorodetsky, A.A., et al., *Solar Cells from a Solution Processable Pentacene with Improved Air Stability.* Chem. Mater., 2009. **21**(18): p. 4090-4092.

137. Park, S.K., et al., *High mobility solution processed 6,13-bis(triisopropyl-silylethynyl) pentacene organic thin film transistors.* Appl. Phys. Lett., 2007. **91**.

138. Pramanik, C., et al., *Water soluble pentacene.* Journal of Materials Chemistry C, 2013. **1**(11): p. 2193.

139. C. D. Sheraw, T.N.J., D. L. Eaton and J. E. Anthony, *Functionalized Pentacene Active Layer Organic Thin-Film Transistors.* Adv. Mater., 2003. **15**(23): p. 2009-2011.

140. S. K. Park, T.N.J., J. E. Anthony and D. A. Mourey, *High mobility solution processed 6,13-bis(triisopropyl-silylethynyl) pentacene organic thin film transistors.* Appl. Phys. Lett., 2007. **91**(6).

141. Kobayashi, K., et al., *Synthesis and Cofacial π-Stacked Packing Arrangement of 6,13-Bis(alkylthio)pentacene.* Org. Lett., 2006. **8**(11): p. 2385-2388.

142. Jihua Chen, C.K.T., Junyan Yang, Charles Shaw, Max Shtein, John Anthony, David C. Martin, *Thermal and mechanical cracking in bis(triisopropylsilylethnyl) pentacene thin films.* J. Polym. Sci. Part B, 2006. **44**(24): p. 3621-3641.

143. J. A. Merlo, C.R.N., C. P. Gerlach, T. W. Kelley, D. V. Muyres, S. E. Fritz, M. F. Toney and C. D. Frisbie, *p-Channel Organic Semiconductors Based on Hybrid Acene−Thiophene Molecules for Thin-Film Transistor Applications.* J. Am. Chem. Soc., 2005. **127**(11): p. 3997-4009.

144. Yuan, Y., J. Huang, and G. Li, *Intermediate Layers in Tandem Organic Solar Cells.* Green, 2011. **1**(1).

145. Kamat, P.V., I. Bedja, and S. Hotchandanit, *Photoinduced Charge Transfer between Carbon and Semiconductor Clusters. One-Electron Reduction of Ca in Colloidal TiO2 Semiconductor Suspensions.* J. phys. Chem., 1994. **98**(37): p. 9137-9142.

146. Madakasira, P., et al., *Multilayer encapsulation of plastic photovoltaic devices.* Synthetic Metals, 2005. **155**(2): p. 332-335.

147. Yilmaz, C., et al., *Large-Scale Nanorods Nanomanufacturing by Electric-Field-Directed Assembly for Nanoscale Device Applications.* IEEE Trans. Nanotech, 2010. **9**(5): p. 653-658.

148. *Sun: Facts and Figures*, in *Solar System Exploration*, NASA.

149. Schoenberg, E., *Theoretische Photometrie, Über die Extinktion des Lichtes in der Erdatmosphäre*. 1929, Berlin: Springer.

150. Meinel, A.B. and M.P. Meinel, *Applied Solar Energy*. 1976: Addison Wesley Publishing Co.